

# **Transport Spectroscopy of Semiconductor Superconductor Nanowire Hybrid Devices**

**Inauguraldissertation**

zur  
Erlangung der Würde eines Doktors der Philosophie  
vorgelegt der  
Philosophisch-Naturwissenschaftlichen Fakultät  
der Universität Basel

von

**Christian Helmut Jünger  
aus Deutschland**

Basel, 2020

Genehmigt von der Philosophisch-Naturwissenschaftlichen Fakultät  
auf Antrag von  
Prof. Dr. Christian Schönenberger  
Prof. Dr. Jesper Nygård  
Dr. Fabrizio Nichele

Basel, 23.04.2019

Prof. Dr. Martin Spiess  
Dekan

# Contents

<b>Introduction</b>	<b>vii</b>
<b>1. InAs nanowires</b>	<b>1</b>
1.1. InAs nanowire growth . . . . .	1
1.2. Electronic properties . . . . .	4
<b>2. Quantum dots coupled to a superconductor</b>	<b>5</b>
2.1. Quantum dots . . . . .	5
2.1.1. Coulomb blockade . . . . .	6
2.1.2. Transport spectroscopy with Coulomb diamonds . . . . .	8
2.2. Superconductivity . . . . .	11
2.3. Transport in superconductor - normal metal structures . . . . .	12
2.3.1. Quasiparticle transport . . . . .	13
2.3.2. Andreev reflection . . . . .	14
2.3.3. Andreev bound states . . . . .	16
2.3.4. Andreev bound states in S - QD systems . . . . .	18
2.4. Transport in S - QD - S . . . . .	22
2.4.1. Strong coupling regime . . . . .	22
2.4.2. Weak coupling regime . . . . .	23
2.4.3. Intermediate coupling regime . . . . .	23
2.5. Crossed Andreev reflection . . . . .	24
2.5.1. Cooper pair splitting using quantum dots . . . . .	25
<b>3. Fabrication</b>	<b>27</b>
3.1. Device fabrication . . . . .	27
3.1.1. Standard nanowire devices . . . . .	27
3.1.2. Epitaxial Al shell devices . . . . .	30
3.2. Cryogenic measurement set-up . . . . .	33
<b>4. Crystal phase defined quantum dots</b>	<b>35</b>
4.1. Zincblende and wurtzite crystal phase of InAs nanowires . . . . .	36
4.2. Crystal phase defined quantum dots . . . . .	37
4.3. Characterization of crystal phase defined quantum dots in InAs nanowires . . . . .	39

<b>5. Spectroscopy of the superconducting proximity effect in InAs nanowires using built-in quantum dots</b>	<b>45</b>
5.1. Sample and characterization . . . . .	45
5.2. Proximity gap in cotunneling regime . . . . .	48
5.3. Proximity gap in sequential tunneling regime . . . . .	50
5.4. Discussion . . . . .	54
<b>6. Spectroscopy of superconducting sub-gap states in InAs nanowires</b>	<b>59</b>
6.1. Device and characterization . . . . .	59
6.2. Spectroscopy of superconducting sub-gap states . . . . .	61
6.3. Magnetic field dependence . . . . .	64
6.4. Conclusions . . . . .	66
<b>7. Hybridization of quantum dot and Andreev bound states</b>	<b>69</b>
7.1. Supercurrent in open regime . . . . .	70
7.2. Single electron characteristics in weak coupling regime . . . . .	72
7.3. Intermediate coupling regime . . . . .	74
7.3.1. Andreev bound state spectroscopy in cotunnelling regime	75
7.3.2. Andreev bound state spectroscopy in sequential tunneling regime . . . . .	76
7.3.3. Resonant tunneling model . . . . .	79
7.3.4. Conclusions . . . . .	84
<b>8. Cooper-pair splitting in two parallel InAs nanowires</b>	<b>87</b>
8.1. Double nanowire device and characterization . . . . .	87
8.2. Cooper pair Splitting in double NW . . . . .	89
8.3. Conclusion . . . . .	94
<b>9. Summary and outlook</b>	<b>95</b>
<b>Bibliography</b>	<b>97</b>
<b>A. Fabrication Recipes</b>	<b>109</b>
A.1. Fabrication of InAs Nanowire devices . . . . .	109
A.1.1. Wafer characteristics . . . . .	109
A.1.2. Cleaning . . . . .	109
A.2. Electron beam lithography . . . . .	109
A.2.1. PMMA etch mask . . . . .	109
A.2.2. ZEP mask for Pb contacts . . . . .	110
A.3. Reactive ion etching - O <sub>2</sub> plasma cleaning . . . . .	110
A.4. Etching of NW native oxide . . . . .	110
A.4.1. Argon Ion Beam milling . . . . .	110
A.4.2. Sulphur passivation . . . . .	111



A.4.3. HCl . . . . .	111
A.5. Etching of epitaxial aluminum shell . . . . .	112
A.6. Contacts . . . . .	113
A.6.1. Ti/Au leads . . . . .	113
A.6.2. Ti/Al leads . . . . .	113
A.6.3. Pd/Pb/In leads . . . . .	113
<b>B. Further information on spectroscopy of the superconducting proximity effect in nanowires using integrated quantum dots</b>	<b>115</b>
B.1. Additional numerical calculations for individual ABS . . . . .	115
B.2. Additional numerical calculations for interface with disorder . .	116
B.3. Additional measurements of S - I - S junction . . . . .	116
<b>C. Further information on spectroscopy of superconducting sub-gap states</b>	<b>119</b>
<b>D. Additional measurements of S - QD - S</b>	<b>121</b>
D.1. Supercurrent in ZB segment of InAs nanowire . . . . .	121
D.2. Resonant tunneling model with two discrete levels . . . . .	122
D.3. Additional data measured in S - QD - S device . . . . .	122
<b>E. Further information on Cooper pair splitting in two parallel InAs nanowires</b>	<b>125</b>
E.1. Coulomb diamond measurements . . . . .	125
<b>F. Quantum dots in InAs defined by InP tunnel barriers</b>	<b>127</b>
F.1. Coulomb diamond measurements . . . . .	127
<b>G. Preliminary results of superconducting nanowire multi-junction</b>	<b>129</b>
G.1. Quartet device . . . . .	129
G.2. Supercurrent in multi-junction . . . . .	130
<b>Curriculum Vitae</b>	<b>133</b>
<b>Publications</b>	<b>135</b>
<b>Acknowledgements</b>	<b>137</b>



# Introduction

For almost a decade indium arsenide nanowires (InAs) have been the work horse for quantum transport in hybrid devices [1]. This is due to the large versatility of available types of materials that form good contact, such as metals, ferromagnets [2] and superconductors [3]. Combined with their low dimensionality, low effective mass and intrinsically large spin orbit interaction, InAs nanowires provide the ideal platform to study various fundamental transport effects, like the entanglement of spins [4] or the ferromagnetic proximity effect [2]. Furthermore, this material system is a potential candidate to host so-called spin-orbit qubits [5, 6], which enable storage and manipulation of quantum information.

Alternatively, one can use topological qubits [7] based on topologically protected particles such as Majorana bound states (MBS) [8–13] or parafermions [14–16] to encode qubits. Both rely on the combination of one dimensional nanowires with strong spin orbit coupling proximitized by a superconductor. Recent advances in growth synthesis and interface engineering have triggered a new generation of nanowire devices. This enabled to create more complex structures made of several NWs, like nanowire crosses [17–19] or nanowire networks (“hashtags”) [20]. Furthermore, radial [21] and axial [22, 23] nanowire heterostructures can be grown in a controlled manner, allowing to implement quantum dots (QDs) in-situ during the growth [24, 25]. The latest breakthrough was to grow the superconducting contact epitaxially to nanowires [20, 26–28] which resulted in numerous reports on the observation of MBS [29–32]. However, the unambiguous identification of MBS is not straight forward [33, 34].

Several theoretical proposals suggest to investigate these topological states by using a QD as a spectrometer to probe their lifetime [35, 36], parity [37] or spin texture [38]. Until now, there is one report published where the QD was formed by electrical gates [30], which gave insight on the non-locality of MBS [31]. However, spectroscopy of such superconducting bound states remains challenging because of the lack of control on the QD in the nanowire.

The reason for this is the following: most QDs used in spectroscopy measurements of superconducting nanowire hybrid devices are either defined by the source drain contacts [39] or by electrostatic (bottom) gates [30, 40–43]. Both methods hold various problems: neither the exact location, nor the electronic

characteristics of the QD can be predicted or systematically controlled. In addition, QDs defined by electrostatic gates are sensitive to the electrostatics of the entire system, which is especially disadvantageous when working with superconductors. Using this type of QDs as an electronic spectrometer is therefore problematic, as it is not clear where the voltage drops in the system, which has a strong impact on the determined energies and amplitudes of the signal.

## **Motivation of this thesis**

In order to realise the above proposed systematic spectroscopy of MBS [35–38] we present first steps towards unambiguous transport spectroscopy of topological states in nanowires.

Within the experiments described in this thesis, we demonstrate transport spectroscopy on superconducting hybrid systems using a QD defined by hard wall barriers in nanowires. In our case, this is realised by atomically precise engineered tunnel barriers defining the QD both spatially and energetically. Consequently, the size of the QD can be controlled and its electrical characteristics can be predicted. Furthermore, the location of the QD in the nanowire is precisely known.

This results in a fundamentally new experimental situation: as the location of the integrated QD is known, we can clearly subdivide the system into the segment forming the QD and the remaining nanowire lead segments. This enables us to distinguish between the origin of individual physical effects. Most importantly, the bias voltage drops on the barrier-defined QD, when the conductance of this platform is measured. Consequently, the differential conductance is directly proportional to the density of states of the nanowire segment being probed. This allows us to perform tunnel spectroscopy in a controlled and systematic manner in NW hybrid systems.

The goal of this thesis is to use integrated QDs as tunnel spectrometers, in order to probe the DOS and potential sub-gap states in the adjacent nanowire lead segment. By investigating a large variety of effects in NW lead segments, when they are coupled to a superconducting electrode, we pave the way towards systematic spectroscopy of topological states in NWs.

We can use our platform essentially in two different ways: 1) as a controllable single tunnel barrier, when the quantum dot is in Coulomb blockade and 2) as an energy filter, when the quantum dot is on resonance.

By using both regimes, we demonstrate the evolution of the proximity induced superconducting gap in the nanowire lead segment, when the nanowire is coupled to one superconducting electrode. We can explain the observed characteristic features as a transition between the long and the short junction limit of the device (see chapter 5).

---

Furthermore, we show spectroscopy measurements on a NW segment, in which discrete subgap states form. These subgap states exhibit rich physics, due to a competition between Coulomb and the Kondo effect (see chapter 6).

Moreover, we discuss electronic spectroscopy measurements performed in NW devices with integrated QDs with two superconducting electrodes. Here, we can access a large variety of transport regimes. Most remarkably, we find a hybridisation of the quantum dot resonances with Andreev bound states in the intermediate coupling regime (see chapter 7).

In addition, we present a first step towards devices, based on two nanowires, a potential candidate for the detection of parafermions. For the first time, we present a splitting of Cooper pairs into separated individual nanowires (see chapter 8).

In the following we give the outline of this thesis:

Chapter 1 provides a short introduction to semiconducting InAs nanowires. Afterwards, we introduce the relevant theoretical background on transport with quantum dots and superconductivity (chapter 2). Chapter 3 covers the standard fabrication process of semiconducting superconducting nanowire devices as well as a detailed discussion on fabrication of InAs nanowires with an epitaxial aluminum shell. Additionally, a brief introduction to the cryogenic measurement set-up is given.

First results on crystal phase defined QDs in InAs NWs are presented within the characterization of the QDs in chapter 4

Results based on spectroscopy measurements using crystal phase defined quantum dots are presented in chapter 5, 6 and 7.

Chapter 8 provides first measurements of Cooper-pair splitting in a parallel double nanowire device.

In chapter 9 we summarise the results of this thesis.

In addition, we present preliminary results on quantum dots in InAs NWs, defined by InP tunnel barriers and supercurrent measurements in multi-terminal nanowire superconductor junctions in the appendix F and G.



# 1 InAs nanowires

---

The following chapter provides an introduction to the properties of InAs nanowires, such as the growth process and basic electronic characteristics. Semiconducting nanowires are single crystalline one-dimensional nanostructures. Typically, they have a diameter between 10 nm to 100 nm and lengths up to several micrometer. Until now, synthesis of group III-V, II-VI and III SCs have been reported [44]. Due to the large possible material variety, semiconducting nanowires can be used in a wide spectrum of applications [45] such as LEDs [46], solar cells [47] or sensors [48]. However, they are also of special interest in the field of nanoelectronics, as they can for example be used as efficient transistors [49, 50].

This is especially the case for nanowires made of indium-arsenide (InAs), as this material platform offers additional advantages: low effective mass, small band gap, high mobility [51] and large spin orbit interaction [52], allowing electrical control on the spin and the possibility to form a spin-orbit qubit [5]. In the following chapter, we briefly discuss the basics of nanowire growth and provide a summary of electronic characteristics of InAs nanowires, following Refs. [53–55].

## 1.1. InAs nanowire growth

For many decades, bottom up growth of semiconducting nanowires is based on vapour-liquid-solid methods (VLS) [56], such as molecular beam epitaxy, or metal organic vapour phase epitaxy to name just a few examples [54, 55]. The basic principal of these techniques relies on the accumulation of gaseous atomic or metal-organic precursors inside a metallic catalyst particle [54]. The catalyst particle (usually made of gold) can be deposited by different methods. For example by metal evaporation and subsequent annealing or by aerosol techniques. Each techniques results in a random distribution of the nanowires (situation I in Fig. 1.1 a) [54]. One can also obtain nanowire arrays by pre-patterning the substrate by lithography, resulting in an array-like structure (see Fig. 1.1 b). The nanowires grow from the catalyst particle when it gets supersaturated by the precursor concentration (situation II/III). The main difference in the above mentioned growth techniques is the way the catalyst particle is fed by the semiconductor. By controlling the size of the catalyst

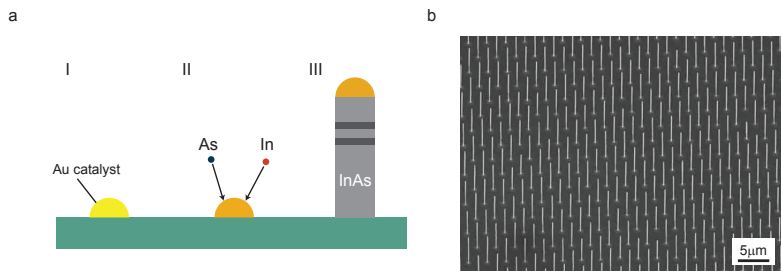


**Figure 1.1. Growth of InAs nanowires.** **a** Illustration of a vapour-liquid-solid growth process of InAs NWs. Situation I shows the pre-defined gold catalyst particle (yellow) on the growth substrate (green), which is fed by In (blue) and As (red) until it supersaturates (II) and grows (III). The ark grey stripes inside the InAs nanowire illustrate an example of a controlled implementation of a hetero-structure, achieved by adjustment of growth parameters. **b** Transmission electron micrograph of InAs NWs on a pre-patterned substrate. Schematic adapted from [45, 54]. TEM image provided by S. Lehmann.

particle one can determine the diameter of the nanowire, whereas its length depends on the growth time [54]. The growth direction and also the crystal structure depend on many growth parameters and is therefore difficult to control [53–55].

In the case of InAs nanowires, it has been found that they usually grow in a mix of wurtzite (WZ) and zincblende (ZB) crystal phase, whereas ZB is the bulk crystal structure of InAs. In the extreme case of polytypic NWs, transport properties can be drastically effected by band gap mismatches [57]. Due to advances in growth techniques, it is possible to growth defect free single crystal InAs NWs, meaning either pure WZ or ZB crystal phase. It has also been shown that it is possible to switch between both crystallographic phases in a controlled way, creating ZB-WZ homostructures with atomic precision [23, 58]. Furthermore, the WZ segments act as potential barriers, which can be used to create a quantum dot [25]. We will elaborate this system in more detail in chapter 4, as it is the main working horse for experiments performed in this thesis [59].

Within recent technical advances of nanowire synthesis, various types of nanowire heterostructures with different materials have been successfully grown. This is mainly possible because strain originating from a large lattice mismatch of different materials can relax at the NW surface, which is not possible in bulk systems. It is, for example, possible to grow nanowires in radial heterostructures in a core-shell configuration [21, 60] or axially along the growth



direction [22]. In Fig.1.2, we present an example of an InAs NW heterostructure made of InAs and InP. Fig.1.2 a shows a scanning electron micrograph (SEM) of such a NW taken with the help of a quadrant back-scatter electron detector. This detector allows us to distinguish different materials by contrast in intensity. Therefore, we can extract the dimensions (in this case:  $\approx 5$  nm thick; separation:  $\approx 20$  nm) as well as the location of the InP segments (dark contrast), as shown in the inset of Fig. 1.2 a, within the otherwise InAs NW. In Fig. 1.2 b we present a transmission electron micrograph of a such InAs/InP heterostructure, where we can observe the InP segments in more clearly. However, TEM imaging is tedious and can not be done for every NW that is fabricated. Therefore it is very helpful to have the capability to detect the InP segments in these NWs by SEM techniques. For us, this is of special interest, as the InP segments are acting as a hard wall barrier for electrons, forming a well defined QD in between [24, 61–64]. These NWs have been grown and thankfully provided by Prof. L. Sorba (NEST Pisa). In addition, it is possible to grow more complex nanowire structures, due to controlled pre-patterning of the growth substrate, such as nanocrosses [17–19] or so called nanowire hashtags [20]. One of the biggest breakthrough within the last years was the achievement of growing superconducting materials epitaxially on NWs, with a defect free interface [20, 26].

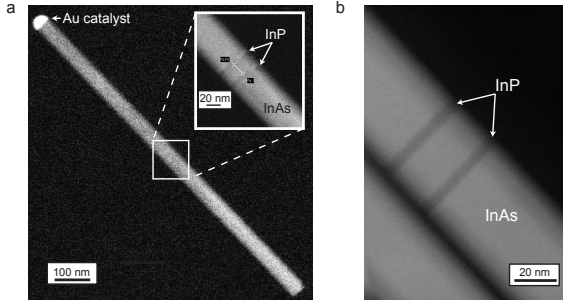


**Figure 1.2. InAs/InP nanowire heterostructure.** **a** Scanning electron micrograph taken with a quadrant back-scatter electron detector of InAs NW with InP segments. Inset shows zoomed in image, revealing the InP segments as dark stripes. **b** Transmission electron micrograph of InAs NW with InP segments (dark stripes). TEM image provided by L. Sorba.

## 1.2. Electronic properties

We now focus on the electronic properties of InAs nanowires, arising due to intrinsic material properties and dimensional confinement, following [54, 55]. The electronic band structure of InAs NWs yields a parabolic dispersion relation for the conduction band yielding an effective electron mass of  $m^* = 0.023m_e$ . Here,  $m_e$  is the free electron mass [54]. The electronic states form quantized transverse modes, caused by the radial two-dimensional confinement, described by the dispersion relation for each sub-band:  $E_n(k_x) = E_n + \frac{\hbar^2 k_x^2}{2m^*}$ . Here,  $E_n$  is the minimum required energy, due to the quantization in modes [55]. By connecting an electronic reservoir to one channel, results in the current  $I = \frac{2e^2}{h}N$ , which scales with the number of occupied modes  $N$  [54]. This means, whenever a new subband becomes occupied, we expect a stepwise increase in quantized conduction [54, 55]. This, as well as ballistic transport, has been confirmed lately by several groups [18, 65–67]. Furthermore, due to the strong spin orbit coupling, we can further expect the appearance of a so-called helical gap in such systems[68]. First signatures of an interaction induced helical gap has also been reported lately in InAs NWs [69].

It has also been found that the diameter of the InAs NW strongly effects transport. For InAs NWs with diameter less than  $\approx 40$  nm, a rapid decrease of electron mobility was reported [70], most likely due to enhanced surface scattering. Throughout this work we only used InAs NWs with diameters between 60 nm to 100 nm for which mobilities up to  $6600 \text{ cm}^2/\text{Vs}$  have been reported [51].

Furthermore, the semiconducting energy gap differs for both crystal phases. Since ZB is the bulk InAs crystal phase, the properties of the band are well known: direct band gap  $E_{ZB} = 0.42 \text{ eV}$  and g-factor  $g = -14.9$  [71]. The WZ crystal phase has a larger band gap of  $E_{WZ} \approx 0.52 \text{ eV}$  to  $0.54 \text{ eV}$ , consistent with what has been found in ZB-WZ homostructures [25]. In addition, it is possible to achieve good low-ohmic contacts with many different contact materials, as the Fermi level is pinned to the surface [72]. Furthermore, the mean free path in InAs nanowires has been reported to be  $\approx 100 \text{ nm}$  [66].

The presented characteristics of InAs NWs, such as: various controlled synthesis possibilities (like different crystal phases, complex geometries, epitaxial control on interfaces to superconductors), and their electronic properties like strong spin-orbit interaction make InAs a perfect candidate to study transport experiments. This platform especially gained renewed interest, as it can serve as a host for topological states, such as Majorana fermions, and therefore constitute a potential platform topological quantum information processing [73]. For a more detailed summary of electronic properties of InAs nanowires we refer to Refs. [53–55].

# 2 Quantum dots coupled to a superconductor

---

The following chapter will provide the theoretical basis for the experiments performed in this thesis. After a brief introduction on quantum dots and superconductivity, the most relevant transport mechanisms in nanowire hybrid devices are discussed. We will explicitly discuss transport processes in superconductor - quantum dot - normal metal structures, such as Andreev bound states and Cooper pair splitting. Furthermore, we will presents transport phenomena that can occur in systems with only superconducting electrodes. Here, we follow Refs. [54, 55, 74–76].

## 2.1. Quantum dots

One of the key ingredient of this thesis are quantum dots (QDs) - quasi zero-dimensional islands, commonly referred to as “artificial atoms” [75]. Here, an electron is confined in all three dimensions which results in a quantization of the energy spectrum. However, QDs can be coupled to source drain electrodes and electrostatic gates, allowing us to probe their characteristics in transport experiments at low temperatures. Since they are very small, also the capacitance of the island is small and therefore requires a large energy cost, to add an additional electron [54]. This so-called Coulomb blockade (CB) is the most universal property of QDs and has been observed in many different solid state systems, such as two dimensional electron gases [77], graphene [78], carbon nanotubes [79] and semiconducting nanowires [80].

In order to describe the entire energy spectrum of a single quantum dot, one takes into account Coulomb interactions and quantum confinement [81]. Just like the the “particle in a box” scenario, quantum confinement leads to an energy spacing between individual energy levels of  $\delta E$ . In systems where electrons have a quadratic dispersion relation,  $\delta E$  decreases with the size of the QD  $L$  as  $\delta E \propto 1/L^2$  [74], which depends on the geometry of the QD. Furthermore, the shell filling of the energy levels depends on the spin degeneracy and the Pauli principle [76, 82].

### 2.1.1. Coulomb blockade

Coulomb interaction effects can be described by the constant interaction model [75, 76, 81, 82], which makes two major assumptions: we can assign a constant self capacitance to the QD and electron-electron interactions do not affect the discrete energy spectrum of the QD.

In Fig. 2.1 a circuit diagram is shown, with a QD (orange) being tunnel coupled to source (S) and drain (D) electrodes by a coupling strength  $\Gamma_{S/D}$  and capacitively coupled with capacitances  $C_{S/D}$ , respectively [55, 76]. In addition, a voltage  $V_G$  can be applied on the gate (G) that is only capacitively coupled to the QD with capacitance  $C_G$ . The QD capacitance is the sum of all capacitances:  $C = C_S + C_D + C_G$ , whereas its energy  $E_{tot}$  is described by the following formula (considering  $N$  electrons) [54, 82]:

$$E_{tot} = \frac{1}{2C} \left[ -|e|(N - N_0) + \sum_i C_i V_i \right]^2 + \sum_{n=1}^N E_n, \quad (2.1)$$

where  $i = S, D, G$  and  $N_0$  is the number of charges when the QD is not charged (meaning all  $V_i = 0$ ). The number of electron  $N$  varies discretely, whereas  $C_i V_i$  are charges induced by the gate [76]. The electrochemical potential of the system can be written as:  $\mu(N) = E_{tot}(N) - E_{tot}(N - 1)$  [54, 55, 76, 81, 82]:

$$\mu(N) = E_n + \frac{e^2}{C} \left( N - N_0 - \frac{1}{2} \right) - \frac{|e|}{C} C_G V_G. \quad (2.2)$$

This is the energy which is needed to add the next electron and constitutes as a “ladder” of discrete levels (illustrated in Fig. 2.1 b) [81, 82]. The difference between those levels is the addition energy and is defined by [54, 55, 81, 82]:

$$E_{add} = \mu(N + 1) - \mu(N) = \frac{e^2}{C} + \delta E, \quad (2.3)$$

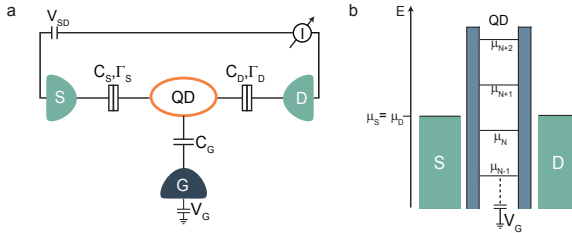


**Figure 2.1. Quantum dot model.** **a** QD schematically coupled to source (S), drain (D) electrode and gate. **b** Schematic of energy diagram with electrochemical potential energies of QD with  $N$  electrons. Adapted from [75, 81].

with  $E_C = \frac{e^2}{C}$  the charging energy and  $\delta E$  the quantum mechanical level spacing. By applying a gate voltage  $V_G$  the ladder can be shifted linearly by  $e\alpha_G\Delta V_G = C_G/C$ , where  $\alpha_G$  is the lever arm of the gate [55, 82].

Additionally, we can see in Fig. 2.2 b, electron transport is only possible when the electrochemical potential of the QD is aligned with the electrochemical potentials of S and D  $\mu_{S/D}$  [55, 81]. This situation is called resonant tunneling and results in peaks of conductance  $G$ , which are called Coulomb resonance peaks [81]. In the case that the electrochemical potentials are not aligned, as shown in Fig. 2.2 a, electron transport is blocked [55]. Consequently, the gate dependent conductance  $G$  reveals Coulomb resonances whenever the QD is on resonance, meaning  $\mu(N) = \mu_S = \mu_D$ , which is shown in Fig. 2.2 c. The Coulomb resonances are separated by  $E_{add}$  and have a two-fold periodic structure (in InAs NWs), due to spin degeneracy. This means, the first electron which occupies a new NW shell needs the addition energy  $E_C + \delta E$ , whereas the next electron only needs  $E_C$  [54, 55, 82].

Up to now, we assumed an isolated QD and neglected the tunnel couplings to source (S) and drain (D)  $\Gamma_{S/D}$ . However, even a small coupling  $\Gamma = \Gamma_S + \Gamma_D$  leads to a finite electron lifetime on the QD, which enables electrons to tunnel on and off the QD, even slightly off-resonance. This results in a finite, intrinsic resonance width (Heisenberg's uncertainty).

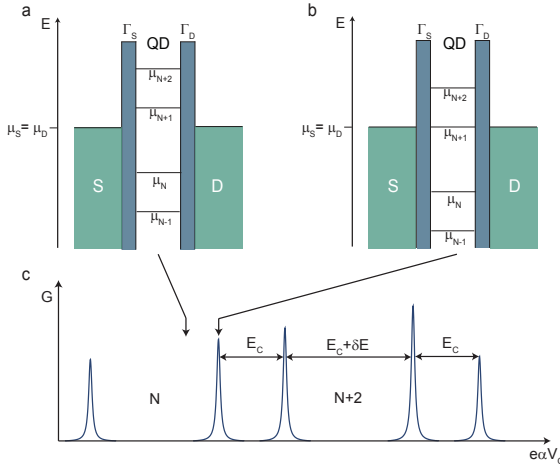


**Figure 2.2. Energy diagram of QD and Coulomb resonances.** Energy diagrams with electrochemical potential of QD not aligned with  $\mu_{S/D}$  **a** and aligned with  $\mu_{S/D}$  **b**. **c** Resulting gate dependent conductance  $G$ . Adapted from [54, 75, 76, 82].

In the limit of  $kT \ll \Gamma \ll \delta E, E_C$ , which holds for sufficiently low enough temperatures, the Coulomb resonance lineshape is described by a Lorentzian [82, 83]:

$$G(V_G) = \frac{2e^2}{h} \frac{\Gamma_S \Gamma_D}{\Gamma_S + \Gamma_D} \frac{\Gamma}{(\epsilon \alpha V_G)^2 + (\Gamma/2)^2}. \quad (2.4)$$

For higher temperatures, the resonance is in addition thermally broadened and takes a different lineshape [83]. The broadening (FWHM) is determined by  $\Gamma$ , whereas the conductance maximum is given by the asymmetry of the tunnel barriers  $\Gamma_S/\Gamma_D$  [76].

Analysing the shape of the peak enables to determine the transport regime as well as the ratio of the coupling parameters  $\Gamma_S/\Gamma_D$  [54]. In a standard two-terminal configuration, it is not possible to assign  $\Gamma_{S/D}$  to the respective electrodes [54, 55, 76, 82].

### 2.1.2. Transport spectroscopy with Coulomb diamonds

It is also possible to lift Coulomb blockade, by applying a source-drain bias  $V_{SD}$ , as schematically shown in Fig. 2.3 [76, 82]. Whenever a chemical potential level, i.e.  $\mu(N)$  enters the opened bias window  $-|e|V_{SD} = \mu_S - \mu_D$ , a step-wise change in current  $I$  is obtained, which results in a peak in conductance  $G$ . Consequently we observe a pattern which is called “Coulomb blockade diamonds”, when the conductance is measured with respect to  $V_{SD}$  and  $V_{BG}$  [84]. Fig. 2.3 presents a schematic of a CB diamond measurement of a QD. Inside of the CB diamond, sequential tunneling is blocked, while outside of each CB diamond the number of electrons is fluctuating [76]. The boundaries of each

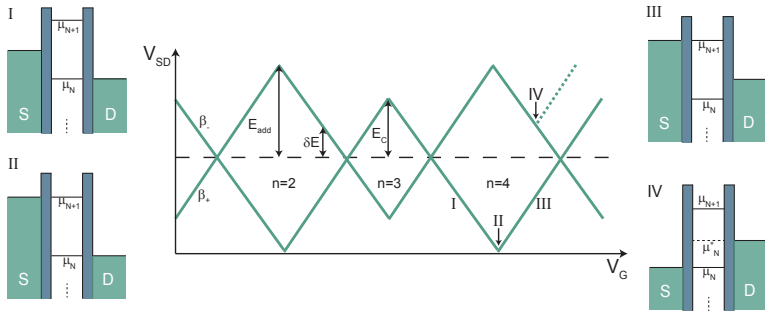


**Figure 2.3. Schematic Coulomb blockade diamonds.** Center: Coulomb blockade diamond with two fold symmetry. Schematics show different situations of applied bias voltage between source and drain. Schematics adapted from [75, 76, 82, 84].

diamond is determined by the condition  $\mu_{QD} = \mu_{S/D}$ , which means, along the positive slope  $\beta_+$  a QD level is aligned with the source  $\mu_{QD} = \mu_S$ , while on the negative slope  $\beta_-$  it is aligned with the drain  $\mu_{QD} = \mu_D$ . Hence, the bias voltage at the tip of the diamond (situation *II* in Fig. 2.3) directly measures the addition energy  $E_{add} = E_C + \delta E$ . This can also be used to extract  $E_C$  and  $\delta E$ , in case the two-fold periodic shell filling is observed [54, 55, 76, 82]. Assuming asymmetric biasing, we can calculate the two slopes  $\beta_{+/-}$ . In this case the shift of the resonance due to the S capacitance needs to be compensated by the gate, leading to [82]:  $0 = -|e|\frac{C_G}{C}\Delta V_G + \frac{C_S}{C}\Delta V_{SD}$  [76]. This gives for the negative slope  $\beta_- = -\frac{C_G}{C_S}$  and for the positive slope  $\beta_+ = \frac{C_G}{C-C_S}$ . Consequently, we obtain for the lever arm of the gate  $\alpha_G = \frac{\beta_+|\beta_-|}{\beta_+ + |\beta_-|}$ . [54, 55, 76, 82].

### Excited states and cotunneling

Until now, we only considered ground state transitions. In case the applied bias voltage is larger than  $\delta E$ , the electrons can also be excited to the consecutive orbital and relax back to the ground state [76, 82]. These excited states can be detected as additional resonances in  $G$  whenever a level of an excited state  $\mu_N^*$  lies within the bias window (shown in Fig. 2.3) [76].

By increasing the coupling  $\Gamma_{S/D}$ , higher order tunneling processes can become possible, like the second order process called “cotunneling” [85]. In this process, the electron is able to escape the QD, even in the CB regime, as long as another electron enters the QD within the uncertainty time  $\sim \hbar/E_C$  [76]. This process gives rise to a current  $\propto V_{SD}$ , and thus a constant  $G$  inside the CB diamond. When the QD stays in the ground state after this process, it is called elastic cotunneling, whereas it is called in-elastic cotunneling, when the QD is left in an excited state [54, 55, 76, 82].

### Kondo effect in quantum dots

Another physical process that can occur, when the coupling of the metallic reservoir to the Quantum Dot is large. This effect is called “Kondo effect” and manifests as an enhancement of the conductance within the blockade regime of a QD for an odd number of occupation [86, 87] (see Fig. 2.4 b). The origin of this is the hybridisation of an unpaired electron and the fermionic ground state of the metallic electrodes, generating a spin singlet ground state [54, 55]. This results in additional transport channel mediated by a spin-flip cotunneling process (see Fig. 2.4 a) [55]. By applying a bias, the electrochemical potentials of the leads are shifted, resulting in a conductance decrease, because the Kondo effect can no longer occur. The FWHM of the Kondo peak can be characterized by the Kondo temperature  $T_K$ . This can be thought of as a

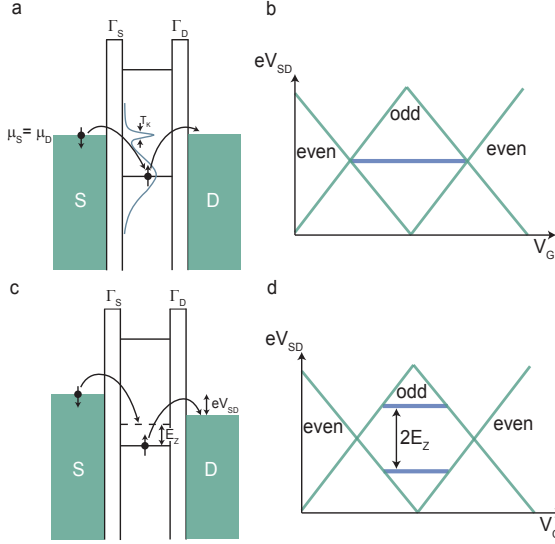


**Figure 2.4. Schematic illustration of Kondo effect in quantum dots.** **a** Schematic energy diagram of a QD with additional DOS at the Fermi level of the leads due to Kondo correlations [86]. **b** Schematic of CB diamonds (green) with Kondo ridge (blue) at zero bias in odd charge state. **c** Energy diagram of spin flip process at applied magnetic field. **d** CB diamonds at finite magnetic field with a Kondo split ridge (blue). Adapted from [54, 55].

crossover temperature, such that Kondo correlations can form. In addition, the Kondo temperature depends on the coupling  $\Gamma$  to the metallic reservoirs as well as  $E_C$  [54, 55, 87]:

$$k_B T_K = 1/2\sqrt{\Gamma E_C} \exp\left(\frac{\pi\epsilon(E_C + \epsilon)}{\Gamma E_C}\right). \quad (2.5)$$

In this expression,  $\epsilon$  is the energy of the occupied level with respect to  $E_F$  of the leads.

The spin degeneracy of the odd level can be lifted by applying an external B field, which leaves the spin down level as an excited state (Fig. 2.4 c) [55]. A spin flip is still possible, leaving the QD in an excited state. The required energy for this inelastic cotunneling process must be provided by the applied bias. Therefore the applied bias  $eV_{SD}$  needs to match the Zeeman energy  $E_Z = g^* \mu_B B$ , which results in an splitting of the Kondo ridge by [54, 55, 86–89]:

$$\delta = 2E_Z = 2g^* \mu_B B. \quad (2.6)$$



As shown in Fig. 2.4 d, the original single Kondo ridge at zero bias voltage (and also  $B = 0$ ), developed into two peaks, separated by  $2E_Z$  for a finite applied magnetic field  $B$  [55]. Furthermore, by following the Kondo splitting as a function of  $B$ , it is possible to extract the effective  $g$ -factor  $g^*$  [54, 55].

## 2.2. Superconductivity

As discussed in the previous section, QDs allow electrons to pass successional due to their large charging energy. In contrast, superconductivity is based on a macroscopic condensate consisting of pairs of electrons. Therefore, coupling a superconductor to a QD results in a conflict of competing transport mechanisms. However, the arising interplay of repulsive and attractive interactions in such hybrid systems enabled observations of interesting effects such as Andreev or even Majorana bound-states [30, 90]. This following section we will give a brief introduction to superconductivity (following Refs. [91, 92]), before we focus on transport phenomena arising in hybrid devices, while following Refs. [54, 76, 81, 82].

The most striking feature of superconductivity is the fact that certain superconducting materials, such as aluminum, lead or niobium have an undetectably small electrical resistance below their critical temperature  $T_C$ . Typical critical temperatures of elemental superconductors are in the range of mK up to 10 K. The first theory describing superconductivity in a macroscopic picture has been invented by Bardeen, Cooper and Schrieffer [82, 93]. Their so called “BCS theory” is based on the following fundamental theorem: the “Fermi sea” (fermionic ground state) is not stable against an attraction of two electrons [76]. Therefore, it is possible that two individual electrons are bound together and form a so-called “Cooper pair”, which no longer follows Fermi-Dirac statistics, but rather Bose-Einstein statistics [93]. Here, the phonons of the ionic lattice are acting as a mediator of this attractive interaction [76, 82]. Intuitively, one can picture an electron moving across the solid, which consequently deforms the lattice of the ion cores with positive charge [76]. This drags a cloud of positive polarization behind its path, which can then attract another electron, as the motion of ion cores lag behind the electron [54]. It is found that the attractive interaction between the electrons is maximized, when one electron has the opposite momentum of the second electron  $\mathbf{k}_1 = -\mathbf{k}_2$  [54, 82]. As a result, the orbital wave function is symmetric and in a spin singlet state  $|\Psi_S\rangle = \frac{1}{\sqrt{2}}(|\uparrow\downarrow\rangle - |\downarrow\uparrow\rangle)$  restoring the antisymmetry required by Pauli’s exclusion principle [54, 76, 82].

As Cooper pairs have a total spin of zero, they can condense into a coherent ground state, which is described by a macroscopic wavefunction. Additionally, the excitation spectrum of a superconductor has a gap around the Fermi energy  $E_F$  of  $2\Delta$ , which is the required energy for excitations of the ground

state, or in other words: to break up a Cooper pair. Their energy dispersion of these so called quasiparticles is described by [54, 82]:

$$E(\mathbf{k}) = \sqrt{\epsilon(\mathbf{k})^2 + \Delta^2}, \quad (2.7)$$

where  $\Delta$  is the superconducting gap parameter and  $\epsilon(\mathbf{k}) = \frac{\hbar^2 k^2}{2m} - E_F$  the energy of a single free electron [91]. Calculating the density of states (DOS) of the quasiparticles  $D_S$  shows that the quasiparticles are separated by  $\Delta$  from the Cooper pair condensate [54, 82]:

$$D_S(E) = D_N(\epsilon) \frac{d\epsilon}{dE} \begin{cases} D_N(\epsilon) \frac{E}{\sqrt{E^2 - \Delta^2}} & (E > \Delta) \\ 0 & (E < \Delta) \end{cases}, \quad (2.8)$$

assuming a constant normal state DOS  $D_N$  around  $E_F$ . For energies  $E < \Delta$ , the DOS is zero and consequently there are only Cooper pairs and no quasiparticles [82]. For energies  $E \rightarrow \Delta$  the DOS diverges and starts to decrease for higher energies until the normal state DOS is resembled for  $E \gg \Delta$ .

Quasiparticle excitation also takes place when the temperature is increased from  $T = 0$ , which reduces the number of Cooper pairs. Hence, the gap  $\Delta$  is becoming reduced until it vanishes at a critical temperature  $T_C$ . The dependence of  $\Delta$  on the temperature is given by [54, 82, 94]:

$$\Delta(T) \approx \Delta_0 \left(1 - \frac{T}{T_C}\right)^{1/2}. \quad (2.9)$$

with  $\Delta_0$  the gap at  $T = 0$ . With further assumptions, one can relate  $\Delta$  to the critical temperature:  $\Delta_0 \approx 1.76 kT_C$ . The BCS theory also provides an additional relevant parameter, which is called the BCS coherence length [92]:

$$\xi = \frac{\hbar v_F}{\pi \Delta_0}, \quad (2.10)$$

where  $v_F$  is the Fermi velocity. The coherence length  $\xi$  is essentially the spatial extension of a Cooper pair and is typically of the order of a few nm to hundreds of nm [76, 82]. Consequently, Cooper pairs are spatially overlapping in the condensate [54, 82].

### 2.3. Transport in superconductor - normal metal structures

In the following section, we first focus on transport phenomena which arises, when a single quantum dot (QD) is embedded between one normal metal (N) and one superconducting (S) electrode. We can categorize different transport regimes, which we distinguish by the coupling strength  $\Gamma$  of the superconducting electrode to the quantum dot [76]. First, we discuss the regime where

S is weakly coupled and transport is dominated by quasiparticle tunneling (Sec. 2.3.1). We then introduce the general concept of Andreev Bound states (Sec. 2.3.3), before we investigate the case of Andreev bound states in strongly coupled S - QD systems (Sec. 2.3.4).

### 2.3.1. Quasiparticle transport

We consider an N - QD - S device with a single QD between a normal metal (N) and a superconducting (S) contact. The QD is characterized by its charging energy  $E_C$  and level spacing  $\delta E$  (as discussed in section 2.1). A schematic of the considered system is shown in Fig. 2.5 a. Here,  $\Gamma_{S/N}$  describes the coupling strength of the QD to the S/N contact with the total coupling strength  $\Gamma = \Gamma_S + \Gamma_N$ . We further denote the electrochemical potentials of the S/N contacts  $\mu_{S/N}$  and the superconducting gap  $\Delta$ . For this section, we restrict ourself to the regime where transport is mainly governed by quaiparticle tunneling and Andreev processes are suppressed due to a weak coupling to the superconductor  $\Gamma_S$  [95, 96]. Hence, this assumption holds for the following relation of the relevant parameters:  $\Gamma_S \ll \Gamma_N \ll \Delta < \delta E \ll E_C$ . Within this limit, transport spectroscopy measurements reveal the quasiparticle DOS in the superconductor [76].

In Fig. 2.5 b a qualitative schematic shows the expected impact of the superconducting gap  $\Delta$  on the shape of the Coulomb resonance. The CB diamond

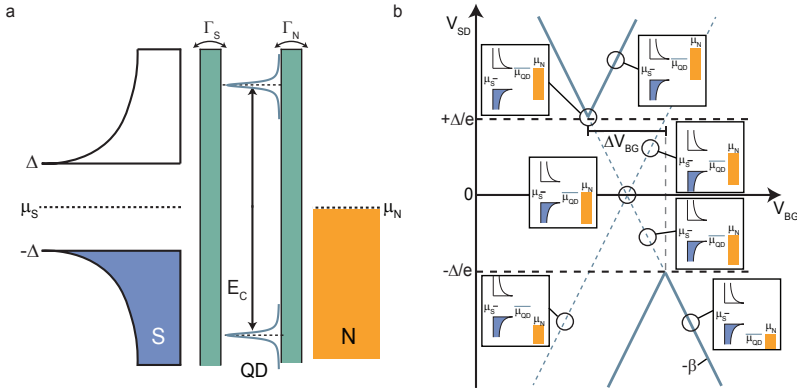


**Figure 2.5. Quasiparticle transport in N - QD - S.** **a** Schematic energy diagram of a superconductor (blue), QD (defined by green barriers) and normal metal contact (yellow). **b** Expected conductance (green solid lines) with respect to source drain bias  $V_{SD}$  and gate voltage  $V_{BG}$ . Adapted from [76, 97].

tips constitute the onset of quasiparticle tunneling, which are consequently shifted by  $2\Delta/e$  in bias. In addition, we expect the Coulomb blockade diamond tips to be shifted in gate voltage  $V_G$ , because of the finite capacitive coupling between both electrodes and the QD [76]:  $\Delta V_{BG} = 2\Delta/\beta_- e$ , with  $\beta_-$  being the negative slope of the CB resonance [97]. This type of system can be further described in a resonant tunneling model (neglecting superconducting correlations and charge dynamics like excited states of the QD), considering single electron transport [95]. Applying the bias to S, the resulting current  $I$  can be written as [76, 95, 97]:

$$I \propto \int dE D_N(E) \cdot D_S(E + eV_{SD}) \cdot T_{QD}(E, V_{BG}, V_{SD}) \cdot [f_N(E) - f_S(E + eV_{SD})], \quad (2.11)$$

where  $D_N(E)$  is the constant DOS of the normal metal contact. The Lorentzian transmission function  $T_{QD}(E, V_{BG}, V_{SD})$  accounts for sequential tunneling via the quantum dot. The Fermi distribution functions of the respective electrodes are taken into account by  $f_{S/N}$ . We further note: here we use an ideal BCS like DOS for the superconducting electrode  $D_S = |E|/\sqrt{E^2 - \Delta^2}$  for  $|E| \leq \Delta$  and  $D_S = 0$  for  $|E| > \Delta$ . As we will see later, the expression for  $D_S$  needs to be adjusted when the DOS that is probed is not BSC-like [76].

### 2.3.2. Andreev reflection

In the following section, we first consider the case of a fully transparent N-S interface and an electron with subgap energy  $E < \Delta$ . When the electron, coming from N, impinges at the S surface, it does not have enough energy to create a quasiparticle and can simply not enter the superconductor. On the other hand, the electron can also not be normal reflected: as the S constitutes a potential barrier of  $\Delta$  with a maximal momentum of  $\delta k \sim \frac{\Delta}{v_F}$ , the required momentum transfer for a normal reflection of  $\sim k_F$  can not be provided [98]. To resolve this, a second order process called Andreev reflection (AR) occurs [100]. The impinging electron can be retro-reflected as a hole, with opposite momentum and spin. The hole will therefore travel backwards with the opposite trajectory as the incident electron (see Fig. 2.6 a, b). In the SC the total charge of  $2e$  is taken up by the formation of a Cooper pair [82].

This transport process is theoretically well described in the BTK model [99]. Here, the scattering potential at the Normal - Superconductor interface is modelled as a  $\delta$  function with the barrier strength parameter  $Z$ , which accounts for elastic scattering processes [76]:  $V(x) = Z\hbar v_F \delta(x)$  [99]. For  $Z = 0$ , no elastic scattering takes place and the only possible process is AR, resulting in a doubling of the current for electrons with energy  $|E| < \Delta$  [54]. In real samples  $Z \neq 0$ , as this would require that both materials are exactly equal and also have the exact same  $v_F$ , resulting in an increase of probability for normal

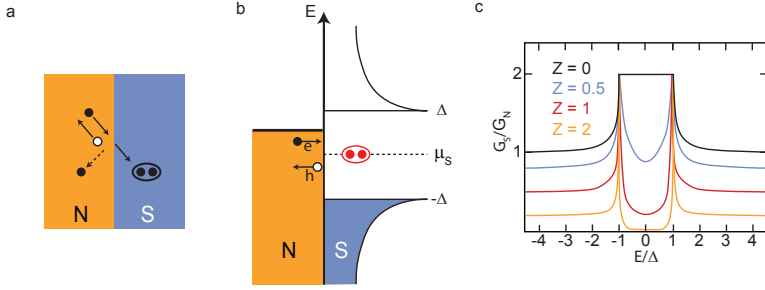


**Figure 2.6. Andreev reflection at superconducting - normal metal interface.** **a** Schematic illustration of Andreev reflection of electron (filled black circle) in real space at Normal - Superconductor interface. Retro-reflected hole is represented as white/black circle. Cooper pair, consisting of two electrons (black circles) depicted in S. Normal reflection is depicted with reflected electron in direction of black dashed line. **b** Andreev reflection in energy space, same notation as in **a**. **c** Normalized differential conductance  $G_S/G_N$  for an Normal - Superconductor junction, based on the BTK model at zero temperature. Curves in different colours show the expected behaviour for several values of the  $Z$  parameter. Adapted from [76, 98, 99].

reflections [54]. For increasing  $Z$ , AR becomes continuously suppressed and one starts to observe the quasiparticle DOS in the S for  $|E| > \Delta$  (see Fig. 2.6 c). This limit describes tunnel spectroscopy experiments in N - insulator - S structures very well [54, 82].

In order to complete this picture, one has to discuss the time reversed process as well. A Cooper pair is removed from the condensate, by an incoming hole and a retro-reflected electron. The AR electron and hole stay phase-coherent for a certain distance and time in the N, corresponding to a non-zero probability to find a Cooper pair in the adjacent N region. Hence, the Cooper pair density decays continuously in N on a length scale of the coherence length  $\xi$ . This is also known as the superconducting proximity effect [101, 102]. This means, superconducting correlations “leak” into the non-superconducting material when it is in electrical contact with a superconductor. In addition, the reverse process can also take place, the “inverse proximity effect”, and results in a decrease of the Cooper pair density in S close to the interface.

### 2.3.3. Andreev bound states

The connection between the proximity effect and AR can be refined, when discussed in a mesoscopic system [103]. In the following section, we assume a mesoscopic Superconductor - Normal metal - Superconductor junction, in which the length  $L$  of the sandwiched Normal segment is shorter than the phase coherence length  $\xi$ , following Refs. [76, 104–106]. We furthermore assume that only a few channels participate to transport, such that the system can be described in a scattering matrix formalism. In addition, we assume a ballistic channel and perfect transmission ( $t=1$ ) in the junctions. We can now ascribe a pairing potential to each of the superconducting contacts  $S_{1/2}$  to  $\Delta_{1/2} = \Delta e^{i\varphi_{1/2}}$ , with  $\varphi_{1/2}$  being the respective phase (see Fig. 2.7). An electron that is moving from left to the right (at low energy  $E < \Delta$ ) will be Andreev reflected at the N-S interface into a hole, moving to the left and thus create a cooper pair in  $S_2$ . When the left moving hole reaches  $S_1$  on the left side, it will be reflected as a right moving electron by taking two electrons from  $S_1$ . Consequently, a pair of charge of  $2e$  is transferred from  $S_1$  to  $S_2$ . The finite length  $L$  of the normal metal segment leads to the generation of discrete energy levels. Depending on the difference in phase  $\varphi = \varphi_1 - \varphi_2$ , standing waves with quantised energies arise in this structure. These subgap states are thus called Andreev bound states (ABS) [107]. The general requirement for the existence of bound-states (in one dimensional systems) is: the acquired phase during one loop must be a multiple of  $2\pi$ . This leads to the following equation [104, 105, 108]:

$$-2\arccos \frac{E_n^\pm}{\Delta} + L(k_+(E_n^\pm) - k_-(E_n^\pm)) \pm (\varphi_1 - \varphi_2) = 2\pi n, (n = 0, \pm 1, \dots) \quad (2.12)$$

with  $k_\pm(E) = k_F \sqrt{1 \pm E/\mu}$  and  $k_F = \sqrt{2m\mu/\hbar^2}$ . Depending on how the process began, the sign of  $\pm(\varphi_1 - \varphi_2)$  corresponds to a left or right moving

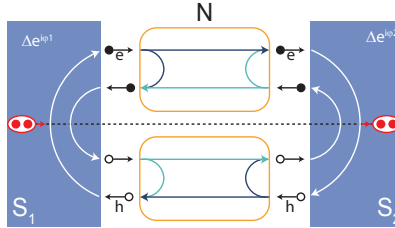


**Figure 2.7. Andreev bound states.** Formation of Andreev bound states in a mesoscopic devices, consisting of normal metal  $N$  sandwiched between two superconductors  $S_{1/2}$ . Adapted from [76, 106].

electron. This equation can be solved for two extreme cases:  $L \rightarrow \infty$  or  $L \rightarrow 0$ . For  $E \ll \mu$  we can approximate the term  $(k_+(E_n^\pm) - k_-(E_n^\pm)) \approx 2E/\hbar v_F$ . We can now characterize such S - N - S systems for the two cases, based on the relation between the length of the normal part  $L$  and the superconducting coherence length  $\xi = \hbar v_F/\Delta$ . The case  $L \ll \xi$  is referred to as the **short junction** limit, whereas the case  $L \gg \xi$  is referred to as the **long junction** limit [109].

In the short junction limit  $L \rightarrow 0$  the second term of equation 2.12 vanishes, resulting in two degenerate ABSs at energies

$$E_\pm(\varphi) = \pm \Delta \cos\left(\frac{\varphi}{2}\right), \quad (2.13)$$

depending only on the phase difference  $\varphi$  of the two superconductors  $S_{1/2}$ . In the long junction limit  $L \rightarrow \infty$ , for  $E \ll \Delta$  we can simplify  $\arccos(E_n/\Delta) = \pi/2$ . This results in the following expression:

$$E_\pm^n(\varphi) = \frac{\hbar v_F}{2L} \left[ \pi(2n+1) \pm \varphi \right], n = 0, \pm 1, \dots \quad (2.14)$$

This describes a set of energy levels which are equally spaced, until they reach  $\Delta$ . Furthermore, the position of these levels is defined by the difference in phase  $\varphi$ . In Fig. 2.8 we present the obtained result for the short Fig. 2.8 a and the long junction limit Fig. 2.8 b.

So far we considered a clean N - S interface with a transmission probability  $t = 1$ . When scattering at the N - S interface is taken into account, the energy of the ABS is given by [107, 108]:

$$E_\pm(\varphi) = \pm \Delta \sqrt{1 - t \cdot \sin^2 \frac{\varphi}{2}}. \quad (2.15)$$

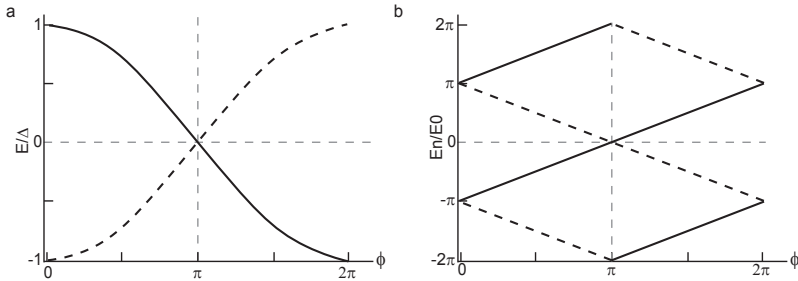


**Figure 2.8. Energy levels for long and short junction limit.** Energy levels of ABS as a function of phase difference  $\varphi$  in the short junction limit **a** and long junction limit **b**. Adapted from [104, 105].

In Fig. 2.9 a the phase dependent energy spectrum, based on this equation is illustrated for different transmission values  $t$ . For low values of  $t$ , the two ABS are very close to the gap edge  $\Delta$ . In a very similar way, one can illustrate the ABS in a mesoscopic N - S junction, with a N-vacuum interface. This is schematically depicted in Fig. 2.9 b.

It has also been shown that this scattering approach can be used to describe a QD as a weak link between two superconductors, assuming that the QD does not interact.

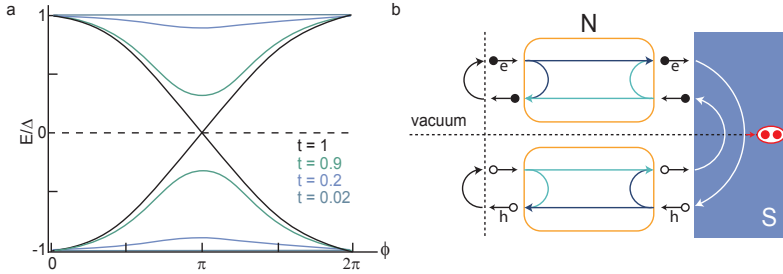


**Figure 2.9. ABS for finite transmission and in N - S system. a** Energy levels of ABS as a function of phase difference  $\varphi$  for different transmission probabilities  $t$ . **b** Formation of Andreev bound states in a mesoscopic N - S device. Adapted from [76, 105, 106].

### 2.3.4. Andreev bound states in S - QD systems

In section 2.3.1 we assumed the coupling of the QD to the superconducting electrode  $\Gamma_S$  to be small. When the coupling strength to the superconductor  $\Gamma_S$  is increased such as  $\Gamma_S \sim \Delta$ , the energy spectrum of the QD is drastically modified [82], as we will present in this section by following Refs. [76, 82, 110, 111]. Just like the metallic normal - superconductor junction discussed in section 2.3.3, the strong coupling  $\Gamma_S$  can also form ABSs, in the quantum dot - superconductor spectrum [76]. ABS in such systems can be directly observed by means of transport spectroscopy, when a normal metal contact is weakly coupled to the this type of system [82, 90].

A QD-S system can be described by the so called superconducting Anderson model [82]. Here, a Hamiltonian of the following form is considered [82, 110]:

$$H_{tot} = H_{QD} + H_S + H_T \quad (2.16)$$



where the QD with a the spin-degenerate single level orbital  $\epsilon_d$  is written as:

$$H_{QD} = \sum_{\sigma} \epsilon_d d_{\sigma}^{\dagger} d_{\sigma} + U n_{\uparrow} n_{\downarrow}. \quad (2.17)$$

In this equation,  $d_{\sigma}^{\dagger}/d_{\sigma}$  are the creation/annihilation operators of the electrons respectively, and  $n_{\sigma} = d_{\sigma}^{\dagger} d_{\sigma}$  the number operator of the QD [82]. The Coulomb interaction of the QD is described by  $U$ , which only appears when an energy level is occupied by two electrons  $n_{\uparrow} = n_{\downarrow} = 1$ .

The superconducting lead itself is denoted by the BCS Hamiltonian [82]:

$$H_S = \sum_{\mathbf{k}, \sigma} \epsilon_{\mathbf{k}} c_{\mathbf{k}\sigma}^{\dagger} c_{\mathbf{k}\sigma} - \Delta \sum_{\mathbf{k}} \left( c_{\mathbf{k}\uparrow}^{\dagger} c_{-\mathbf{k}\downarrow}^{\dagger} + \text{h.c.} \right) \quad (2.18)$$

which is coupled to the QD via the tunnel Hamiltonian [82, 110]:

$$H_T = t_S \sum_{\mathbf{k}, \sigma} \left( d_{\sigma}^{\dagger} c_{\mathbf{k}, \sigma} + \text{h.c.} \right) \quad (2.19)$$

In this equation,  $\Delta$  is the gap of the superconductor and  $\mathbf{k}$  is the wavevector [76, 82]. The tunnel probability  $t_S$  is associated with the coupling as follows:  $\Gamma_S = 2\pi t_S^2 \rho_0$ , where  $\rho_0 = 1/2D$ , representing a constant DOS around the Fermi energy. Unfortunately, the described Hamiltonian  $H_{tot}$  can only be solved either numerically or in a certain limited regime [76].

It has been shown that it is analytically possible to find solutions for the so called “superconducting atomic limit”. Here, the superconducting energy gap  $\Delta \rightarrow \infty$ , which decouples the QD from the quasiparticle continuum. Consequently, one can consider the following effective Hamiltonian [82, 112, 113]:

$$H_{eff} = H_{QD} - \frac{\Gamma_S}{2} (d_{\uparrow}^{\dagger} d_{\downarrow}^{\dagger} + d_{\uparrow} d_{\downarrow}) \quad (2.20)$$

where the second term denotes the proximity effect, which creates and annihilates Cooper pairs on the QD. This process is referred to as virtual Andreev reflections and couples the singlet states  $|0\rangle$  and  $|\uparrow\downarrow\rangle$ , which are no longer eigenstates of the QD as a result, whereas the doublet state  $|\sigma\rangle$  remains an eigenstate (see Fig. 2.10 a). Due to proximity effect, the new doublet state has an eigenenergy of  $E_{\sigma} = \epsilon_d + U/2 = \delta$ . Following the Bogoliubov transformation, one can diagonalize the effective Hamiltonian with the new eigenstates [82]:

$$\begin{aligned} |-\rangle &= u |0\rangle - v^* |\uparrow\downarrow\rangle \\ |+\rangle &= v^* |0\rangle + u |\uparrow\downarrow\rangle, \end{aligned} \quad (2.21)$$

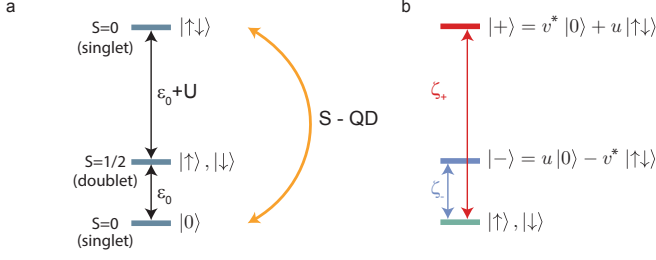


**Figure 2.10. Energy spectrum of QD coupled to S.** **a** Illustration of energy spectrum of single level QD. Virtual Andreev reflections couple even charge states (double arrow). **b** Energy spectrum of coupled quantum dot - superconductor system for superconducting atomic limit [76, 82].  $\zeta_{+/-}$  denote the elementary excitation energies. Adapted from [76, 82, 112].

where  $u, v$  are the Bogoliubov-de Gennes amplitudes  $u = 1/2\sqrt{1 + \delta/\sqrt{\delta^2 + \Gamma_S^2}}$  and  $v = 1/2\sqrt{1 - \delta/\sqrt{\delta^2 + \Gamma_S^2}}$ . The resulting states  $|\pm\rangle$  are Andreev Bound states with respective energy [82, 112, 113]:

$$E_{\pm} = \frac{U}{2} \pm \sqrt{\delta^2 + \Gamma_S^2} + \delta. \quad (2.22)$$

The resulting excitation spectrum is shown in Fig. 2.10 b with the elementary first order transitions  $|\sigma\rangle \leftrightarrow |+\rangle$  and  $|\sigma\rangle \leftrightarrow |-\rangle$  and the respective excitation energies  $\zeta_-$  and  $\zeta_+$ . These excitation energies are measurable as subgap peaks in conductance at  $eV_{SD} = \pm\zeta_{\pm}$  by tunneling spectroscopy in a normal - quantum dot - superconductor system and are referred to as Andreev resonances [82, 111].

### Finite superconducting gap

In the previous section, we considered a infinite superconducting gap  $\Delta$  where quasi particles played little/no role. However, when a finite superconducting gap  $\Delta$  is considered, the interaction with the quasiparticle continuum modifies the energy spectrum of the resulting Andreev resonances [76, 82, 111]. Fig. 2.11 a-c illustrates the expected gate dispersion of Andreev resonances in a N-QD-S device for different ratios of  $\Gamma_S/U$  [82, 111]. For applied bias above  $\Delta$ , standard Coulomb diamonds in a N-QD-S setup are observed. Within the energy window of the gap  $\Delta$ , we see a pair of symmetric Andreev resonances at  $\pm\zeta_-$ . The transition of  $\pm\zeta_+$  is generally not observed, as  $E_+ > \Delta$ . The

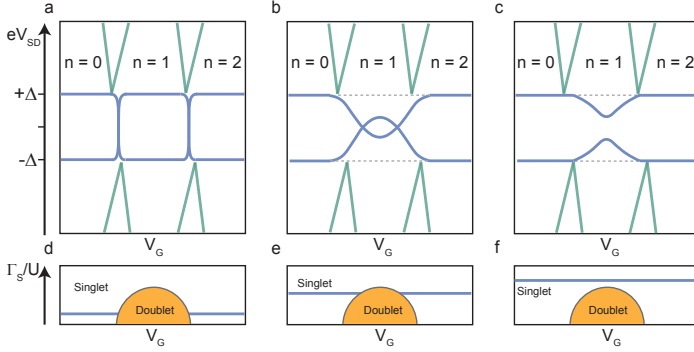


**Figure 2.11. Andreev bound state resonances as a function of gate.** **a-c** Qualitative schematic of gate dispersion of ABS resonances (blue) in charge stability diagram of QD (green). The coupling strength to the superconductor  $\Gamma_S$  is increasing from left to right. **d,e,f** Predicted phase diagram (schematically) and the according ground state with respect to  $\Gamma_S/U$  and  $V_G$  [82]. Adapted from [76, 82, 114, 115].

essential difference to the previously discussed limit (where  $\Delta \rightarrow \infty$ ), the  $\zeta_-$  excitation has now an upper limit of  $\Delta$ . Consequently, the Andreev resonances are pinned to the gap  $\zeta_- \approx \Delta$  in the even charge states (see Fig. 2.11 a-c). The competition between Coulomb repulsion and superconducting pairing becomes visible in the odd charge state, as shown for  $n = 1$  in Fig. 2.11 a-c. For low values of  $\Gamma_S/U$ , a singlet-doublet transition takes place, with  $\zeta_-$  being close to  $\Delta$  (Fig. 2.11 a,d) [76]. When the ratio  $\Gamma_S/U$  is increased (Fig. 2.11 b,e), the  $\zeta_-$  resonance forms a loop in the odd charge state and the singlet-doublet transition occurs within the CB diamond. For large values of  $\Gamma_S/U$ , the ground state remains always the singlet state and  $\zeta_-$  reveals an anti-crossing in the odd charge state [82, 111].

The first experimental detection of ABS in such systems have been demonstrated by [90, 114, 116, 117] in CNT and also in NWs [115]. The physics of ABS is currently of great interest for many research groups, as so called Andreev qubits [118] might provide a possible platform for quantum information processing.

## 2.4. Transport in S - QD - S

In this section, we consider a S - QD - S system, with a single QD between two superconducting contacts  $S_{1/2}$ , schematically shown in Fig. 2.12 b. In such a system, one can distinguish three different transport regimes, depending on the coupling strength  $\Gamma$  relative to the superconducting gap  $\Delta$  and the addition energy  $E_{add}$  of the QD [1, 119]:

- strong coupling:  $\Gamma \gg \Delta, E_{add}$  or  $E_{add} > \Gamma \gg \Delta$ ,
- weak coupling:  $\Gamma \ll \Delta, E_{add}$ ,
- intermediate coupling:  $\Gamma \sim \Delta \sim E_{add}$ .

In the following, we will describe the basic characteristics of each of the three transport regimes, following Ref. [119].

### 2.4.1. Strong coupling regime

In the strong coupling regime  $\Gamma \gg \Delta, E_{add}$  or  $E_{add} > \Gamma \gg \Delta$ , the Coulomb blockade effect can be neglected and the system behaves like a S - N - S junction, as illustrated in Fig. 2.12 a. When the length of the junction (also referred to as “weak link”)  $L$  between the two superconductors is smaller than the coherence length  $L < \xi$ , a supercurrent can flow between both superconducting contacts  $S_{1/2}$  (at  $V_{SD} = 0$ ) transferring Cooper pairs from one contact to the other. This effect is well known as the Josephson effect and can also be observed when the weak link is made of an insulating barrier [92] or in our case a semiconducting NW [3, 119].

Following the ABS description of section 2.3.3, we can describe the resulting

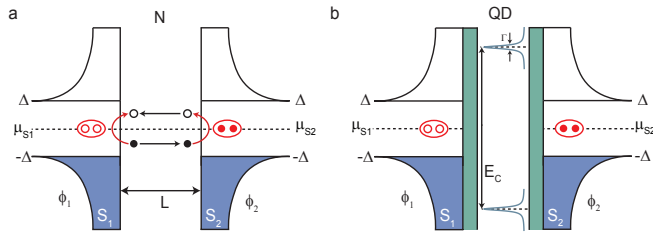


**Figure 2.12. Energy diagrams for Josephson junctions.** **a** Schematic energy diagram of S - N - S structure with supercurrent carrying ABS. **b** Energy diagram of QD between two superconductors  $S_{1/2}$ . Adapted from [119].

supercurrent with the the following equation [81, 92, 105]:

$$I_S = \frac{2e}{\hbar} \sum_{\pm} \frac{\partial E(\varphi)}{\partial \varphi} \tanh\left(\frac{E_{\pm}}{2k_B T}\right). \quad (2.23)$$

This can be simplified, for low temperatures and for the absence of quasiparticle exchange between the superconductors and the ABSs, where exclusively  $E_-$  is transmitting the supercurrent [81]. In case the transmission coefficient  $t \ll 1$  (tunnelling limit), we arrive at the first Josephson equation, the DC Josephson current [81, 92]:

$$I_S(\varphi) = I_C \sin(\Delta\varphi). \quad (2.24)$$

Here,  $I_C$  is the maximal critical current:  $I_C = e\Delta t/2\hbar$ . The supercurrent  $I_S$  depends on the phase difference  $\Delta\varphi = \varphi_2 - \varphi_1$  of the two superconductors  $S_1$  and  $S_2$ . When the junction is biased with a voltage  $V$ , the phase varies:  $\frac{d\Delta\varphi}{dt} = \frac{2eV}{\hbar}$ . This is known as the second Josephson equation or the AC Josephson effect [81, 92].

### 2.4.2. Weak coupling regime

In the weak coupling regime  $\Gamma \ll \Delta, E_{add}$ , the Josephson effect is suppressed by the Coulomb interaction and transport is mainly governed by quasiparticle transport when  $|V_{SD}| > 2\Delta$  (c.f. situation *I* in Fig. 2.13). However, it has also been shown that coherent tunneling of Cooper pairs can, in fact, occur when the QD is on resonance with the Fermi energies of the superconductors [97, 120]. For now, we only consider quasiparticle transport [95, 96]. In Fig. 2.13 we provide a schematic illustration of a S - QD - S device in this regime assuming two S contacts  $S_{1/2}$  with the same superconducting gap  $\Delta_{1/2}$ . We observe that the tips of the diamond are separated in energy by:  $eV_{SD} = \pm 2\Delta$ , but effectively not shifted in gate voltage  $V_G$ . As a reference, the green/blue dashed lines show the expected resonances of an N - QD - S device for the right/left contact being a normal metal. We can describe this type of system, using a resonant tunneling model, similar to the one used in Sec. 2.3.1, by replacing the constant DOS of the normal metal in equation 2.11, by the DOS of a second superconducting electrode [119].

### 2.4.3. Intermediate coupling regime

In the intermediate-coupling regime  $\Gamma \sim \Delta \sim E_{add}$ , the situation is more complex as all relevant energy scales are comparable. Transport is dominated by the competition between repulsive interactions of electrons confined in the QD and pairing of electrons due to superconducting order. For example, in this regime transport processes like resonant Andreev tunneling have been

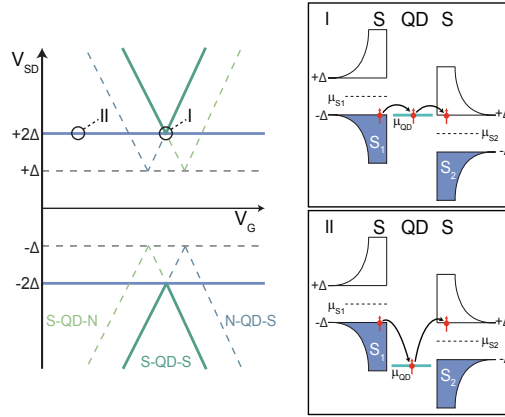


**Figure 2.13. Quasiparticle transport S - QD - S.** a Schematic depiction of expected charge stability diagram for quasiparticle tunneling. Shifted CB diamond tips depicted in green, whereas quasiparticle tunneling in the Coulomb blockade region is shown in blue. On the right: Schematic energy diagrams for two distinct situations, as depicted in a. Adapted from [1, 39, 119].

detected recently [97].

Generally in such devices, a quasiparticle current can be observed within the Coulomb blockade diamonds due to second order cotunneling processes (see section 2.1.2). In the superconducting phase of both contacts, a minimum bias voltage of  $2\Delta$  is required in order to bring the occupied states of the source into resonance with the unoccupied states of the drain (situation II in Fig. 2.13). In contrast to single-electron tunneling, this threshold does not depend on the applied gate voltage  $V_G$  [1, 121, 122]. We schematically indicate the expected elastic cotunneling current at the onset of  $eV_{SD} \pm 2\Delta$  in Fig. 2.13. In addition, negative differential conductance along the gap edge has been observed in this type of systems and can be attributed to peaks in the DOS [43, 123–125]. For a more complete overview of this regime, we refer to Refs. [1, 119].

## 2.5. Crossed Andreev reflection

Considering the spatial extension of Cooper pairs, it is clear that the hole can also be reflected within a length  $l < \xi$  [54]. When devices with multiple terminals are used, this can happen in different leads, resulting in cross conductances based on this non-local AR process called crossed Andreev reflection (CAR).

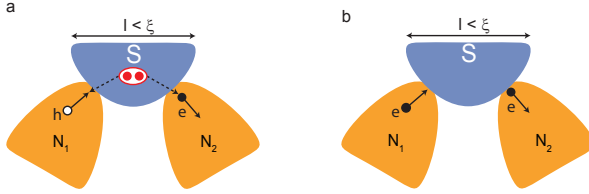


**Figure 2.14. Schematic of crossed Andreev reflection.** **a** Splitting of a Cooper pair by impinging hole from  $N_1$  to  $S$  and reflected electron into  $N_2$ . **b** Elastic cotunneling of electron coming from  $N_1$ , being transmitted to  $N_2$  via virtual state in  $S$ . Adapted from [76, 82]

For example, one can consider a multi-terminal system as shown in Fig. 2.14 a. A single superconducting contact is connected to two individual normal metal leads  $N_{1,2}$ , where the hole which is arriving at  $N_1$  can be retroreflected as an electron to  $N_2$  [54]. In other words, this can be described as a Cooper pair, originating from  $S$ , which is split into 2 different normal metal electrodes [76]. Since the process is still phase coherent, this platform can be potentially used as a source for spatially separated spin-entangled electrons [54, 76, 82].

In purely metallic N - S - N structures, crossed Andreev reflection is difficult to detect, because it competes with elastic cotunneling which has a similar probability amplitude (see Fig. 2.14 b).

### 2.5.1. Cooper pair splitting using quantum dots

The following section follows the explanation from Refs. [54, 76, 82] on “Cooper pair splitting” using QDs. As discussed in the previous section, crossed Andreev reflection can be used as a basic mechanism for the creation of spatially separated spin entangled electrons in metallic structures. Unfortunately, these metallic systems offer nearly no control over the present transport mechanisms. Hence, it is hard to identify CAR from local processes. To circumvent this problem, the theoretical proposal of Recher et al. [126] suggested to add QDs as a controllable energy filter between the superconductor and the normal metal leads. In Fig. 2.15 a a schematic of such a system is presented, which we will refer to as the Cooper pair splitter (CPS) from here on. The illustration also contains the most important device parameters: the coupling between each QD to the superconductor  $\Gamma_{S1/2}$  and to the normal metal leads  $\Gamma_{N1/2}$ , as well as the coupling between the QDs  $\Gamma_{12}$ . Each of the the QDs have an individual charging energy of  $E_{C1/2}$  and the electrochemical potential of each QD  $\mu_{QD1/2}$  can be tuned separately by local gates. Furthermore, the spatial distance between the tunneling points is denoted as  $\delta r$ .

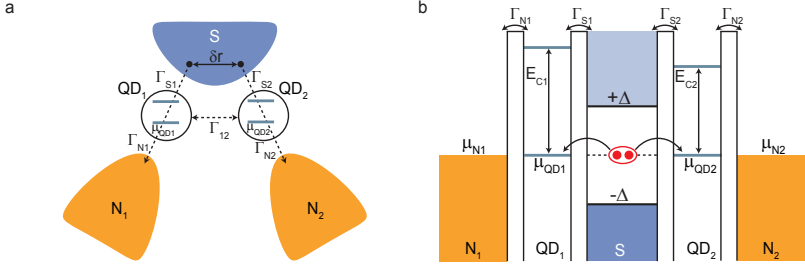


**Figure 2.15. Cooper pair splitting with QDs.** **a** Schematic of Cooper pair splitter setup with two QDs,  $QD_{1/2}$  coupled to normal metal leads  $N_{1/2}$ . **b** Energy diagram of CPS process. Adapted from [54, 76, 82].

The basic principle of a CPS relies on the following idea: due to the present on-site Coulomb interactions of the QDs, a double occupancy of the individual QDs is prohibited which should enhance the CAR transport process. Therefore, by adjusting the QD characteristics and device parameters, local tunneling of Cooper pairs into the same normal lead can be suppressed. This local pair tunneling (LPT) can occur via two different channels. One possibility is, that a cooper pair tunnels simultaneously to the same QD, which is suppressed by Coulomb interaction  $\sim E_C$ ; a parameter adjustable by the size of the QD. The second possibility is that the Cooper pair is broken and one electron tunnels after the other through the same QD [54]. This only works when the second electron is excited into a quasi-particle state with energy larger than  $\Delta$ , while the other electron can tunnel through QD [54]. This sequential tunneling process is therefore suppressed by the quasiparticle excitation energy  $\sim 1/\Delta$ . A quantitative description can be found in Refs. [54, 82].

It has also been theoretically proposed that a higher order CPS process "quartets" can occur in junctions made of three superconducting electrodes [127, 128]. First signatures of this non-local CPS have been recently reported in InAs NW multi-terminal superconducting junctions [129].



# 3 Fabrication

---

In the following chapter we will discuss the methods which are used to fabricate nano-scale samples, which are investigated within this thesis. First, we present the fabrication process of standard nanowire devices, using InAs nanowires. Within the scope of this thesis, we mainly fabricated InAs nanowire devices with either one superconducting and one normal metal contact, or two superconducting contacts. In both case, the fabrication steps are very similar. We further discuss an established etch process of InAs nanowires with an epixal shell, made of aluminum. To conclude, we present a brief introduction to the basics of cryogenic measurement techniques.

## 3.1. Device fabrication

The most important tool which is needed to fabricate nano-scale devices, is electron beam lithography (EBL). We used this technique to fabricate devices consisting of a single InAs NW with two electrical contacts. In order to place the contacts with the desired size at the correct location, we have to perform a sequence of EBL steps, as described in the following section.

### 3.1.1. Standard nanowire devices

#### Wafer cleaning

All of the discussed devices were fabricated on a highly p-doped silicon wafer. The silicon wafer has a 400 nm thick capping layer made of silicon oxide ( $\text{SiO}_2$ ) which is used as the gate oxide for the global backgate. After cleaving the wafer into smaller pieces ( $2.5\text{ cm} \times 2.5\text{ cm}$ ), the surface of the wafer is cleaned by immersing it in acetone and placing it in a ultrasonic bath for 10 min. Then, it is rinsed in isopropanol (IPA) and exposed to an UV/ozone plasma for 5 minutes.

#### Base structure fabrication

Standard EBL is used to define a marker grid, which is required to localize the nanowires with high precision and to align the following EBL steps. For

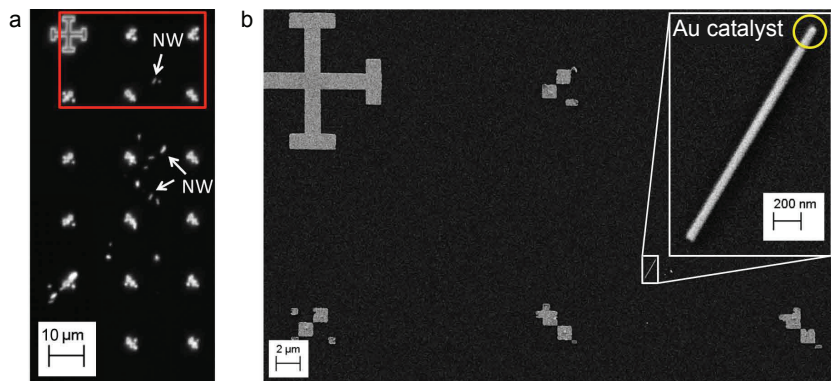


**Figure 3.1. Base structure layout.** **a** Optical microscope image of base structure with markers and NWs. **b** SEM image of area marked with red in **a**. Inset shows SEM image of single NW with an Au catalyst particle on the end.

a more detailed description on the EBL process we refer to other PhD theses of our group [54, 55, 76]. The markers are arranged in a square pattern, have a spacing of  $20\text{ }\mu\text{m}$  (see Fig. 3.1), and cover an area of  $400\text{ }\mu\text{m}\times 400\text{ }\mu\text{m}$ . Around this pattern, the “outer” contact leads and bond pads are predefined as well (see Fig. 3.2 b). A single base structure, including bond pads, has a size of  $2.5\text{ mm}\times 2.5\text{ mm}$ , meaning one can define about  $\sim 50$  base structures on one piece of wafer. Subsequently, a titanium/gold layer ( $5\text{ nm}/45\text{ nm}$ ) is evaporated onto the wafer.

### NW deposition and read out

In order to transfer the NWs from the growth wafer to one of the base structures, we used the tip of a cleanroom tissue. By touching the growth chip with the tip of the tissue, several NWs break off from their growth origin and become attached to the tissue. By dabbing the tissue tip on the marker area of the base structure, the NWs detach and stay on the sample surface. A coarse localization of the transferred NWs can be done with the optical microscope (Fig. 3.1 a). Afterwards, the precise NW localization was extracted by using a SEM image. It is important to know on which end of the NW the Au-particle is located (see inset of Fig. 3.1 b). This information is required, because the location of the in-situ grown QD is known with respect to the gold catalyst (as discussed in detail in chapter 4). For designing the contacts, we read out the NW position with respect to the small markers of the grid by

using a Python based program written by O. Faist.

### Contacting InAs nanowires

In order to make electrical contact to NWs, one has to remove the 2 nm to 3 nm thick native oxide, which is formed, after the NWs have been taken out of the growth chamber. In principal, there are several ways to remove the native oxide prior to metallization. One can either use a wet etch method called “sulphur passivation”, which consists of a  $\text{NH}_4\text{S}_x$  solution [130]. Another possibility is to use an in-situ argon plasma, which mechanically removes the oxide with a directed bombardment of argon ions. Both methods are well established in our group and details can be found in the appendix in section A.4.

The contacting method has a strong influence on the electrical behavior of the NWs. Using the sulphur passivation, the contact area<sup>1</sup> is doped by the remaining sulphur atoms, such that the Fermi energy is shifted further up in the conduction band. This helps to achieve good ohmic contacts, whenever we use InAs NWs grown in WZ crystal phase, having lower electron densities, compared to ZB. In this case, using the argon plasma seems to deplete the NW contact area, making it more difficult to get good contacts.

On the other hand, when we use InAs NWs which are mainly grown in the ZB crystal phase, sulphur passivation is counterproductive. As InAs in ZB has an intrinsically higher electron concentration, the Fermi energy is shifted so far up in the conduction band (when using sulphur passivation) that it is difficult to deplete the NWs afterwards. Therefore, all measurements involving NWs with crystal phase defined QDs are contacted by using argon plasma. Recently we also began to work on a wet etch process based on HCl for NWs consisting of ZB crystal phase, following the recipe of Ref. [25], but did not explore this in great detail yet.

As a normal metal contact, we mostly used a bilayer consisting of titanium/gold (5 nm/80 nm). The final evaporation step is the superconducting contact, which is a titanium/aluminum (5 nm/90 nm) bilayer. Further details of the etch recipes and parameters of the evaporation process can be found in the Appendix (see section A.4).

### Chip carrier

As a last fabrication step, the sample wafer is cleaved into smaller pieces (4 mm×4 mm), in order to fit in the chip-carrier. Then the sample is glued into the chip-carrier with silver paste to ensure electrical contact to the substrate, which we are using as a backgate [54, 55]. The contact pads of the sample are then connected to the chip-carrier via standard wire bonding by using a gold

<sup>1</sup>and maybe also parts of the NW, caused by  $\text{NH}_4\text{S}_x$  creeping along the NW below the resist etch mask

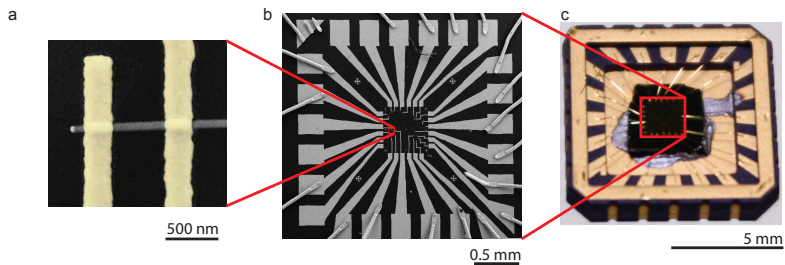


**Figure 3.2. Device in a chip carrier.** **a** Scanning electron micrograph of NW device with evaporated titanium/gold (yellow) contacts. **b** Bonded base structure with leads to devices. **c** Chip which is glued into the chip carrier by silver paste and bonded with gold wires. The backgate is connected via silver paste to one of the contact pads.

wire (see Fig. 3.2 c). The chip-carrier has 20 contact pads (due to the fact that the cryostats are wired with a total number of 20 electrical lines), which limits the number of possible devices to a maximum of nine (for the simplest possible two terminal devices), since one line is used for the backgate. After bonding, one has to take special care of electrostatic discharge (ESD) which can easily blow up devices. Therefore, it is recommended to ground everything properly and wear ESD safe shoes. Once the sample is ready to be measured it is either stored in a vacuum chamber to avoid oxidization or directly built into a cryogenic measurement set-up which is discussed in the last part of this chapter.

### 3.1.2. Epitaxial Al shell devices

The following subsection will discuss the established etch process of an aluminum shell, which is grown epitaxially on InAs nanowires. The recipe is based on information we received from Dr. M.T. Deng from the University of Copenhagen. The etch process was adapted and established in our group together with R. Haller. The NWs discussed below have been grown by Prof. P. Krogstrup and thankfully provided by Prof. J. Nygård (University of Copenhagen.)

In contrast to standard NW devices, where the electrical contact is evaporated after removing the natural oxide of the NW (as discussed in the previous section), it has been demonstrated a few years ago that it is possible to grow the contact material epitaxially within the growth vacuum chamber, before the NW surface becomes oxidized [26]. This is of special interest when the contact material is a superconductor, as in this case aluminum.

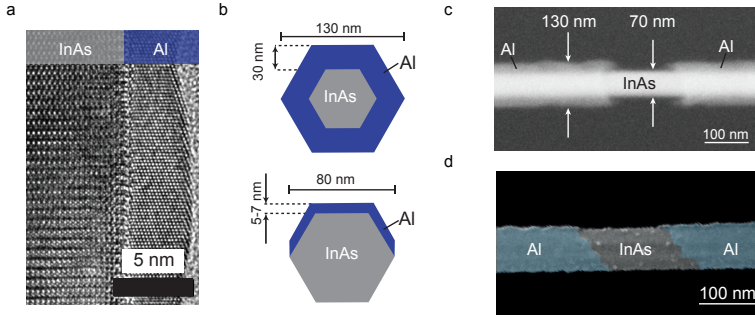


**Figure 3.3. InAs NW with epitaxial aluminum shell.** **a** Transmission electron micrograph of interface between InAs NW and epitaxially grown, provided by P. Krogstrup. **b** Schematic of NW with full Al shell (top) and half shell (bottom). Scanning electron micrograph of selectively etched NW devices with Al full shell **c** and half shell **d**. SEM images done by R. Haller.

Fig. 3.3 a shows the transmission electron micrograph of an epitaxially grown aluminum shell on an InAs NW, which shows no defects or perturbations at the interface. Fig. 3.3 b shows schematic cross sections of two different types of aluminum shell NWs: in the top panel, the aluminum covers all facets of the NW and is grown  $\sim 30$  nm thick (which we will refer to as “full shell”), whereas in the bottom panel the aluminum covers only three facets and is grown with a thickness of 5 nm to 7 nm (referred to as “half shell”).

In order to fabricate functional devices, based in this type of NWs, one needs to selectively remove the aluminum shell, which can be challenging, especially for small trenches, due to possible over etching. In the following we will now describe the established fabrication process of InAs NWs with an epitaxial aluminum shell.

After standard NW deposition and location read out, the etch mask needs to be defined by EBL resist. Since it is a wet etch process, it is crucial to have a good adhesion between the etch mask and the NW to prevent the etchant from creeping along the NW, resulting in an uncontrolled over-etching. Therefore, we use the commercially available MMA based resist called EL6 from the company MicroResist, which adheres better than the PMMA etch mask. Furthermore, the resist is less viscous as PMMA, which may lead to better coverage of the NW. Since a certain resist thickness is required, the resist is spun twice and baked on a hotplate at  $180^\circ$ . This results in an etch mask thickness of  $\approx 250$  nm. By performing standard EBL writing, square shaped etch windows or lines (for small trenches) are opened in the etch mask. After development,

remaining resist residuals are removed by an oxygen plasma. Before the etch process itself is performed, it is important to prepare two additional beakers with DI water, next to the beaker with the etchant. As an etchant the TMAH based optical developer MF321 is used. This etchant has several advantages in comparison to the otherwise widely used “Transine aluminum etch type D”: it can be used at room temperature, has an etch time of around of roughly one minute and degrades on a longer timescale. During the etch process, the etchant is constantly stirred with a magnetic stirrer to provide fresh etchant to the etch-window. For the half shell NWs, we immerse the sample with a metal tweezer vertically in the etchant for 75 s (full shell: 85 s). Subsequently, the sample is immersed in the first water beaker for 20 s and heavily shook to stop the etch process as fast as possible. Next, the sample is immersed in the second water beaker for another 30 s to dilute the remaining etchant.

As a final step, the etch mask is removed by hot acetone. Fig. 3.3 c shows a SEM image after a full shell NW has been etched. A gap of about 100 nm has been opened successfully, without over-etching the Al shell. Fig. 3.3 d presents a SEM micrograph of a half shell NW, which has been etched as well. For further details on the process see appendix A.5.

To demonstrate the success of this fabrication process, we present a measurement of a device with one contact made of a normal metal (titanium/gold) and the other one formed by the epitaxial aluminum full shell (shown in Fig. 3.4 a). In Fig. 3.4 b we present the measured normalized (by the normal state differential conductance  $G_N$ )  $G$  with respect to the bias voltage  $V_{SD}$ , revealing a hard superconducting energy gap of  $\Delta \approx 170 \mu\text{eV}$ . We further observe a conductance suppression of about  $\sim 100$  inside the superconducting energy gap, similar to Ref. [131].

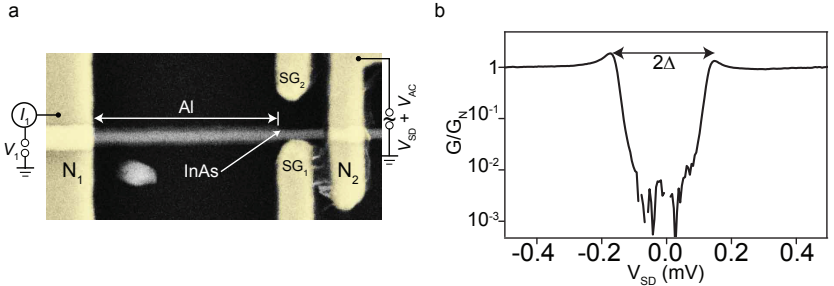


**Figure 3.4. Hard gap in InAs NW with epitaxial aluminum shell. a** Device consisting of InAs NW with Al shell and a bare InAs NW segment of about 300 nm. **b** Normalized  $G/G_N$  with respect to source drain bias voltage  $V_{SD}$ .

### 3.2. Cryogenic measurement set-up

To be able to measure quantum mechanical effects, not only the temperature of the crystal lattice, but also the electronic temperature must be sufficiently low. Here, we give a short description of the cryogenic measurement setup, which was used within this thesis and refer to other PhD thesis of our group for more detailed information [54, 76, 132] .

As liquid  $^4\text{He}$  has a temperature of 4.2 K, we can cool down the sample to this temperature very fast. When we start pumping on the surface of the liquid helium, we remove latent heat because of the evaporation and the temperature of the liquid gets reduced to  $\approx 1.4$  K. We can reach lower temperatures, by using so called “dilution refrigerators”. The working principle is based on a mixture of  $^3\text{He}$  and  $^4\text{He}$ . At a temperature of about  $\sim 870$  mK this mixture is separated in one phase which is rich of  $^3\text{He}$  and another one which is  $^3\text{He}$ -poor [132, 133]. The cooling power is generated by the dilution of the  $^3\text{He}$  from a  $^3\text{He}$ -rich to the  $^3\text{He}$ -poor phase. Due to this, we can reach a base temperature of  $\approx 20$  mK.

Once the chip-carrier (Fig. 3.2 c) is mounted to the holder of the cryogenic insert, it is electrically connected to a so called “break-out box” [54, 132]. From here on, we can use BNC cables to connect all required measurement electronics. All measurement lines inside the insert of the cryostat are thermalised at the coldest accessible place of the insert. In order to protect the sample from radiation of high frequencies a few stages with filters are mounted [132]. The break-out box has a commercially available filter-stage with a cut-off frequency of around 1 MHz. In addition, we employ tape-worm filters, which are manufactured in-house, having a cut-off frequency of 10 MHz [54, 76, 132]. Furthermore, the devices are protected from thermal radiation by a Faraday cage. Typically, we reach electronic temperatures below 100 mK in our setups.

In order to measure differential conductance/resistance, we used low-frequency lock-in techniques (lock-in: Stanford SR830). In Fig. 3.5 we show an illustration of a typical measurement setup. Within the detection setup, we used low-noise and low-drift I/V-converters and voltage amplifiers, manufactured by the in-house electronics workshop. As a DC bias source we use the commercially available Yokogawa YK7651. The AC voltage was superimposed on the DC voltage by using a standard transformer. The DC gate voltages are applied via a high-resolution DAC, which is also home built by the electronics workshop. We controlled all measurement units by home made routines written in Igor Pro on the computer. For a more detailed description of the measurement setups we refer to Refs. [76, 132]

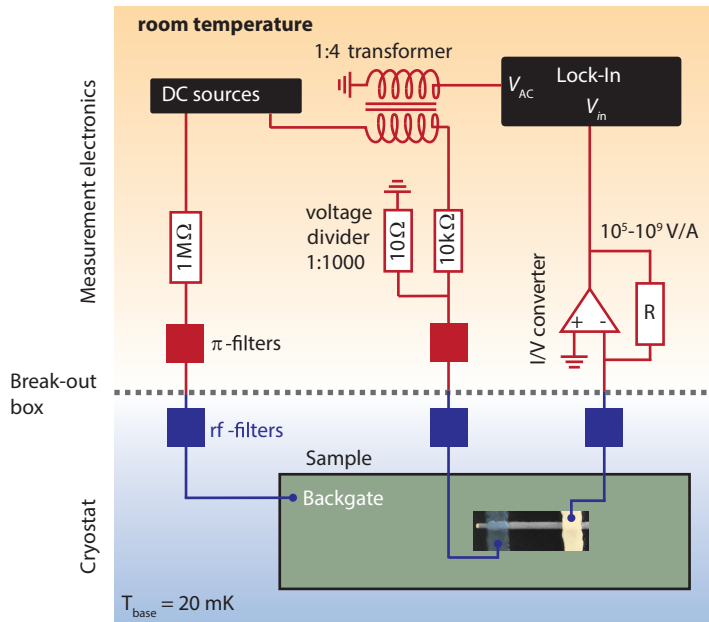


**Figure 3.5. Schematics of a cryogenic measurement set-up:** Schematic depiction of standard measurement. The measurement configuration shows a  $G$  measurement with applied  $V$  bias at cryogenic temperatures [76, 132]. Image adapted from [76, 132].



## 4 Crystal phase defined quantum dots

---

In the following chapter we discuss the material platform which gives the basis for most experiments performed in this thesis: InAs nanowires with quantum dots defined via controlled tunnel barriers, based on the alternation of crystal phases [59]. Here, the QD is formed in between two wurtzite (WZ) segments, in the otherwise zinc-blende (ZB) nanowire. First, we present basic properties of both crystal phases and afterwards show how we extract the dimensions and position of the QD using sophisticated SEM techniques. The last part focuses on the characterization measurements of the specific nanowires we were using. One of the main goals of this thesis was to perform spectroscopy measurements using a well defined QD, in order to probe the DOS in the NW lead segment. Until now, most spectroscopy studies in such systems have been performed by either using QDs formed by electrostatic gates [30, 40–43] or by the source drain contacts themselves [39]. However, both approaches have disadvantages, creating difficulties in the interpretation of the spectroscopic results: barriers defined by electrostatic gates are not sharp, the QDs are sensitive to electrostatic fluctuations, the precise location and size is unknown and they are highly non reproducible (especially in the case of source-drain defined QDs). Therefore, the origin of the measured DOS is unclear.

To resolve these issues, we use QDs defined by integrated tunnel barriers. Due to recent advances in synthesis, it is possible to grow such QDs by a controlled switching between the WZ and the ZB crystal phase of InAs [58]. In this system, the WZ segments define a potential step for the electrons, as this crystal phase induces a positive conduction band offset in the bandstructure, resulting in the formation of a QD in between the WZ barriers. Most importantly, the QDs dimensions and location are defined with atomic precision. Furthermore, we can precisely locate its position, making this the ideal platform to perform tunneling spectroscopy in NWs.

The NWs presented here, are grown and developed by the group of K. Dick-Thelander, S. Lehmann, M. Nilsson and C. Thelander (University of Lund), who thankfully provided the NWs. We therefore follow the explanation of Ref. [59] in the following part of this chapter.

### 4.1. Zincblende and wurtzite crystal phase of InAs nanowires

The two important crystal phases here are ZB and WZ, which are described by the sequence of the atomically layered stacks. The WZ crystal phase is a hexagonal close-packed (hcp) structure (see Fig. 4.1 a top) whereas ZB is a cubic close-packed (ccp) structure (see Fig. 4.1 a bottom). In the WZ case, the bilayers follow a ABAB order, whereas ZB follows a ABCABC order (see Fig. 4.1 b). This so called homostructure is grown by metal-organic vapour phase epitaxy (MOVPE) [59]. The details of the growth process can be found in Ref. [59, 134]. First, the growth substrate with the gold catalyst particles was annealed ( $\sim 550^\circ\text{C}$ ) such as contaminations are desorbed from the surface and to melt the Au particles. For the nanowires within this thesis Au aerosol particles of  $\sim 40\text{ nm}$  diameter as seed particles were used. The Au seed particles had a variation in diameter of about  $2\text{ nm}$  to  $3\text{ nm}$  and were randomly distributed on the growth substrate. During the annealing process an over-pressure of  $\text{H}_2$  and Arsine ( $\text{AsH}_3$ , the As precursor) was maintained. Afterwards, the temperature was kept at constant temperature of  $\sim 460^\circ\text{C}$  for the entire process. Next, the indium - precursor trimethylindium ( $\text{TMIn}$ ) was introduced. When coming into contact with the substrate, the vapor-phase precursors decomposed into In and As, diffused and dissolved in the gold catalyst. When the gold particle is supersaturated by In and As, local nucleation begins to form at the interface of the substrate and the Au particle. The epitaxial growth of the NW continues, until no new material is supplied. The

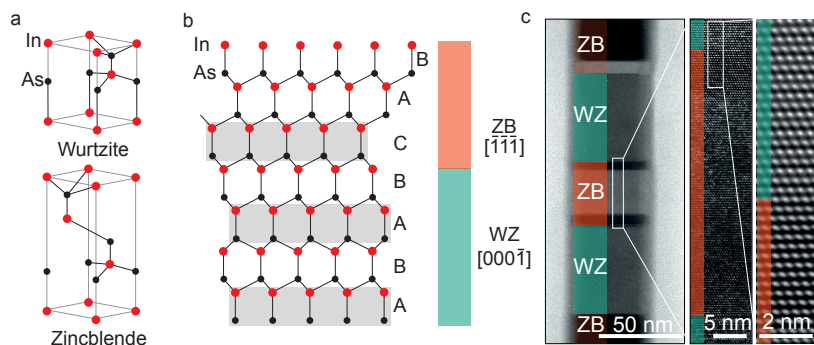


**Figure 4.1. Wurtzite and zinc-blende crystal structure.** **a**, Schematic of wurtzite and zincblende crystal phase. **b** Schematic of a stack of WZ and ZB. The respective sequences ABAB (wurtzite) and ABCABC (zinclende) are marked. **c** TEM micrograph of a QD (ZB segment in the middle) in nanowires. Freely adapted from [59, 81, 135]; TEM image provided by S.Lehmann [136].

crystal phase can be controlled in various ways. Typically, NWs with smaller diameters tend to grow in the WZ phase, while NWs with larger diameter tend to grow in ZB phase [137]. One can modulate the crystal phase by tuning the temperature [138] or incorporate dopants [135]. In this thesis, we used NWs where the crystal phase was controlled by changing the ratio of the In/As precursors, whereas ZB is grown with a higher In/As precursor ratio. Due to technical advances of this method, one can controllably switch between ZB and WZ with atomically precision (see Fig. 4.1 c on the right) [58, 138]. Fig. 4.1 c shows transmission electron micrographs (TEM) of a NW with a built-in QD defined by WZ (green) tunnel barriers and a ZB (orange) segment in between, in which the QD will be formed.

## 4.2. Crystal phase defined quantum dots

This section will discuss, how a QD is formed inside an InAs NW, when controlling the crystal phase along the growth direction. Segments of WZ crystal phase, in a otherwise ZB InAs nanowire, act as hard wall potentials to electrons, as the bandstructure of both phases is aligned with an offset (positive) of 126 meV in the conduction band, according to theoretical calculations [139, 140]. Growing two segments of WZ crystal phase, with a ZB segment in between, consequently results in the formation of a QD in the ZB segment. In Fig. 4.2 a we present an illustration of a QD formed within two WZ barriers. We assume that the WZ segments create a square shaped, hard wall potential at the edge of the conduction band (see Fig. 4.2 b). Experimentally, first measurements have been reported in Ref. [23], whereas a barrier of potential of at least  $\sim 95$  meV [25] has been found, similar to the value obtained by thermionic

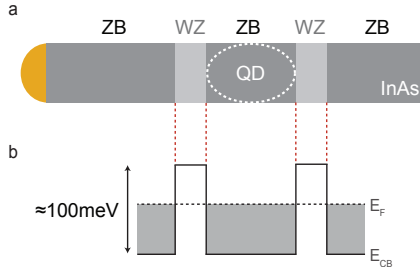


**Figure 4.2. Schematic of crystal phase defined QD in NW. a** Schematic of a InAs NW with a built-in QD defined by WZ tunnel barriers (light grey) and ZB leads (dark grey). **b** Illustration of the energy diagram of the conduction band edge  $E_{CB}$  relative to the Fermi energy  $E_F$  [59, 136].

emission measurements  $\sim 135$  meV [141].

### SEM imaging of crystal phase defined quantum dots

As already mentioned, InAs NWs with crystal phase defined QDs have been used, which were grown by randomly distributed Au aerosol particles with a variation in diameter (2 nm to 3 nm). The difference in diameter not only directly affects the resulting diameter of the NW, but also the total length of the grown segments, due to a slower growth rate. This results in shorter segments for larger seed particles, which also depends on the crystal phase [137]. In addition, the random distribution of the particles on the substrate also affects the segment length. Areas where Au particles are located less dense on the surface, are effectively exposed to a higher concentration of precursor material, leading to an increase in growth rate. As a result, the size of the WZ barrier, the ZB QD and also the location of the QD varies within one growth batch.

However, it is required to know the location and also the dimension of the QD, in order to fabricate well defined devices. Unfortunately, it is not possible to detect the location of the WZ tunnel barriers (i.e. the QD) with standard standard scanning electron microscope (SEM) techniques, as only the crystallographic structure varies, not the material. However, it is still possible to observe the change in crystal structure, by using “electron channeling contrast imaging” (ECCI), an SEM technique, which is used to detect defects in crystalline materials [142, 143]. Here, we follow closely the approach of Refs. [25, 59]. This method is based on the interaction of the electrons incident from the beam of the SEM and the crystal lattice of the material. A standing electron density wave is formed, after the electrons entered the sample. Depending on the relative orientation of the impinging electron beam and the crystal lattice, the amount of backscattered electrons varies. An increase of the amount of backscattered electrons is observed when the maxima of the

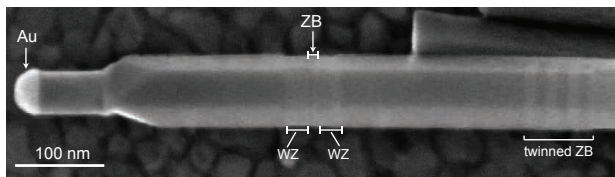


**Figure 4.3. InAs NW with WZ tunnel barriers.** ECCI SEM image under an angle of  $5^\circ$ . The ZB segment, defining the QD, is seen between two WZ segments. SEM image taken with the help of E. Bieler (Nano Imaging Lab, SNI).

electron-density wave match the position of the atomic-sites. This enables us to distinguish between the ZB and the WZ segments of the NWs, because they have different atomic orientations and will therefore give a different contrast in the ECCI signal. Consequently, we can estimate the geometrical dimension of the QD and also its location.

The drawback of this method is that it is very time consuming and is preferable done after electrical measurements, because the NWs could be damaged after being exposed with the electron beam for a long time. In our case, we performed the measurements together with the help of E. Bieler from the Nano Imaging Lab of the Swiss Nanoscience Institute. In Fig. 4.3 an SEM image done by ECCI can be seen. One can clearly see the gold particle on top of the NW as well as the WZ segments (bright) enclosing a ZB segment. In addition, we observe several shorter variations in contrast within the long ZB segment, towards the right of Fig. 4.3. We can attribute this, to rotational twinning of the ZB crystal segments itself, which means the atomic layer is rotated by  $60^\circ$  around the growth direction [135].

By using this method, we can measure the thickness of the WZ barriers and the size of the QD of individual nanowires. Within one growth batch the size of the QD varies from 20 nm to 25 nm and the thickness of the WZ barriers 30 nm to 35 nm. Based on statistics of ECCI SEM images, we are also able to give an estimation of the location of the QD, before device fabrication, based on the diameter and total length of the NWs, within an error of  $\pm 50$  nm. We note, that it is possible to gain control on reproducibility of the desired dimensions by using pre-defined arrays of seed particles [59].

### 4.3. Characterization of crystal phase defined quantum dots in InAs nanowires

The next section will characterize the QDs which are mainly used in this thesis. Before we can perform measurements, we need to fabricate functional devices using standard electron beam lithography, described in chapter 3. All measurements have been performed at a temperature of about  $\sim 20$  mK.

#### Dependence of the life-time broadening on the gate voltage

In Fig. 4.4 we present the measured  $dI/dV$  with respect to  $V_{BG}$  at zero source drain voltage  $V_{SD}$ . We observe regular CB resonances over a large backgate voltage range  $V_{BG} \approx -1$  V to 7 V. Already here, we can notice that not only the height, but especially the FWHM of the CB resonances increases with increasing gate voltage. In order to quantify this, we fit each resonance assuming a Lorentzian shape in the limit of  $kT \ll \Gamma$  (see equation 2.4 in Sec. 2.1.1) and extract the resonance broadening  $\Gamma$ . In Fig. 4.5 we plot the extracted res-

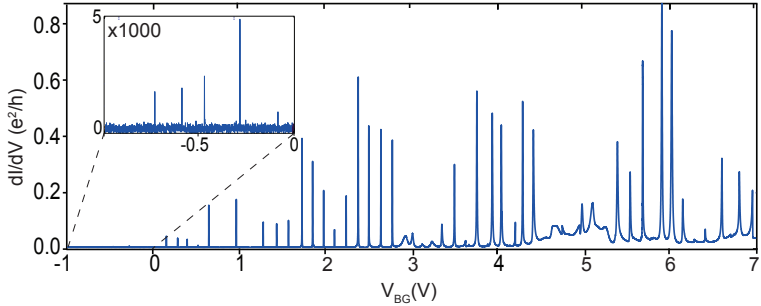


**Figure 4.4. Coulomb resonances of crystal phase defined QD.** Differential conductance  $dI/dV$  with respect to the applied backgate voltage  $V_{BG}$  [136]. © 2019 by SpringerNature.

onance broadening  $\Gamma$  with respect to the applied  $V_{BG}$ . We observe a clear systematic increase of the average broadening  $\Gamma$  with increasing  $V_{BG}$ , with a strong variation between neighbouring charge states, possibly due to orbital effects. At low gate voltages ( $V_{BG} \approx 0$  V), the resonance broadening is  $\approx 50$   $\mu$ eV and increases up to  $\approx 1$  meV at large gate voltages ( $V_{BG} \approx 7$  V). This is consistent with an exponential increase with a linear reduction of the barrier height with respect to  $E_F$ .

Following the analysis of Ref. [144], we can qualitatively fit our data by assuming the simple case of an electron between two square shaped tunnel barriers (see inset of Fig. 4.5). We assume the barriers to be sharp defined, the bias voltage to be small and the same conduction band edge  $E_{CB}$  alignment in all nanowire segments. Therefore the remaining free parameters in our model are: the barrier thickness  $a$ , the distance between the barriers  $s$ , the barrier height  $V_0$ , the pinch-off voltage ( $E_{CB} = 0$ ) and the gate lever arm. Based on the previously described SEM techniques (section 4.2), we can estimate the WZ barrier thickness to be  $a = 30$  nm and the distance between the barriers  $s = 20$  nm (i.e. the QD). We further know the height of the barriers  $V_0 \approx 100$  meV from previous measurements [25]. Based on our experience from previous nanowire measurements, we know that the pinch-off voltage can strongly differ for individual nanowire devices. This might be, due to differences in the fabrication process (like the contacting method) or individual charging effects during the cool down of the samples.

The tunnel probability through one of the barriers is well described by the

transmission coefficient  $T_{L/R}$  for left/right barrier respectively [74]:

$$T_{L/R}(E) = \left( 1 + \frac{V_0^2 \sinh^2(ka)}{4E(V_0 - E)} \right)^{-1}; k = \sqrt{2m^*(V_0 - E)/\hbar^2}. \quad (4.1)$$

We can then describe the lifetime broadening  $\Gamma$  by:

$$\Gamma = \frac{\hbar v_F}{2s} (T_L + T_R), \quad (4.2)$$

where  $v_F/2s$  is the attempt frequency, in this semi-classical model, and  $v_F$  the Fermi velocity. Using this expression, allows us to fit the extracted data (red line in Fig. 4.5). Here, the bottom of the conduction band edge  $E_{CB}$  (pinch - off voltage) is  $V_P = -9$  V, which is unknown for this specific device. Furthermore, the lever arm, converting energy to the respective gate voltage is set to 0.5%, which is 10 times smaller than what we extracted from the QD measurements ( $\approx 5\%$ ). One possible reason for the large discrepancy between the experimental and the model lever arm, could be the fact that the extracted lever arm is the one of the QD, which is not necessarily the same for the leads. However, this is qualitatively in agreement with the lead segments being much longer, compared to the quantum dot. In the model, we further assumed a

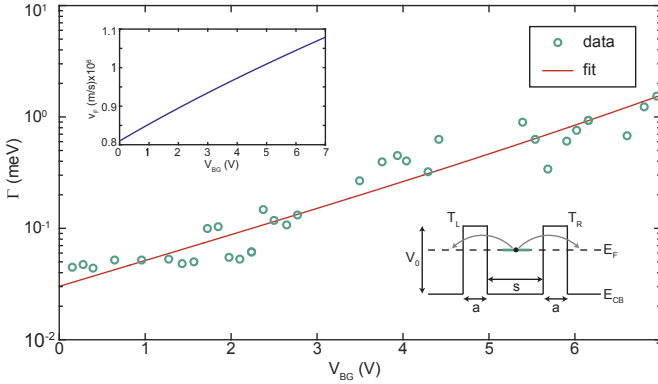


**Figure 4.5. Backgate dependence of QD broadening.** Logarithmic plot of QD resonance width  $\Gamma$  as a function of  $V_{BG}$  (green circles). Resulting fit with square shaped potential barriers. Inset on the right shows schematic of considered model, consisting of two square shaped tunnel barriers, illustrating the conduction band off-set due to the WZ segments in the ZB NW. Inset on upper left shows the Fermi velocity  $v_F$  as a function of gate voltage  $V_{BG}$ .

constant density of states in the leads of  $D_N = 1$ , which might not be the case in the experiment. In addition, the Fermi velocity  $v_F$  varies from  $v_F = 0.8 \times 10^6$  m/s to  $1.1 \times 10^6$  m/s, as the inset shows.

We further note, that our data spans only one order of magnitude, which is not ideal for an exponentially dependent fit.

However, we conclude that we can qualitatively fit our data very well, by using a very simple model. This allows us to give an estimate on the resulting QD, based on the growth size of the WZ and ZB segments, which is not possible for gate-defined QDs. A more detailed study of broadening mechanisms of tunnel barrier defined QDs can be found in Ref. [144].

### Coulomb blockade diamonds

In Fig. 4.6 we present CB diamond measurements<sup>1</sup>:  $dI/dV$  is measured with respect to the bias voltage  $V_{SD}$  as well as backgate voltage  $V_{BG}$ . We observe a very regular Coulomb blockade pattern from which we can extract the addition energy  $E_{add} \approx 10$  meV and charging energy  $E_C \approx 7$  meV. The energy level spacing is estimated to be  $\sim 1$  meV to 3 meV. Within the presented gate range, the resonance broadening of the CB resonances is estimated to be  $\approx 50$   $\mu$ eV. Outside of the Coulomb blockade region, we observe positive conductance lines perpendicular to the CB diamond edges, which we attribute to excited states of the QD (one excited state is indicated with a white arrow). As described in section 2.1.2, transport is still sequential in this regime, but takes place with the ground or excited state of the QD<sup>2</sup>.

In addition, we observe positive and negative conductance lines outside the CB diamonds. These resonances result from tunnel coupling fluctuations between the QD states and the one-dimensional subband states in the semiconducting NW lead segments between the QD and the metallic contacts. When tuning the backgate voltage  $V_{BG}$  the coupling between those states and the QD states varies, resulting in an increase or decrease of conductance. Similar signatures have already been observed in such QD systems before [59].

The important conclusion from this measurement is, that the crystal phase defined QDs are electrically very well defined and behave as expected. We can describe the detected dependence of the life-time broadening with respect to the applied gate voltage with a very simple model. This enables us to predict the QD, based on its growth size. Furthermore, we can access a wide range of coupling strengths, as  $\Gamma$  can be tuned from  $\sim 50$   $\mu$ eV up to a few meV. This is especially interesting, when working with aluminum as a superconducting electrode for example, as the superconducting energy gap is  $\Delta_{Al,bulk} \approx 220$   $\mu$ eV. In addition, we detect a large energy level spacing of  $\delta E \approx 1$  meV to 3 meV

<sup>1</sup>of a similar device of the same nanowire growth batch.

<sup>2</sup>For a detailed study of the excited state spectrum of crystal phase defined QDs, we refer to Ref. [59].



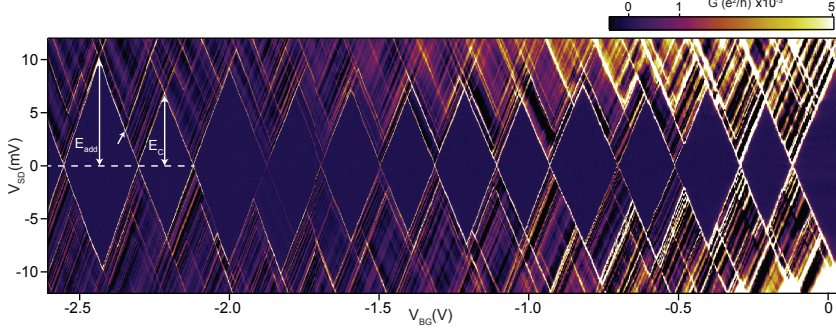


**Figure 4.6. Coulomb blockade diamonds of crystal phase defined QD.** Differential conductance  $dI/dV$  ( $G$ ), with respect to the voltages  $V_{SD}$  and  $V_{BG}$  at a temperature of  $T = 20$  mK. Addition energy  $E_{add}$ , charging energy  $E_C$  and excited state (white arrow) as indicated.

and charging energies of  $E_C \approx 7$  meV. This means, the QD levels are well separated from each other and can be very sharp, compared to the sample to be probed. These characteristics allows us to use crystal phase defined QD as a proper tunnel spectrometer for the DOS in the adjacent NW lead segments.



# 5 Spectroscopy of the superconducting proximity effect in InAs nanowires using built-in quantum dots <sup>1</sup>

---

In the following chapter, we introduce a new material platform that allows us to perform ideal tunnel spectroscopy, by using a tunnel barrier defined (“integrated”) quantum dot in an InAs nanowire. This allows us, to probe the superconducting proximity region of a nanowire segment close to the superconducting contact. The QD is formed with two tunnel barriers, defined by alternating the crystal phases, as described earlier in section (section 4.1) [23, 58]. As discussed earlier, the QD is both electrically and spatially well defined, which allows us ultimately to investigate the induced superconducting proximity gap inside the NW. Furthermore, this system enables us to predict the coupling strength, based on a similar analysis as outlined in Ref. [144]. Here, we use such artificial QDs to study the evolution of the proximity induced superconductivity in a controlled and systematic manner. We demonstrate this type of spectroscopy using two different transport regimes of the QD: the cotunneling regime and the resonant tunneling regime. In the cotunneling regime, we can picture the quantum dot as one single barrier, while in the resonant tunneling regime, the QD is essentially an energy filter. The results of both measurement regimes enable us to provide an intuitive description of the formation of the induced superconducting gap in a bare InAs NW lead segment. In addition, we discuss results based on numerical calculations, which support our interpretation quantitatively. The numerical calculations were done in collaboration with Denis Chevallier.

## 5.1. Sample and characterization

Here, a NW made of InAs is used, in which the QD is already integrated during the NW growth process [58] by alternating its crystal phases. The segments made of WZ crystal phase ( $\sim 30$  nm thickness) create tunnel barriers in the ZB nanowire as their bandstructure aligns with a conduction band offset of  $\sim 100$  meV [25, 141]. This results in the formation of a well defined quantum dot

---

<sup>1</sup>Parts of this chapter are published similarly in Ref. [136]. All figures and text are reused with permission by © 2019 SpringerNature.

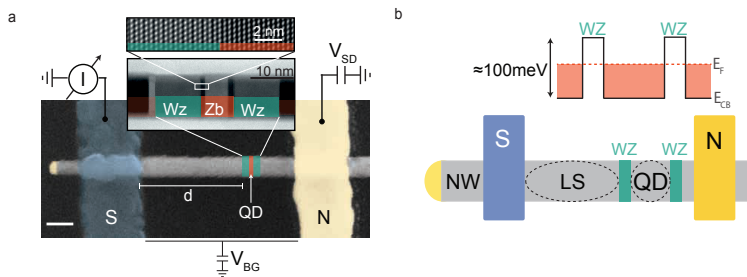


**Figure 5.1. Crystal phase engineered QD in an S - QD - N sample.** **a** SEM picture of examined sample, made of a superconductor S (blue) - InAs NW - normal metal N (yellow) (scale bar: 100 nm). The QD is created by two built in tunnel barriers (green), made of WZ crystal phase. We illustrate the measurement geometry as a scheme. A TEM image of an ZB/WZ interface within the InAs NW is shown as an inset. **b** Illustration of an NW S - N device structure with a schematic of the energy diagram of the conduction band  $E_{CB}$  relative to the Fermi energy  $E_F$  [136]. © 2019 by SpringerNature.

in the ZB segment ( $\sim 20$  nm to 30 nm) [25]. A SEM picture of the investigated sample is presented in Fig. 5.1a. In addition, we show a TEM image of the sharp interface between both crystal phases. We use standard E-beam lithography, in order to evaporate one contact made of aluminum and the second one made of gold. By measuring the differential conductance  $G = dI/dV$  with respect to  $V_{BG}$ , we detect very regular CB resonances in the normal state, meaning we applied a magnetic field of  $B = 50$  mT in order to quench superconductivity (see Fig. 4.4 and Fig. 4.5 in section 4.3). Here, we detect a broadening of the resonances when going from low to high backgate voltages. The observed exponential behaviour is in agreement with the lowering of the effective tunnel barrier when the bandstructure is tuned to lower energies as a function of the Fermi energy (see schematic in Fig. 5.1 b) [25]. For further investigation of this effect, see Ref. [144].

For the investigated sample, the location of the QD is about  $L \approx 350$  nm to the superconducting contact. This leaves a bare InAs NW segment with this length between the quantum dot and the superconductor. In the following, we will call this segment the “lead segment” (LS) of the NW (see Fig. 5.1). One has to realize, that this gives a fundamentally new experimental situation: we are convinced, that the quantum dot is *not* connected directly to the superconducting reservoir, which is likely the situation in previously studied systems [39, 97, 117]). This situation allows us to investigate the NW LS. We note, that the backgate voltage  $V_{BG}$  changes the electrochemical potential of

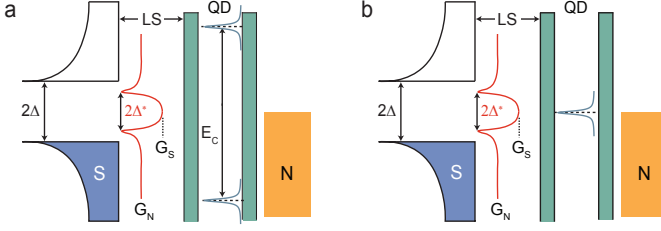


**Figure 5.2. Energy diagram of S - LS - QD - N system.** Schematic illustration of energy diagrams of the investigated system, for two different transport regimes: cotunneling regime **a** and resonant tunneling regime **b**. The induced superconducting gap  $\Delta^*$  in the lead segment of the NW is shown in red [136]. © 2019 by SpringerNature.

the LS as well as the QD simultaneously. In the following, we will investigate the  $G$  with respect to  $V_{SD}$  between the superconductor and the normal metal. In case, the electron tunnels from the QD to the SC directly, it is expected to observe the superconducting bulk gap of aluminum  $\Delta \approx 210 \mu\text{eV}$  [147], which does not depend on the applied  $V_{BG}$ . Assuming that the bias mainly drops on the QD, we expect the measured  $G \propto \text{DOS}$  in the LS. As a consequence, we are convinced, that we are performing ideal tunneling spectroscopy on the LS of the NW, using the quantum dot as a spectrometer (see Fig. 5.2).

Fig. 5.3 a-c presents CB diamond measurements of the device in the superconducting state for three different regimes of  $V_{BG}$ . The characteristics of the quantum dot are found to be: charging energy  $E_c \approx 6 \text{ meV}$ , level spacing  $\epsilon \approx 1.5 \text{ meV}$  to  $2 \text{ meV}$ , consistent with previous results of this platform. Already on this scale, we detect a peculiar transition, as for large  $V_{BG} \gtrsim 3 \text{ V}$  there seems to be an induced gap around zero bias (c.f. Fig. 5.3 c), which is not the case for low values of  $V_{BG}$  (c.f. Fig. 5.3 a). In the intermediate regime, shown in Fig. 5.3 b, it is not clear if we detect a superconducting gap, as the measurement resolution is not good enough on this scale. However, at low gate voltages (Fig. 5.3 a), we detect a regular sequence of CB diamonds, without signatures of induced superconductivity.

In the following part, we will demonstrate that we can use the quantum dot as a spectrometer in both regimes: the cotunneling regime, as well as in the resonant tunneling regime. When we are in the cotunneling regime [148], the number of charges on the quantum dot is fixed, as  $\Delta^* \ll E_c$ . For this regime, we can picture the quantum dot as a single tunnel barrier. In the resonant tunneling regime, the electrochemical potential of the QD is aligned with the one of source and drain.

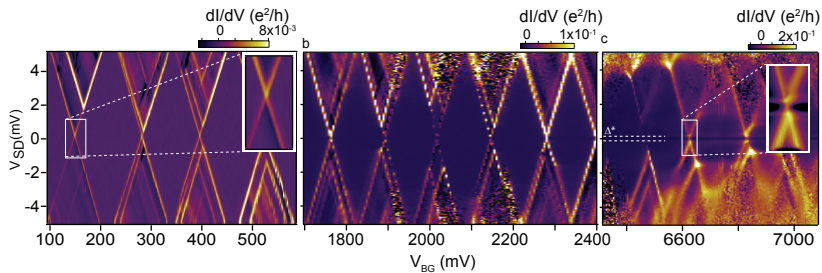


**Figure 5.3. Crystal phase engineered QD in an S - QD - N device.**  $G$  with respect to  $V_{BG}$  and  $V_{SD}$  in the superconducting state. We show a zoom-in of the respective resonance in the insets. Diamond measurements in the low gate voltage regime **a** and intermediate regime **b**, showing regular diamonds. **c** CB diamonds at higher backgate voltages revealing an energy gap around zero bias [136]. © 2019 by SpringerNature.

## 5.2. Proximity gap in cotunneling regime

We will now focus on the investigation of the cotunneling regime. Here, we interpret the SC - LS structure as an S-N junction with weak coupling to the quantum dot. The data of the spectrum is shown in Fig. 5.4 a. We can now characterize four quantities: the observed induced gap  $\Delta^*$ , the broadening (FWHM) of the peaks at energy  $\Delta^*$ , the conductance  $G_N$  in the normal state, which is measured at a bias  $|V_{SD}| > \Delta^*/e$  and  $G_S$  the conductance at  $V_{SD} = 0$ . In addition, we quantify the suppression of the conductance at low bias using a suppression factor  $S = G_S/G_N$ , as it is not completely suppressed, i.e. the gap which we observe is “soft”.

In Figs. 5.4 a-c we show the measured  $G$  with respect to  $V_{BG}$  and  $V_{SD}$  for three different backgate regimes. The cross sections of several different values of  $V_{BG}$  are depicted as blue lines within Figs. 5.4 a-c.

For high gate voltages ( $V_{BG} \approx 7$  V, c.f. Fig. 5.4 a) a clear proximity induced superconducting gap  $\Delta^*$  is observed around  $V_{BG} \approx 0$ . We are able to detect this gap to a gate voltage of about  $V_{BG} \approx 2.6$  V (shown in Fig. 5.4 b).

In Fig. 5.5 a we plot a selection of cross sections which are normalised to  $G_N$  for several different values of  $V_{BG}$ . Every cross section shows a conductance suppression of  $G$  at around zero bias. The induced superconducting energy stays constant for this gate range and is found to be  $\Delta^* \approx 150$   $\mu$ eV. Furthermore, we can extract the broadening of the peaks at energies  $\approx \Delta^*$ , as well as the suppression factor  $S$  from this plot. In Fig. 5.5 b, we plot the extracted values of these characteristic quantities as a function of the applied backgate

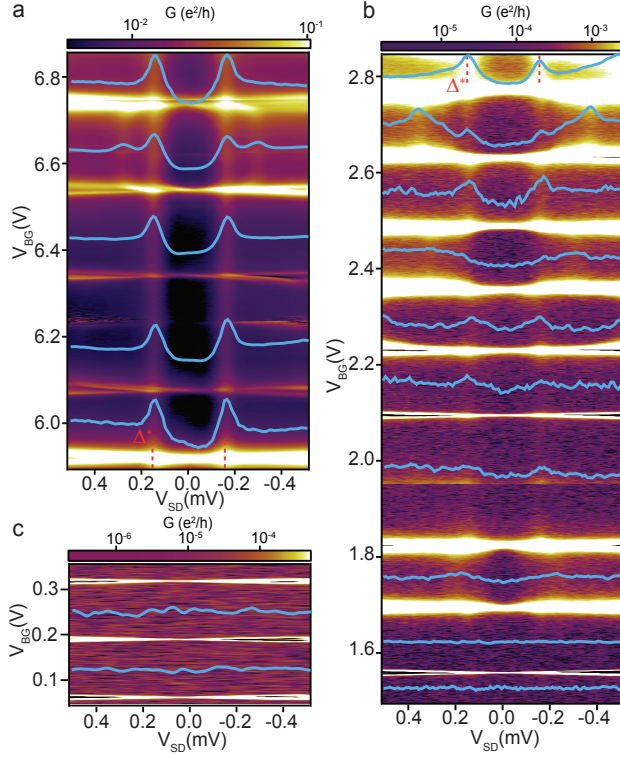


**Figure 5.4. Proximity gap detected in cotunneling spectroscopy.** Differential conductance  $G$  with respect to  $V_{BG}$  and  $V_{SD}$  for **a** high, **b** middle and **c** low  $V_{BG}$ . The blue lines represent cross sections, which were taken in the blockade regime of the quantum dot [136]. © 2019 by SpringerNature.

voltage  $V_{BG}$ . We find that both, the FWHM as well as the suppression factor  $S$ , are almost constant in this gate regime. We estimate the  $FWHM$  to be  $\approx 65 \mu\text{eV} \pm 10 \mu\text{eV}$  and the suppression factor  $S \approx 0.5 \pm 0.1$ .

For a perfect superconducting contact in the weak coupling regime, the suppression factor  $S$  is supposed to be zero in the limit of a tunnel barrier. However, higher values are very often detected in the case of induced superconducting gaps, which we refer to “soft gaps” [3, 149, 150].

In the gate regime, where  $V_{BG} < 2.6 \text{ V}$  (Fig. 5.4 b) the detected cotunneling signal is very weak, which is why we are unable to do the same quantitative

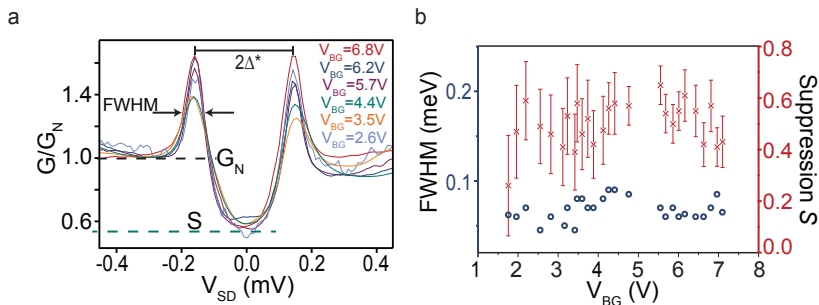


**Figure 5.5. Normalized proximity induced superconducting energy gap.** **a**  $G$  normalised to  $G_N$  with respect to  $V_{SD}$  at constant backgate voltages for the cotunneling regime. **b** Full Width Half maximum (blue) of the coherence peaks and normalized zero bias suppression  $S$  (red) as a function  $V_{BG}$  [136]. © 2019 by SpringerNature.

analysis. Despite this fact, we are still able to detect broad peaks down to a backgate voltage of  $V_{BG} \approx 1.8$  V. Once, the applied backgate voltage is  $V_{BG} < 1.8$  V the detected  $G$  is too small to detect a signature of the induced gap, within the measurement resolution of our setup. When gate voltages are applied smaller than  $V_{BG} \approx 0.2$  V (Fig. 5.4 c), we can not resolve any signatures within the blockaded region of the quantum dot any more. To summarize: within the regimes, where we are able to extract an induced gap in the cotunneling regime, the gap does not depend on the applied backgate voltage  $V_{BG}$ .

### 5.3. Proximity gap in sequential tunneling regime

In the next part of this chapter, we will examine the regime, where the level of the QD is on resonance, i.e. the sequential tunneling regime. Here, we are able to investigate a bigger gate range, as compared to the cotunneling regime. The left figure (“Exp.”) of each panel in Fig. 5.6 a-d shows zoom-in measurements CB resonances at different  $V_{BG}$  voltages. The central panel shows a calculated map which is discussed below, whereas the panels to the right present cross sections at gate voltages  $V_{BG}$  as indicated in the left and central panels.

For an ideal SC - QD - N device we expect the CB diamond pattern to be strongly modified compared to the standard N - QD - N configuration, as shown in Fig. 5.6 e. First, we expect the CB diamond tips to be shifted apart by  $2\Delta^*/e$  in bias (energy). Secondly, we also expect the diamond tips to be also shifted in gate voltage by a value of  $\Delta V_{BG} = 2\Delta^*/\beta e$ . Here,  $\beta$  is the gate



lever arm of the quantum dot. For further discussion, see section 2.3.1 as well as Refs. [97, 151].

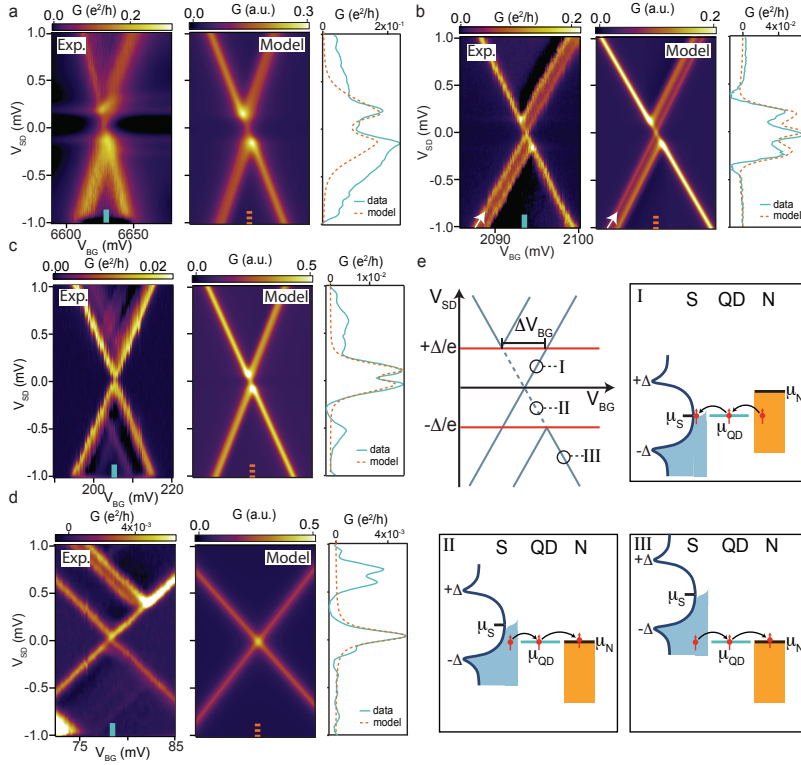


**Figure 5.6. Proximity gap detected in sequential tunneling.** **a-d** Experiment (left) and resonant tunneling model (middle) as well as cross sections of both (right) for a selection of CB resonances. Light blue and orange lines represent the backgate voltage of the cross sections. **e** Positions of the electrochemical potentials of the normal electrode ( $\mu_N$ ), the SC ( $\mu_S = \mu_N - eV_{SD}$ ) and the QD ( $\mu_{QD}$ ) for selected points. The tips of the diamonds are shifted in  $V_{BG}$  by:  $\Delta V_{BG} = 2\Delta^*/(\beta e)$ , where  $\beta$  is the lever arm of the CB resonance. In **a** the tunnel coupling is roughly 3 times as large as in **b-d**. In the model,  $\Gamma$  is effectively the same for **b-d**, while the value of the induced gap  $\Delta^*$  changes from  $\Delta^* = 165$   $\mu$ eV in **a**,  $\Delta^* = 145$   $\mu$ eV in **b**,  $\Delta^* = 85$   $\mu$ eV in **c** and  $\Delta^* < 10$   $\mu$ eV in **d** [136]. © 2019 by SpringerNature.

By analysing the characteristic quantities of the quantum dot in the normal state (compare Fig.4.5), we find that the coupling strength  $\Gamma$  is increased for gate voltages  $V_{BG} > 2.5$  V. In the regime, where  $\Gamma$  is high, at  $V_{BG} \approx 6.6$  V for example, the CB diamond is presented in Fig. 5.6 a. Here, the resonance of the CB diamond is very broad. However, we can detect a suppression of the  $G$  around  $V_{SD} \approx 0$ . Furthermore, we observe an induced superconducting proximity gap of  $\Delta^* \approx 150 \mu\text{eV}$ , which is consistent with what we found earlier in the cotunneling regime (Fig. 5.4).

In Fig. 5.6 b we present a CB resonance, where the coupling strength  $\Gamma$  is reduced, compared to the resonance of Fig. 5.6 a, for a backgate value of  $V_{BG} \approx 2.1$  V. Here, we observe an additional resonance, which we will explain below. In addition, we see a shift of the diamond tips of  $\pm \Delta^*/e$  in bias and by  $\Delta V_{BG}$  in gate voltage, consistent with what we expected (see Fig. 5.6 e). Both yields a value of the induced gap of about  $\Delta^* \sim 150 \mu\text{eV}$ . As already mentioned, we detect one additional resonance which crosses the gap (indicated with white arrows). This additional resonance corresponds to the situation, when the Fermi level of the two reservoirs is aligned with the level of the quantum dot. Consequently, we interpret this as tunneling via the non-zero DOS which remains around  $V_{BG} \approx 0$ , due to the softness of the gap (see position I in Fig. 5.6 e).

For a gate value of  $V_{BG} \approx 0.2$  V we observe, that the suppression of  $G$  is reduced, presented in Fig. 5.6 c. We further notice, that the tip of the CB diamond is only slightly separated and also only slightly shifted in gate. As already mentioned, we are not able to resolve any signal for this gate value in the cotunneling regime, as seen in Fig. 5.4.

For gate values of  $V_{BG} \approx 80$  mV (Fig. 5.6 d), it is impossible to detect a modification of the CB resonance, caused by the superconductor. We rather observe the well known CB resonance pattern, which we found in the normal state of the device.

In order to examine the characteristic quantities using the presented data of the sequential tunneling regime, we can use a standard resonant tunneling model based on the assumption of an S - QD - N structure. We can then calculate the expected current to be [95, 97]:

$$I = \int_{-\infty}^{\infty} dE D_N(E) \cdot D_S(E + eV_{SD}) \cdot T_{QD}(E, V_{BG}, V_{SD}) \cdot [f_N(E) - f_S(E + eV_{SD})]. \quad (5.1)$$

In this equation,  $D_N(E)$  is the DOS of the normal metal, while  $T_{QD}(E, V_{BG}, V_{SD})$  is the Lorentzian transmission function of the quantum dot, which accounts for the resonant tunneling of electrons trough the QD. Furthermore,  $f_{S/N}$  are the Fermi functions of the normal and the superconducting electrodes respectively. In order to take into account the observed “soft gap”, we can use the phenomenological Dynes parameter  $\delta$  [152], which

then gives us the following description of the DOS of the proximitized LS:

$$D_S = \left| \Re \left( E - i\delta / \sqrt{(E - i\delta)^2 - \Delta^{*2}} \right) \right|. \quad (5.2)$$

We can now model the  $G$  maps presented in Figs. 5.6a-d (“model”), by adjusting the amplitude of the induced superconducting proximity gap  $\Delta^*$ , the coupling strength of the quantum dot  $\Gamma$  as well as the Dynes parameter  $\delta$ .

With a coupling strength  $\Gamma = 150 \mu\text{eV}$ , we can reproduce the resonance of Fig. 5.6 a very well. Here, we get  $\Delta^*$  to be  $\Delta^* \approx 165 \mu\text{eV}$ , and  $\delta = 0.4 \cdot \Delta^*$  ( $\delta = 65 \mu\text{eV}$ ). This results in a suppression factor of  $S \approx 0.5$ , which is consistent with the value extracted in the cotunneling regime.

In order to model the resonance, which is shown in Fig. 5.6 b we find  $\Gamma = 40 \mu\text{eV}$ ,  $\Delta^* \approx 145 \mu\text{eV}$  and  $\delta = 0.4 \cdot \Delta^*$  ( $\delta \approx 60 \mu\text{eV}$ ). This means, that the parameters of the model are almost the same, as the ones found in the cotunneling regime at larger  $V_{BG}$ . Furthermore, the resulting cross section of the model is also in good agreement with the cross section of the experimental data. In addition, we see, that the enhanced conductance at the edge of the superconducting gap, as well as the negative differential conductance are also reproduced by the theoretical model. We note: in the sequential tunneling regime, we are able to detect and characteristics of the superconducting proximity gap, down to a value of  $0.2 \text{ V}$ , which was impossible in the cotunneling regime.

In the following part we will focus on the CB resonance presented in Fig. 5.6 c ( $V_{BG} \approx 200 \text{ mV}$ ). Here, the coupling strength is almost the same as the one of the resonance in Fig. 5.6 b ( $\Gamma = 60 \mu\text{eV}$ ), and  $\delta = 0.5 \cdot \Delta^*$  ( $\delta \approx 40 \mu\text{eV}$ ). In contrast, the proximity induced superconducting energy gap is reduced to  $\Delta^* \approx 85 \mu\text{eV}$ , which is smaller than what we extracted at higher  $V_{BG}$ . The cross sections confirm, that the model is able to reproduce the experimental data with good agreement.

When trying to reproduce the CB resonance, which is shown in Fig. 5.6 d, at a backgate value of about  $V_{BG} \approx 80 \text{ mV}$ , we find an upper limit for  $\Delta^*$  of  $10 \mu\text{eV}$  and a coupling strength of about  $\Gamma = 50 \mu\text{eV}$ .

We find, that the presented experimental data is very well modelled with the presented parameters and effectively corresponds to a regular N - QD - N device. We further note, that the resonance in the data at larger bias voltage outside of the CB region, is due to an excited state, which is not taken into account in our model.

We can summarise the presented data of the resonant tunneling regime in the following manner, i.e. Fig. 5.6: we detect a transition from a regime where the LS acts as a superconducting lead (at high  $V_{BG}$ ) with a constant gap of  $\Delta^* \approx 165 \mu\text{eV}$  to  $150 \mu\text{eV}$  down to a regime where the induced gap is smaller  $\Delta^* \approx 85 \mu\text{eV}$ , to a regime where superconductivity has no effect at all anymore. We therefore conclude, that our data demonstrates a clear evolution

of the induced proximity gap  $\Delta^*$  of the LS with respect to the applied gate voltage  $V_{BG}$ .

## 5.4. Discussion

In Fig. 5.7 a we present a summary of the experimental results of both discussed transport regimes. Here, we plot the extracted magnitude of the proximity induced gap  $\Delta^*$  in the NW LS with respect to the applied backgate voltage  $V_{BG}$ . We clearly observe a relatively abrupt transition from a resolved induced gap for  $V_{BG} > 0$  to a fully suppressed gap at  $V_{BG} < 0$ .

As discussed, we are able to fit the detected features with a broadened BCS DOS qualitatively. However, might not be the adequate description, since there is only a small number of states in the quasi 1D nanowire segment. Assuming only a few modes in the NW LS, we can give a clear picture of the process causing the observed transition of Fig. 5.7 a. Every electron with an energy smaller than  $\Delta^*$  will be Andreev reflected at the superconductor, which then gives rise ABSs.

### Qualitative understanding

We can understand the detected transition of  $\Delta^*$  qualitatively as a transition of the ABSs created in the LS, caused by the change in gate voltage. We essentially turn the system from the short junction limit into the long junction limit, as described in section 2.3.3). We can distinguish both limits, by comparing the actual length of the junction,  $L$ , to the critical length-scale  $L_c = \hbar v_F / \tilde{\Delta}$ , which is essentially the coherence length [153]. In this equation,  $v_F$  is the Fermi velocity in the NW LS,  $\hbar$  the Planck constant and  $\tilde{\Delta}$  the proximity induced superconducting gap in the NW below the superconducting contact, as shown schematically in the inset of Fig. 5.7 a. Considering the short junction limit, meaning  $L \ll L_c$ , the Andreev bound state energy in the LS is determined by the acquired phase, because of Andreev reflection at the interface of the superconductor and the LS. Here, we have to assume a sudden change of  $\tilde{\Delta}$ . For this situation, the Andreev bound states are “pushed” to the gap edge, meaning  $E_{ABS} \cong \tilde{\Delta}$ . Consequently, this results in the formation of a superconducting proximity gap LS which is of the magnitude of  $\tilde{\Delta}$ , i.e.  $\Delta^* \sim \tilde{\Delta}$  [104].

When moving on to the long junction limit of the junction,  $L \gg L_c$ ,  $E_{ABS}$  is now dominated by the change in phase in the LS. This scales with  $k_f = m^* \cdot v_F / \hbar \propto v_F$ , where  $m^*$  is the effective mass of the electrons. Here,  $E_{ABS}$  can have values which are smaller than  $\Delta^*$  and therefore start to fill the induced superconducting gap [153].

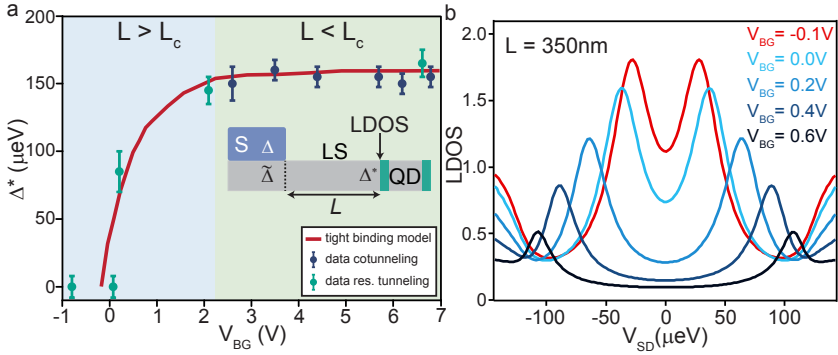


**Figure 5.7. Proximity induced gap as a function of gate voltage. a** Proximity induced superconducting energy gap  $\Delta^*$  with respect to  $V_{BG}$ . The inset shows schematically the considered sample geometry and the required parameters. **b** Numerical calculations of the local DOS with respect to a selection of gate voltages for a distance of  $L$  from the interface,  $L = 350$  nm [136]. © 2019 by SpringerNature.

Consequently, we realize that we can also modify the  $E_{ABS}$  by tuning  $v_F$  as well as the electron density in the LS by changing the backgate voltage  $V_{BG}$ . In our data, we see that for very high gate voltages, the Fermi energy  $E_F$  is far up in the conduction band and thus the Fermi velocity  $v_F$  is also large. This results in an effectively long  $L_c$ , which drives the LS into the short junction limit, as  $L < L_c$ .

In the other limit, meaning the Fermi energy  $E_F$  is tuned to the bottom of the conduction, the Fermi velocity  $v_F$  is lowered and therefore also  $L_c$  is smaller. This is the situation for lower values of the backgate voltage  $V_{BG}$  and brings the LS into the long junction limit, meaning  $L > L_c$ , and the energy of the Andreev bound states  $E_{ABS} < \tilde{\Delta}$ . Consequently, the induced gap that appears  $\Delta^*$  is reduced, because of the ABSs which move to smaller energies inside the gap. Note, that the NW segment below the superconducting electrode is not tuned by the backgate voltage, as it is screened by the superconductor.

## Numerical calculations

In order to support this interpretation, we examine a numerical model, that combines the Green's function method with a tight binding model. We account for the properties of the superconductor as a self energy dressing the bare Green's function in a NW section below the superconductor, in which

the gap  $\tilde{\Delta}$  is induced, which depends on the coupling strength to the superconductor. In the supplementary of Ref. [136], we present more details of the performed calculation, which was done by Denis Chevallier. This segment is directly connected to a bare InAs NW segment (of length  $L = 350$  nm) which models the LS, as presented in the inset of Fig. 5.7 a. We now look at the local density of states (LDOS) for a distance of  $L = 350$  nm as a function of the applied gate voltage  $V_{BG}$ . The results are shown in Fig. 5.7 b for a few selected values of  $V_{BG}$ , indicated by different colours. Similar to the measured data, the magnitude of the induced gap  $\Delta^*$  is extracted from the model, as the distance between the peaks of the DOS. As described before, the energy of the Andreev bound states, as well as the number of bound states, is a consequence of the physical length of the LS. We plot the extracted values of  $\Delta^*$  of the numerical calculation with respect to the applied backgate voltage  $V_{BG}$  in Fig. 5.7 a (red solid line). Similar to the measured data, we see a transition of the extracted induced gap size, which corresponds to the transition from the short to the long junction limit. Within the model, the induced gap  $\Delta^*$  goes to zero in case the Fermi energy  $E_F$  is tuned to the bottom of the conduction band ( $V_{BG} \approx -0.2$  V. This is right before the NW LS is completely depleted and the Fermi velocity is  $v_F \rightarrow 0$ . In the appendix, in Fig. B.1 a, we plot the behaviour of a single Andreev bound state with respect to the applied gate voltage, for a fixed length  $L$ . In addition, we present cross sections for different lengths  $L$  for a fix value of the backgate voltage  $V_{BG}$  (see Fig. B.1 b).

As already mentioned, we do observe a “soft” gap in our spectroscopy measurements, meaning the suppression of  $G$  around zero bias is lower than in NWs with an epitaxial aluminium shell [26, 131]. The origin of this softness is not clear and is also not expected from our model. As a reference, we measured evaporated bulk Al in a standard large area metallic S - I - S tunnel junction configuration which shows a “hard gap” in a similar measurement setup (see Fig. B.3 in the appendix). In addition, we tried to reproduce the softness of the proximity gap, by adding random spatial potential fluctuations at the nanowire - superconductor interface [154, 155] in the presented numerical model, which also could not account for the detected soft gap either (presented in Fig. B.2 in the appendix).

Within the framework of Andreev bound states, the broadening of the Andreev bound states in the LS depends on their lifetime, which results in a softening of the measured induced gap. This broadening can originate from different mechanisms: tunneling to the quantum dot (which should have a similar tunability as the life time of the quantum dot), single particle tunneling to the nanowire segment below the superconductor (due to the inverse proximity effect caused by the gold nanoparticle at the top of the nanowire), as well as quasiparticle excitations, due to absorption of microwave radiation which might differ in semiconducting nanowire samples in comparison to metallic junctions.

## Conclusion

In conclusion, our work demonstrates a systematic study of the superconducting proximity gap in a bare InAs nanowire segment, originating from the close by superconducting electrode. The basis of our measurements is controlled tunnel spectroscopy performed by an integrated quantum dot, which is formed by built-in tunnel barriers. We detect a transition, which is tunable by the gate voltage, from a fully induced superconducting gap, at high gate voltages to a reduced gap size and ultimately a complete gap suppression at low gate voltages. Our measured data is in good agreement with the transition from the short to the long junction limit in a superconductor - normal configuration, where Andreev bound states have been formed at energies smaller than the induced gap. We observe this transition, in case the Fermi energy is aligned with the conduction band edge, where the Fermi velocity is consequently tending to zero. We furthermore present a new platform, nanowires with integrated tunnel barriers, which are in our case formed by an alternation of crystal phases, which can be extremely useful to perform unambiguous transport spectroscopy in superconductor-semiconductor hybrid devices in general. Therefore, we have presented a novel spectroscopy tool, well suited to investigate superconducting bound states in semiconducting nanowires, which can be used to battle fundamental limitations, which are found in the latest studies of Majorana bound states [33, 34].





# 6 Spectroscopy of superconducting sub-gap states in InAs nanowires<sup>1</sup>

---

In the following chapter we use InAs nanowires (NWs) in which the quantum dot (QD) is predefined by crystal phase engineering (see chapter 4). In this case the QD size is  $\approx 20$  nm (made of zinc-blende crystal phase) whereas the tunnel barriers, defined by wurtzite segments are  $\approx 30$  nm. As already discussed in chapter 5, the usage of a built-in QD provides a new experimental situation: instead of being directly coupled to metallic reservoirs, the QD is coupled to a bare nanowire segment, forming nanowire leads (see Fig. 6.1 (a)). In chapter 5, we used this setup to investigate the gate dependence of the proximity induced gap in a NW with one superconducting contact and a metallic one [136]. In contrast to the previous chapter, we now use the integrated QD as a spectrometer to resolve individual sub-gap states in the adjacent NW lead segment. Complex features appear spontaneously in the proximitized nanowire at low magnetic field, involving the Kondo effect competing with the Coulomb interactions and the superconducting proximity effect to form superconducting sub-gap states.

## 6.1. Device and characterization

The nanowires are contacted by one superconducting contact made of evaporated titanium/aluminium (Fig. 6.1. (a) and (b)) and one contact made of titanium/gold. The spacing between the metallic contacts is  $L = 400$  nm and the total size of the barrier defined QD is roughly 70 nm, such that the QD is connected to the reservoirs by bare nanowire segments. The contacts are designed such that the spacing between the superconductor and the first tunnel barrier  $\sim 250$  nm, yielding a NW segment between the gold contact and the QD much smaller than the one between the aluminium and the QD. The chemical potential of the whole sample (the QD and nanowire segments) can be tuned using an electrostatic backgate ( $V_{BG}$ ). An additional side gate ( $V_{SG}$ ) is placed in the vicinity of the wire to allow a finer tuning. The sample is cooled down using a dilution fridge with a base temperature of 50 mK and its

---

<sup>1</sup>Parts of this chapter are accepted for publication in a similar form in *Physical Review Letters* and are available as a pre-print in in Ref. [156]. All figures and text are reused with permission by © 2020 American Physical Society.

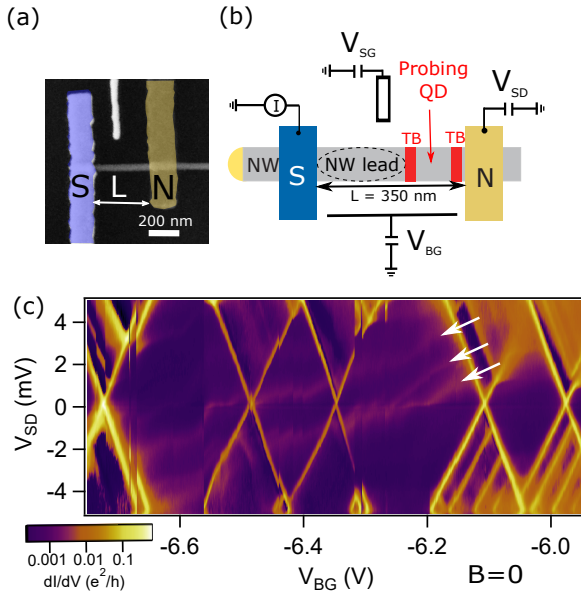


**Figure 6.1. Device and characterization.** (a) Scanning electron microscope image of the sample, and (b) associated schematics. A nanowire, in which two tunnel barriers (TB) have been grown in situ, is contacted with one SC and one N electrode. The electrostatic potential can be tuned using a backgate  $V_{BG}$  and a side gate  $V_{SG}$ . (c) Differential conductance with respect to  $V_{BG}$  and  $V_{SD}$ . Inside of the CB diamonds, one can see a gate dependent conductance background which looks independent from the barrier defined QD (indicated by white arrows). Note the logarithmic scale of the colour-code [156]. © 2020 by American Physical Society.

differential conductance  $dI/dV_{SD}$  is measured using a standard low frequency lock-in technique.

The Coulomb blockade (CB) diamond measurement of the sample is presented in Fig. 6.1. (b). We observe clearly-defined diamonds over a large gate voltage range that correspond to the QD with a charging energy of to  $E_c \approx 5$  meV and inter-level spacing  $\delta E \approx 1$  meV. Inside of the CB region, the conductance is not homogeneous: broad conductance lines extend over three consecutive diamonds. These conductance lines are not excited states of the QD, which would give rise as well to parallel lines outside of the diamonds, like the excited states that can be seen very clearly between  $V_{BG} = -6.2$  and  $V_{BG} = -5.9$  V for negative  $V_{SD}$ . These features are independent from the QD, since they

can be tuned independently by a side gate (see appendix C) or undergo charge rearrangements that do not affect the QD (Fig. 6.1. (c)). Note that the lever arm of the side gate is very small, such that we cannot use it to efficiently tune one chemical potential independently of the others. In the following, we set the side gate to  $V_{SG} = 0$ .

## 6.2. Spectroscopy of superconducting sub-gap states

To understand the features inside the Coulomb blockade region, we focus now on small bias voltages of the order of the superconducting gap of aluminium ( $\Delta \approx 200 \mu\text{eV}$ ). This is what is presented in Fig. 6.2, in both normal and superconducting states.

Inside the Coulomb diamonds of the integrated QD, the current is carried by second order cotunneling processes (Sec. 2.1.2) such that the transmission of the QD is strongly reduced [85]. Consequently, the bias voltage drops mainly over the QD, which can thus be considered as a tunnel barrier [30]. As a consequence,  $G \propto \text{DOS}$  in the NW segment. In that respect, the barrier-defined QD can be seen as a probe of the NW segment, which is why we refer to this QD as the “probing QD”. In the normal state, around zero bias, most of the broad conductance lines remain at zero bias over a gate range around 25 mV. This is a characteristic feature of the Kondo effect as observed in a QD occupied by an odd number of electrons [87, 157]. The associated Coulomb diamonds are smeared out, asymmetric in  $V_{SD}$  and have a small signal (see dashed blue lines on Fig. 6.2. (a)). The charging energy is evaluated to be  $\approx 0.5 \text{ meV}$ , indicating a large QD (typically ten times larger than the probing QD, *i.e.*  $\sim 500 \text{ nm}$ ). These characteristics suggest that a large QD forms in a nanowire segment, which is strongly coupled to one metallic reservoir (the closer one) and very weakly coupled to the other reservoir, which is separated by the tunnel barriers from the probing QD.

The nanowire lead QD is coupled in series with the probing QD, as the resistance of the tunnel barriers are very high, such that the voltage bias drops mainly on the probing QD. This is why we measure a combination of the DOS of the QD in the NW lead and the Coulomb diamonds of the probing QD.

The superconducting state data, presented on Fig. 6.2. (b) supports this picture. The cotunnelling regime reveals the opening of a gap with peaks at  $\Delta^* = 150 \mu\text{eV}$  (inset of Fig. 6.2. (b)), consistent with the value of superconducting gaps induced by evaporated aluminium (with a bulk gap  $\Delta \approx 220 \mu\text{eV}$ ) in semi-conducting nanowires in literature [3, 131, 150, 158]. This gap is the one induced by the superconducting proximity effect in the nanowire segment located between the probing QD and the superconducting contact. Note that the current is not fully suppressed at zero bias, suggesting a soft gap, simi-

lar to previous experiments using evaporated aluminium to contact the InAs nanowire [13, 131, 136]. The fact that the features observed in the normal states are strongly modified in the superconducting state also proves that they originate from the NW segment located between the superconducting contact and the probing QD.

Each region (A-D) of Fig. 6.2. (a) gives rise to characteristic sub-gap states consistent with bound-states due to a localized impurity coupled to a superconducting reservoir (see Fig. 6.2. (b)). In general, we can categorize two different types of sub-gap states in such systems, namely Andreev Bound states (ABS) and Yu - Shiba - Rusinov (YSR) states. The ABSs are formed by the transfer of Cooper pairs via Andreev reflection at interfaces [90, 117, 123, 159] (see section 2.3.4). In contrast, the YSR states are formed by the coupling between a magnetic impurity and a quasiparticle in the superconductor [124, 150, 160, 161]. Both processes can be described as a competition between the Kondo screening of the impurity by the reservoir that favours a singlet state and the Coulomb interaction that favours a doublet state [114, 115, 162–164].

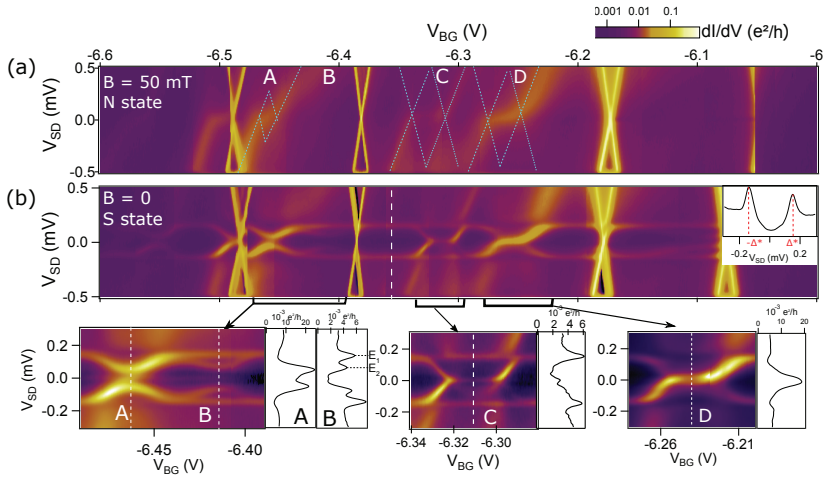


**Figure 6.2. Spectroscopy of sub-gap states in nanowire lead segment.** Differential conductance as a function of  $V_{BG}$  and  $V_{SD}$ , focusing on small  $V_{SD}$ , both in normal (a) and superconducting states (b). Note the logarithmic scale of the color code. The figure has been corrected from some rearrangements. Light-blue dashed lines indicate CB diamonds of the QD in the lead segment in (a). Bottom panel: detailed measurements of indicated regions called A, B, C and D [156]. © 2020 by American Physical Society.

Detailed measurements of the sub-gap states in this system are presented in the bottom panel of Fig. 6.2. Due to instabilities in gate voltage, we corrected the data presented in this figure. We note, that no gate jumps occurred in the regions which are of relevance for the interpretation of the data.

In the following we study four sub-gap states in more detail labelled as A, B, C and D in Fig. 6.2. (b). In the normal state (Fig. 6.2. (a)), we detect Kondo resonances for A, C and D. In contrast, we can not detect any conductance features for region B in the normal state.

In region A (Fig. 6.2, bottom left), we observe sub-gap states at energies below the superconducting gap, which do not cross zero energy. In the cross section we further see, that there is no resonance peak remaining at the gap edge.

Similar to this region, the sub-gap states in region B we detect one resonance at the gap edge  $E_1 = \pm\Delta^*$  and a second resonance at energies  $E_2$  which detaches from the gap edge but does not cross zero bias. In addition, the cross section reveals an additional resonance with low amplitude at zero bias.

The sub-gap states of region C show qualitatively different characteristics, as they cross at zero energy and form a loop structure with an additional peak along zero bias. We further do not detect resonance peaks along the gap edge in the cross section.

In region D, the sub-gap states detach from the gap edge and form a peak at zero bias. The cross section further reveals no resonance peak along the gap edge. The detected characteristics of the sub-gap resonances in regions A, C and D are consistent with the ABS picture [90, 117, 123, 159]. Even though the sub-gap resonance in region B forms a similar half-loop as region A, it is not consistent with the ABS framework, as there is no conductance feature in the normal state.

In order to quantify the observed sub-gap states, we perform magnetic field dependent measurements in the following section. In general, we can characterize the type of sub-gap states by comparing the relevant energy scales, namely the Kondo temperature  $T_K$  (see Eq. 2.5) and the superconducting gap  $\Delta$ .

For  $k_B T_K \ll \Delta$  the system is in a doublet state. In a QD system, for an odd number of occupation, the system undergoes a singlet to doublet transition, which manifests in a crossing of the bound-states at zero.

When  $k_B T_K \gg \Delta$ , the system goes from a BCS-type singlet to a Kondo-type singlet. When the number of electrons is odd, the bound-states separate from the gap but do not cross zero, since there is no singlet-doublet transition.

### 6.3. Magnetic field dependence

For low magnetic fields, regions A, C, D show the expected magnetic field dependence, as shown in Fig. 6.3. These resonances scale with the energy gap  $\Delta$  and vanish at the critical magnetic field  $B_C$  (see waterfall plots in Fig. 6.3). This characteristic behaviour is also found for the resonance at energy  $E_1$  in region B. However, the resonance which forms the loop in region B at  $E_2$  does not depend on the applied magnetic field but stays at constant energies for  $B < B_C$ .

For higher magnetic fields, we detect the broadening of the zero bias peak (Kondo peak) in region A (Fig. 6.3. A), which broadens up to  $B = 0.6$  T and vanishes for even higher values. From the width of the peak, we can estimate  $k_B T_K \approx 150$   $\mu$ eV. We attribute this to the very weak signal, associated with a high Kondo temperature (and thus a very broad peak), such that the splitting is not visible. The sub-gap state in region A reveals bound states which hold very similar characteristics to those expected from a spin 1/2 state coupled to a superconducting reservoir in the limit  $T_K \gg \Delta$  described above.

According to the magnetic field dependence of the conductance, presented on the panel C of Fig. 6.3, the Kondo peak is already split at  $B = 50$  mT. This means,  $k_B T_K < 25$   $\mu$ eV  $< \Delta$  with an extracted g-factor of  $g \approx 13.5 \pm 2$ , resulting from the Zeeman splitting of the peak at higher magnetic fields. This supports our interpretation that we are in the limit of  $T_K \ll \Delta$ . We note that we do not expect the observed (small) zero bias peak at zero field. However, we speculate that it is a weak Kondo peak that forms due to the presence of quasiparticles in the soft gap [124].

Region D presents the intermediate regime  $k_B T_K \approx \Delta$ , resulting in the crossing of the bound-states over the entire Kondo ridge. By investigating the FWHM of the peak in the normal state, we estimate  $k_B T_K \approx 110$   $\mu$ eV (Fig. 6.3. D). This order of magnitude is confirmed by the magnetic field evolution of the Kondo peak: it splits for  $B > B_c \approx 0.3T \approx k_B T_K / (g\mu_B)$  [165].

In magnetic field, the Kondo peak is expected to split, resulting in a Zeeman shift of

$$\Delta E = 2 \times m_s |g| \mu_B B_Z, \quad (6.1)$$

with  $B_Z$  the Zeeman field,  $m_s$  the spin number and  $|g|$  the absolute value of the landé factor (Sec. 2.1.2).

From this we can conclude, that the bound-states observed in region C and D are consistent with a splitting of the Kondo peak a spin  $m_s = 1/2$  and a g-factor  $|g| = 12 \pm 2$ . The obtained value is also consistent with reported g-factors in InAs NWs [89, 166]. We further note, that this is not the g-factor of the built-in QD, but from the one in the nanowire lead, which is why its value is close to  $|g| = 15$ , as found in bulk InAs or in large dots [167]. The sub-gap states in regions C and D are therefore in good qualitative agreement with the presence of a spin 1/2 state located in the NW lead segment (as presented on

Fig. 6.4. (a)).

However, the magnetic field dependence of the sub-gap state in region B reveals a more complex situation. At higher magnetic field, several conductance peaks appear. These peaks arise at voltage bias larger than the charging energy and are thus probably excited states involving two resonances, which are shifted by the Zeeman field. We detect one resonance with an energy that is almost constant with magnetic field, i.e. the slope is  $\sim$  zero. A second resonance occurs with the same slope as detected in regions C and D. In addition, we find a resonance which has twice the slope. This suggests the presence of two spin 1/2 energy levels, that form either a singlet ( $S = 0, m_s = 0$ ) or a triplet state ( $S = 1, m_s = 0, m_s = \pm 1$ ). Considering the value of the g-factor measured above  $|g| \approx 13$  for the Kondo resonances, one of these peaks cor-

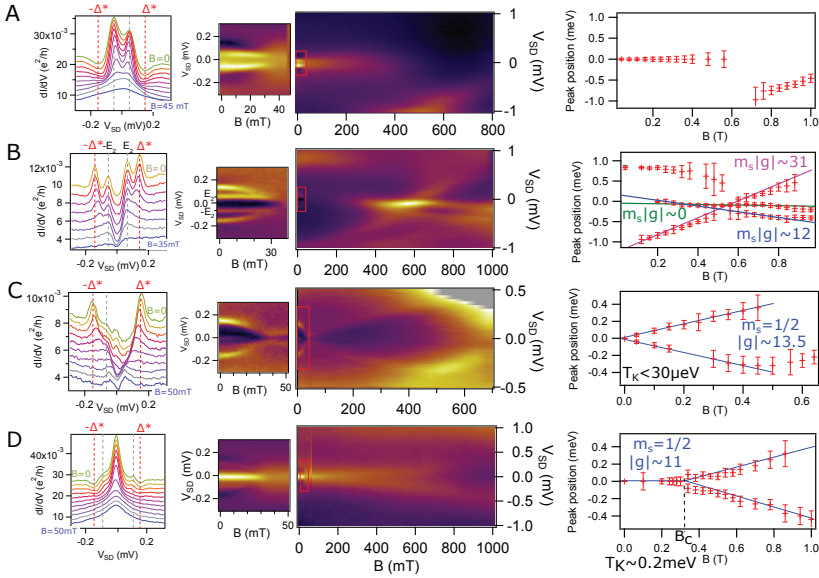


**Figure 6.3. Magnetic field dependence.** Discrete sub-gap states with respect to external  $B$  field for the four regions defined in Fig. 6.2. (b). The magnetic field is applied out of plane. For each region, the left panel shows a focus on small magnetic field, below the critical field of the aluminium induced gap ( $B_c \approx 35$  mT), emphasizing the field evolution of the proximity induced gap and of the bound-states. The right panels show the evolution of the conductance for larger  $B$  fields. The evolution of the peak positions is shown on the very right [156]. © 2020 by American Physical Society.

responds to  $m_s = 0$ , which is constant as a function of magnetic field. The triplet  $|m_s = 1|$  occurs with twice the slope compared to the single spin  $1/2$  level (Fig. 6.3. B).

While most A, C, D of these sub-gap states can be at least qualitatively understood by the standard picture of ABS or YSR states, we found two (and discuss one) type of resonances that does not follow these pictures. To at least tentatively explain these states we propose an anomalous shell filling in the (confined) lead segment with a  $s = 1$  filling. These states might form superconducting bound states when coupled to the superconductor, with rather different dependence on an external magnetic field, an anomalously large Zeeman shift (two times) and a normal state Kondo effect rather different from the  $s = 1/2$  states. Alternatively, the coupling of a  $s = 1/2$  state to S might also result in more than one superconducting bound state forming below  $\Delta$ , and a possibly rather different field dependence.

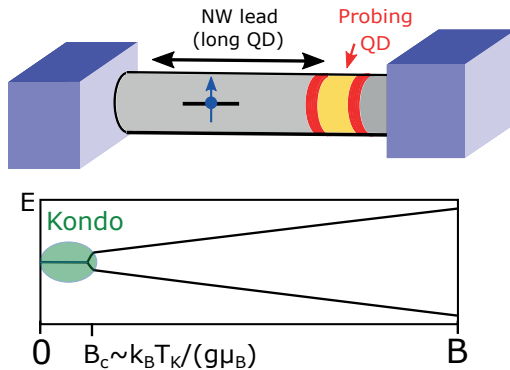


**Figure 6.4. Schematic of considered system and qualitative magnetic field dependence.** The regions C and D of Fig. 6.3 are compatible with the existence of a single impurity (blue arrow) in the nanowire lead. The magnetic field evolution of the associated energy level shows a splitting of a Kondo peak, once the Kondo singlet is broken (for  $B_C > k_B T_K / (g \mu_B)$ ).

## 6.4. Conclusions

In this chapter, we performed tunnel spectroscopy on a nanowire lead segment, in presence of a Kondo impurity. When superconducting correlations are induced in this segment, the lead segment obtains sub-gap eigenstates, some of them being consistent with Andreev bound states expected when a spin  $1/2$  state is coupled to a superconducting reservoir. Surprisingly, one (or two) of



these sub-gap states exhibit a rather different characteristics, not consistent with the standard ABS picture, possibly related to an unconventional shell filling and corresponding sub-gap states.



# 7 Hybridization of quantum dot and Andreev bound states

---

In the following, chapter we discuss measurements based on nanowire devices with two superconducting contacts. We present different transport regimes, in which we can explore various physical effects, such as Josephson (super) current and the hybridization of the quantum dot states with Andreev bound states.

The devices presented in the following sections consist of InAs NWs with a crystal-phase engineered quantum dot (QD) contacted by aluminum electrodes. The devices exhibit a variety of transport regimes accessed by different gate voltages. We begin with the regime at large positive gate voltages, where the NW acts as a Josephson “weak link” between the two superconductors and the QD has no significant influence on transport (Sec. 2.4.1). Afterwards, we discuss briefly the opposite regime, where the Fermi energy in the NW lead segment is aligned with the conduction band edge and transport is dominated by the QD (Sec. 2.4.2). In the intermediate regime, transport is governed by a combination of Andreev bound states and QD states, resulting in new hybridised states.

## Device and setup

In Fig. 7.1 a scanning electron micrograph of a representative device in a superconductor ( $S_1$ ) - QD - superconductor ( $S_2$ ) configuration is shown. The QD in the InAs NW grown in ZB crystal phase is defined by two tunnel barriers grown in WZ crystal phase (thickness:  $\sim 30$  nm). The QD in the enclosed ZB segment is electrically and spatially well defined with a size of  $\sim 20$  nm. Similar to the experiment performed in chapter 5, this allows us to probe the density of states (DOS) in the NW segments surrounding the QD. The total length of the junction is  $\approx 450$  nm and the QD is located closer to one of the superconducting contacts  $S_1$  ( $L_1 \sim 50$  nm) than to the other superconducting contact  $S_2$  ( $L_2 \sim 320$  nm). The superconducting contacts consist of evaporated titanium/aluminium (Ti/Al: 5 nm/80 nm) and the devices are measured in a two terminal configuration, as shown in Fig. 7.1. A voltage  $V_{BG}$  is applied to the bottom of the wafer, therefore it acts as a global backgate tuning both the

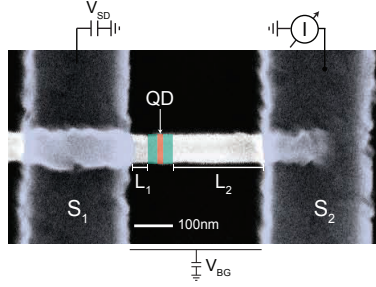


**Figure 7.1. Device and setup.** SEM image of a similar sample. The device consists of an InAs NW, which inherits an integrated crystal phase defined QD and two contacts made of aluminium  $S_{1/2}$ . The distance between  $S_{1/2}$  and the QD is indicated with  $L_{1/2}$ , whereas  $L_1 < L_2$ .

QD and NW lead segments. The lead segments  $LS_1$  and  $LS_2$  are the portion of the NW between the contact  $S_{1/2}$  and the QD. We stress again that  $LS_2$  is significantly longer than  $LS_1$ :  $L_1 \sim 50 \text{ nm} < L_2 \sim 320 \text{ nm}$ .

### 7.1. Supercurrent in open regime

First, we discuss the regime where the Fermi energy lies well in the conduction band due to the large electron density at positive backgate voltages  $V_{BG} \approx 11 \text{ V}$  to  $16 \text{ V}$ . In this gate regime, we do not observe any influence of charging effects of the QD and the system acts as a S - NW - S junction.

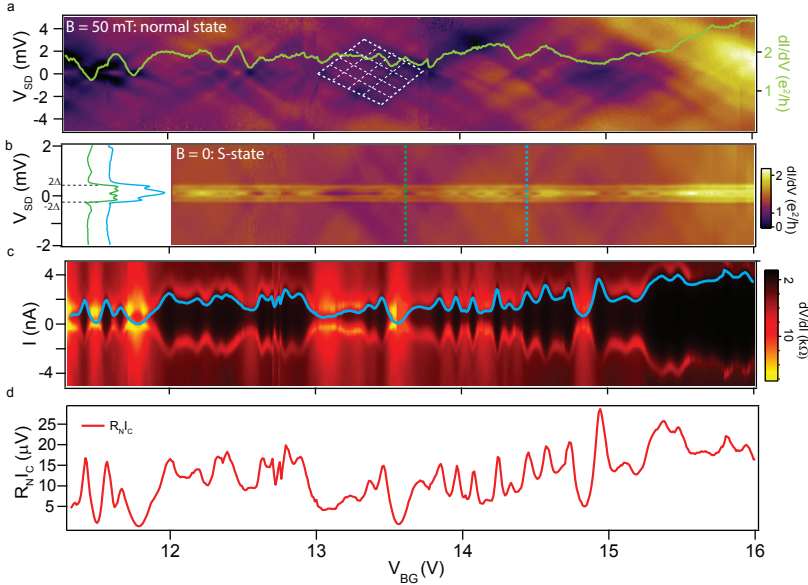
#### Normal state - Fabry-Pérot resonances

Fig. 7.2 a presents a  $dI/dV$  measurement with respect to  $V_{BG}$  and the applied voltage  $V_{SD}$  in the normal state (applied external perpendicular magnetic field  $B_{ext} = 50 \text{ mT}$ ). A clear chessboard-like pattern due to Fabry-Pérot resonances is observed. This demonstrates that the contacts are reasonably transparent and transport is likely to be ballistic in this gate range. Furthermore, we can distinguish between different Fabry-Pérot subpatterns, indicated as dashed white lines in Fig. 7.2 a. Similar multiple interference patterns have been observed in semiconducting nanowires and have been attributed to multiple subbands with different Fermi velocities, resulting in multiple sets of oscillations [168, 169]. This raises the question: where is the Fabry-Pérot cavity formed? By following the approach of Ref. [168], we estimate the length of the cavity  $L_{FP} = 2e/(C_g \Delta V_{FP})$ , where  $C_g$  is the gate capacity per unit length

and  $\Delta V_{FP}$  the respective oscillation period in gate [170]. For this device, we extract a cavity length of  $L_{FP1} \approx 50$  nm. This suggests that the cavity is formed in  $LS_1$ , which is of similar length  $L_1 \approx 50$  nm. This leads to the conclusion that the cavity is not formed between the WZ barriers (i.e. the QD), but in one of the lead segments  $LS_{1,2}$ .

### Superconducting state - supercurrent

We now turn our attention to the superconducting state of the electrodes for the same gate region, presented in Fig. 7.2 b. Here, we observe an enhancement of conductance for  $|V_{SD}| < 320 \mu\text{eV}$ , which we associate with multiple Andreev reflections (MAR) [171, 172]. We can observe MAR peaks up to



**Figure 7.2. Fabry-Pérot and supercurrent in strong coupling regime.** Differential conductance  $dI/dV$  with respect to  $V_{BG}$  and  $V_{SD}$  in the normal **a** and superconducting **b** state showing Fabry-Pérot resonances. The green line shows  $dI/dV$  with respect to the gate voltage for  $V_{SD} = 0$ . **c** Detected  $R$  ( $dV/dI$ ) with respect to the applied back gate voltage  $V_{BG}$  of the same gate region as in **a, b** in the superconducting state. The blue line follows the critical current  $I_C$ . **d**  $I_C R_N$  product as a function of  $V_{BG}$ .

$n=3$ , where  $V_{SD} \sim 2\Delta/en$ . The suppression of higher order MAR in differential conductance can be attributed to inelastic processes in the junction [171]. Furthermore, we can extract the magnitude of the superconducting gap to be  $\Delta \approx 160 \mu\text{eV}$ , assuming that the induced gap of both aluminum contacts is the same.

In Fig. 7.2 c, we present differential resistance  $dV/dI$  measurements with respect to the current  $I$  and  $V_{BG}$ . We observe a gate tunable supercurrent, similar to what has been found before in semiconducting NWs [3], with a maximal critical current of  $I_C \approx 5 \text{ nA}$ . The blue line corresponds to the transitions from the superconducting to the dissipative state, revealing oscillations as function of  $V_{BG}$ . Theoretically, one can expect the product of the critical current and the normal state resistance  $I_C R_N$  in the short-junction limit to be of magnitude  $\pi\Delta/e \approx 470 \mu\text{V}$  [103]. However, in our measurements, we find much smaller values of  $I_C R_N \approx 5 \mu\text{V}$  to  $25 \mu\text{V}$  (see Fig. 7.2 d), which has been observed before and attributed to a switching caused by thermal activation in Josephson junctions [3, 169, 173]. The oscillations of the  $R_N I_C$  product with respect to  $V_{BG}$  have been observed previously [174] and was attributed to the influence of the electromagnetic environment, which has a large impact for small supercurrents.

To summarize the measurement results of the open regime of this device, we observe Fabry-Pérot resonances in the normal state and a gate dependent supercurrent in the superconducting state, despite the presence of the built-in QD defined by two WZ barriers. This is likely due to the Fermi level lying above the height of the tunnel barriers  $E_F > 100 \text{ meV}$ . The detected critical current is small compared to the critical current measured in the same type of NWs ( $I_C \approx 5 \text{ nA}$  to  $20 \text{ nA}$ ), in NW segments made of ZB, without WZ tunnel barriers (see Fig.D.1 in appendix D). However, we find the  $I_C R_N$  product to be of similar magnitude  $I_C R_N \approx 8 \mu\text{V}$  to  $16 \mu\text{V}$  in the ZB segment. In the next section, we discuss measurements of the same device in the regime of low electron density.

## 7.2. Single electron characteristics in weak coupling regime

In this section, we present characterization measurements in the weak coupling regime  $\Gamma < \Delta$  (at low electron density) where transport is dominated by the QD. This enables us to characterize the QD, which we use as an electronic spectrometer in the next section.

For the remaining part of this chapter we consider the system in the configuration, which is schematically shown in Fig. 7.3 a. Here,  $\Delta_{1/2}$  denotes the bulk superconducting gap,  $\tilde{\Delta}_{1/2}$  the induced superconducting gap in the NW segment directly below the electrode and  $\Delta_{1/2}^*$  the induced gap in the respective NW lead segments  $LS_{1/2}$ . In Fig. 7.3 b we show the corresponding energy

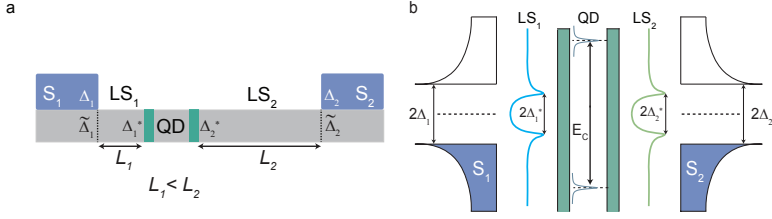


**Figure 7.3. Schematic of system and energy diagram.** **a** Schematic depiction of NW (grey) with two superconducting electrodes  $S_{1/2}$  and barrier (green) defined QD. The distance between the QD and the electrodes is  $L_{1/2}$ , dividing the NW in lead segment  $LS_1$  and  $LS_2$ . **b** Illustration of the energy diagram of the considered system, shown in **a**.

diagram for this type of system. We now turn to the gate region, where the QD is weakly coupled to the electrodes, meaning  $\Gamma < \Delta_{1/2}$ . The measured differential conductance as a function of  $V_{BG}$ , which is now close to  $V_{BG} \approx 0$  V, is presented in Fig. 7.4 (in the superconducting state of the electrodes). We find well defined CB diamonds, with a charging energy of  $E_C \approx 7$  meV and an energy level spacing of about  $\delta E \approx 0.5$  meV to 2 meV. For the resonance broadening  $\Gamma$  we extract  $\Gamma \approx 50$   $\mu$ eV for this gate range in the normal state (not shown). We note, that the two slopes (positive  $\beta_+$ , negative  $\beta_-$ ) of the CB resonances differ by a factor of three, suggesting a difference in the capacitive coupling to source and drain contacts. We detect a strong suppression of conductance within the Coulomb blockade regions and no cotunneling lines.

In Fig. 7.4 b we present a detailed measurement of the resonance marked by **A** in Fig. 7.4 a. We detect a shift of the Coulomb diamond tips in energy  $e\Delta V_{SD}$ , as well as in gate voltage  $\Delta V_{BG}$ . From both we can extract a shift in energy of  $\approx 150$   $\mu$ eV, consistent with the magnitude of *one* superconducting contact, with a gap of  $\Delta^* \approx 150$   $\mu$ eV (see chapter 5). This is contradictory to the fact that both contacts are superconducting. In the standard S-QD-S system, we expect a shift of the diamond tips in energy  $e\Delta V_{SD} = \pm 2\Delta$  and no shift in gate voltage  $\Delta V_{BG} = 0$ , as discussed in section 2.4.

We can interpret our observations as follows: in this gate region, only the shorter lead segment  $LS_1$  is fully proximitized by  $S_1$ , whereas the longer segment  $LS_2$  is not proximitized. This is consistent with results obtained in N - QD - S devices, where we detect a fully developed induced gap for large electron densities, whereas the gap vanished for very low electron densities. We explained this by a gate tunable transition from one limit to the other limit of the junction, as discussed in chapter 5. Similar to chapter 5, we interpret this as  $LS_2$  is in the long junction limit for such low electron densities, whereas  $LS_2$

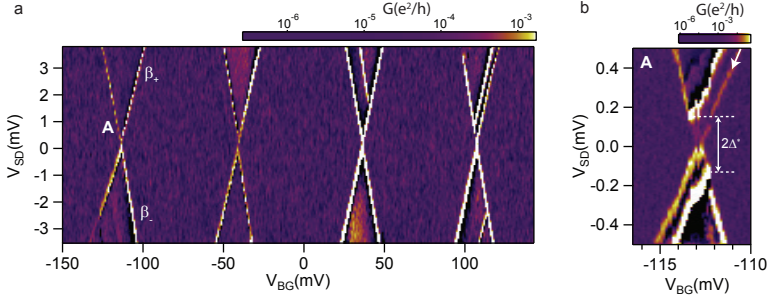


**Figure 7.4. CB diamonds in weak coupling regime.** **a** CB diamonds in superconducting state ( $B_{ext} = 0$ ), with charging energy  $E_C \approx 7$  meV and energy level spacing  $\delta E \approx 0.5$  meV to 2 meV. The CB resonance broadening is  $\Gamma \approx 50$   $\mu$ eV. **b** Detailed measurement of CB resonance labeled **A** in **a**.

is still in the short junction limit, which is reasonable for  $L_1 < L_2$ . This is why we observe only the induced gap  $\Delta_1^*$  originating from *one* superconducting contact  $S_1$  in  $LS_1$ , while  $LS_2$  behaves essentially as in the normal state.

Considering the results of the N-QD-S devices, we can further explain the additional resonance between the main CB resonances, crossing the induced gap (indicated by white arrow). Here, the Fermi level is aligned with both electrodes and the quantum dot level. Consequently, we can explain this by a remaining finite DOS around zero bias, which means that the induced gap is soft [43] (see also Fig. 5.6 in chapter 5). However, we can not provide proof of this interpretation, because we did not measure this resonance with sufficient resolution in the normal state. It is unlikely that the detected characteristics is due to an excited state, as  $\delta E \approx 0.5$  meV to 2 meV which is larger than the observed difference of 150  $\mu$ eV.

We conclude, that the system in this gate regime appears to be N-QD-S, possibly due to one NW segment ( $LS_2$ ) being close to depletion.

### 7.3. Intermediate coupling regime

The following section will present the gate regime for which the coupling strength  $\Gamma$  of the QD is similar to  $\Delta$ :  $\Gamma \sim \Delta_{1/2}$ , resulting in effects arising from both competing mechanisms, but no Josephson effect.

In Fig. 7.5 a,b we plot the measured  $G$  with respect to  $V_{SD}$  and  $V_{BG}$  (in the range of  $\approx 0.1$  V to 0.6 V). We observe CB diamonds, and a general increase in  $G$  with increasing  $V_{BG}$ , which we mainly attribute to larger electron densities in the NW lead segments. Especially outside of the CB diamonds we start



to see many additional resonances, only partially related to excited states of the QD. In addition, we detect resonances which have a different capacitive coupling compared to the QD, as they exhibit different dependence on  $V_{BG}$ . Therefore, we attribute these additional resonances to states in the NW lead segments  $LS_{1/2}$ . We note that it is not possible to detect effects originating from superconductivity on this large bias scale.

In Fig. 7.5 c,d we show measurements performed in the same gate range as in Fig. 7.5 a,b, but for smaller  $V_{SD}$ . In the following we use the integrated QD as an electronic spectrometer in two different transport regimes: First, we discuss the Coulomb blockade regime of these measurements, where the charge is fixed and transport is mediated by cotunneling through the QD (see section 2.1.2). Afterwards, we focus on the resonant tunneling regime.

### 7.3.1. Andreev bound state spectroscopy in cotunnelling regime

In the Coulomb blockade regime, we observe a few standard cotunnel resonances for energies  $|V_{SD}| \approx 0.5$  mV to 0.8 mV originating from excited states of the QD (marked with white arrows). At lower energies, we do not observe any cotunneling resonances. By increasing  $V_{BG}$ , we start to detect the induced superconducting gaps of the lead segments  $LS_{1/2}$ , see Fig. 7.5 d. The white lines correspond to cross sections taken at the respective gate voltage inside the Coulomb blockade region. We can clearly observe a peak-dip structure for  $V_{SD} \approx \pm 320$   $\mu$ eV corresponding to cotunneling arising from the induced gaps at  $eV_{SD} = \Delta_1^* + \Delta_2^*$ . Consequently, we can summarise, that we can not detect the induced gaps in the cotunneling (in the Coulomb blockade regime) for gate voltages  $V_{BG} < 470$  mV, i.e. for low electron densities. For higher gate voltages, the cotunneling signal increases and the induced gaps become visible, see cross sections in Fig. 7.5 d. In this gate region we detect the induced gaps of both superconductors, meaning both  $LS_{1/2}$  are in the short junction limit, holding the same value  $\Delta_{1/2}^* = \Delta^* \approx 160$   $\mu$ eV.

The peak-dip characteristic with negative differential conductance along the gap edge is well known for tunneling transport between two superconducting gap edges and originates from two peaks in the DOS [43, 123–125]. We can therefore conclude that we observe both induced gaps being fully evolved in the cotunneling regime starting from  $V_{BG} \approx 470$  mV.

The observed evolution of the induced gap in the cotunneling regime as a function of electron density is also consistent with the results obtained in the N - QD - S system (see chapter 5).

We start to see a strong influence of both induced superconducting gaps  $\Delta_{1/2}^*$  at the charge degeneracy points of the CB diamonds. Therefore, we now focus on the CB resonances labeled with **A-F** in Fig. 7.5 c,d.

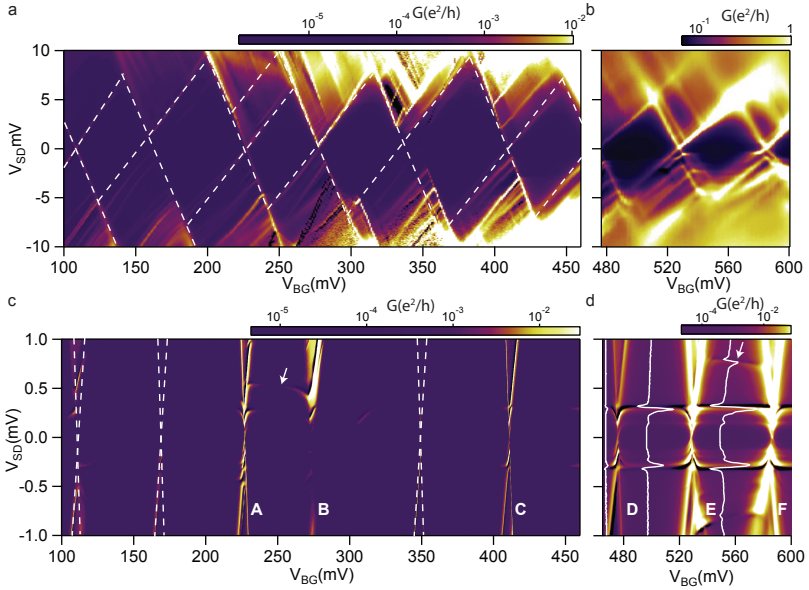


**Figure 7.5. CB diamonds in intermediate regime.** **a,b** Overview of intermediate regime **c,d** Zoom in of same gate range as in **a,b**. Insets in **d** show cross sections for respective gate region in CB. The CB resonance broadening for this gate region is  $\Gamma \approx 150 \mu\text{eV}$ .

### 7.3.2. Andreev bound state spectroscopy in sequential tunneling regime

Next, we turn our attention to detailed measurements of the charge degeneracy points of the QD, where transport is mediated mainly by first order sequential tunneling. In Fig. 7.6 a-c, we present measurements of the resonances labelled **A-C** in Fig. 7.5 c, whereas Fig. 7.6 e-g presents the resonances **D-F** of Fig. 7.5 d. In contrast to the cotunneling regime, we already observe an influence of both superconducting gaps from  $V_{BG} \approx 100 \text{ mV}$ .

CB resonances **A-C** revealing asymmetric anti-crossings of a QD resonance with a subgap resonance. or. The basic structure of the CB resonances in Fig. 7.6 a-c are very similar. One CB resonance (with negative slope  $\beta_-$ ) does not change direction and crosses almost linearly the superconducting gap. In contrast, the resonance with positive slope  $\beta_+$  does not cross the energy gap, bends away from its original direction, and aligns in horizontal direction at

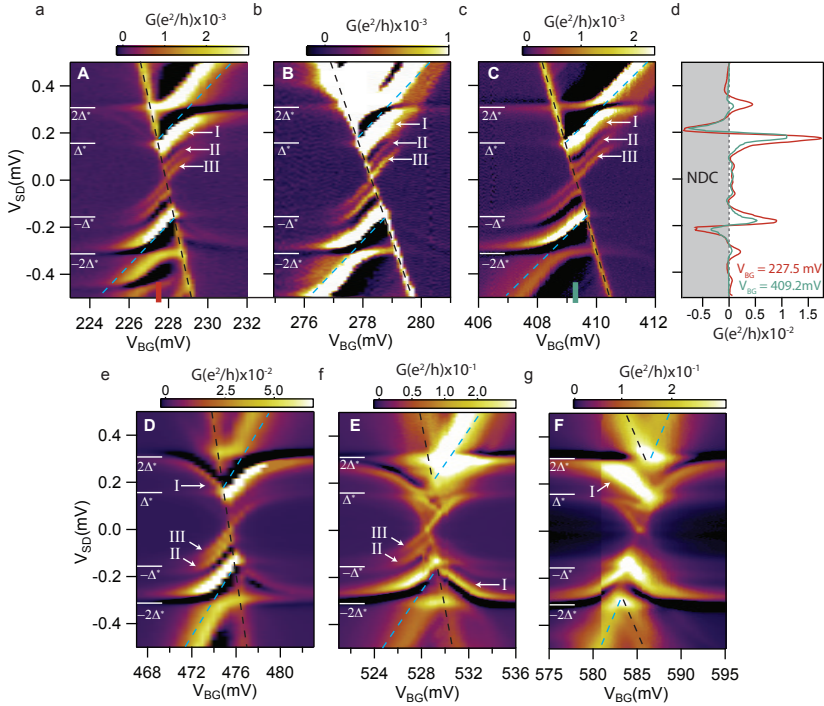


**Figure 7.6. Detailed measurements of Coulomb resonances.** a-c CB resonances **A-C** revealing asymmetric anti-crossing of CB resonance with subgap level (type *I*). Additional subgap resonances labelled with *II*, *III*. **d** Cross sections of resonance **A,C** at  $V_{BG}$  as indicated. **e-g** CB resonances **D-F** revealing anti-crossing in symmetric way (type *I*).

$\pm 2\Delta^*$ . In addition, this CB resonance is accompanied by NDC on the low-bias side (see Fig. 7.6 d), in contrast to the resonance with negative slope  $\beta_-$ . We find the Coulomb diamond tips to be shifted similarly to the weak coupling regime. This is unexpected, as it suggests a N - QD - S system. However, we also observe several subgap states up to  $|2\Delta^*|$  (vanishing in the normal state, not shown), suggesting a S - QD - S system.

For  $eV_{SD} < |2\Delta^*|$ , we observe three different types of resonances: one, occurs between  $|\Delta^*|$  and  $|2\Delta^*|$  (labeled by *I*) and another set of resonances at lower energies, labeled by *II* and *III*, respectively.

For the resonance of type *I* we can extract a full width at half maximum

(FWHM) of  $\approx 30 \mu\text{eV}$ . It originates from the CB resonance with negative slope at energies of  $eV_{SD} = \pm\Delta^*$ . This subgap resonance runs almost linearly towards higher energies and bends away from the Coulomb resonance (with slope  $\beta_+$ ) while approaching the gap edge at  $2\Delta^*$  horizontally. In addition, we observe NDC between this subgap resonance and the CB resonance. For the resonances **A-C** this anti-crossing appears to be, i.e. only with one CB resonance (with  $\beta_-$ ).

The type *II* and *III* resonances both have a smaller amplitude than type *I* (factor of 10 to 20 different) and a similar FWHM  $\approx 30 \mu\text{eV}$ . In addition, both occur at lower energies and run in parallel: type *II* originates where the CB resonance ( $\beta_-$ ) crosses energies of  $eV_{SD} \approx \pm 50 \mu\text{eV} \approx \pm\Delta^*/3$ . It runs linearly with  $V_{BG}$  towards higher energies, bends and vanishes at around  $|eV_{SD}| \approx 190 \mu\text{eV} > \Delta^* (< 2\Delta^*)$ . The energetic spacing between this type of resonance and type *III* is  $\approx 50 \mu\text{eV}$ .

The type *III* resonance has the unique characteristic that it crosses the charge degeneracy point at  $V_{SD} = 0$  (with the same slope as type *II*) and vanishes at energies of  $|\Delta^*|$ .

We can summarize the measurements of Fig. 7.6 a-c (i.e. gate region of  $V_{BG} \approx 200 \text{ mV}$  to  $400 \text{ mV}$ ) as follows: we observe shifted Coulomb diamond tips, suggesting a N-QD-S system. However, we also observe three different types of sub-gap states up to  $eV_{SD} = \pm 2\Delta^*$ , suggesting a S - QD - S system. Remarkably, one type of sub-gap level strongly anti-crosses with the QD level.

For slightly higher gate voltages, the CB resonances show different characteristics, shown in Fig. 7.6 e-g. First, the Coulomb tips are shifted less with respect to each other and do not cross the superconducting gap, which is what one would expect from a S - QD - S system. Secondly, the sub-gap states of type *I* are now bending in both directions and anti-cross with both Coulomb resonances at  $|2\Delta^*|$  in a more symmetric way. Furthermore, the type *II* resonances start to bend in both directions, especially in Fig. 7.6 f where they form a cross like structure.

We interpret the type *I* sub-gap resonance as a Andreev bound state (ABS) that formed within one lead segment. In contrast to previous samples, the ABS seems to be much stronger coupled to the QD, such that it starts to form a hybridized state in the energy window of  $\Delta^* < |eV_{SD}| < 2\Delta^*$ . In order to quantify the coupling strength we extract the energetic difference between the QD resonance and the ABS. The peak to peak distance yields values of  $60 \mu\text{eV}$  to  $150 \mu\text{eV}$  (see Fig. 7.7 a), which is almost the size of  $\Delta_{1/2}^* \approx 160 \mu\text{eV}$  of each electrode. Within the detected range the anti-crossing strength stays roughly constant at  $70 \mu\text{eV}$ , which is consistent with only small change of  $\Gamma$ . To shed more light on the complex subgap structure of these measurements, we follow a resonant tunneling model approach to understand the origin of the observed characteristics.

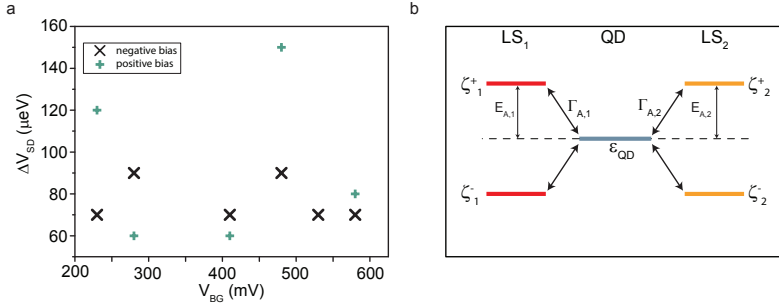


**Figure 7.7. Extracted anti-crossing and schematic energy diagram of resonant tunneling model.** **a** Energy difference in  $eV_{SD}$  of the anti-crossing of CB resonances presented in Fig.7.6 at positive bias voltage (green) and negative bias voltage (black). **b** Energy diagram of expanded resonant tunneling model, where QD level  $\epsilon_{QD}$  is depicted in green. The symmetric single electron levels  $\zeta_{1/2}^{+/-}$  at energies  $E_{A,1/2}$ , mimicking the ABS transitions, are depicted in red and orange for each lead segment respectively. The coupling between  $\zeta_{1/2}^{+/-}$  and  $\epsilon_{QD}$  is labeled with  $\Gamma_{A,1/2}$ .

### 7.3.3. Resonant tunneling model

To obtain a qualitative understanding of the presented data, we employ a model based on resonant tunneling, in an S - QD - S configuration. Due to the complexity of the observed features, we need to make several adjustments to the previously used model (chapter 5). In general, the current  $I$  is given by [95, 97]:

$$I = \int_{-\infty}^{\infty} dE D_{S1}(E + eV_{SD}) \cdot D_{S2}(E) \cdot T_{QD}(E, V_{BG}, V_{SD}) [f_{S2}(E) - f_{S1}(E + eV_{SD})], \quad (7.1)$$

with  $D_{S1,2}(E)$  the DOS in the respective lead segments  $LS_{1,2}$  and  $f_{S1/2}$  represent the Fermi distribution functions, while  $T_{QD}(E, V_{BG}, V_{SD})$  is the Lorentzian transmission function accounting of the quantum dot. We artificially add single particle levels  $\zeta_{1/2}^{+/-}$  symmetrically at energies  $E_{A,1/2}$  (see. Fig. 7.7 b), similar as Ref. [43]. By doing so, we mimic the excitations of an ABS in the respective lead segment  $LS_{1/2}$ . In the model, these levels are pinned to the chemical potential of source and/or drain, i.e. in  $LS_1$  and/or  $LS_2$ . We note, that we do not include the theoretically expected gate dependence of the ABS (Sec. 2.3.4). Furthermore, the levels  $\zeta_{1/2}^{+/-}$  can couple to the QD level  $\epsilon_{QD}$  (set

to 0), which we model by a coupling strength  $\Gamma_{A,1/2}$  (c.f. Fig. 7.7 b), resulting in the following matrix written in the basis  $(\varepsilon_{QD}, \zeta_1^+, \zeta_1^-, \zeta_2^+, \zeta_2^-)$ :

$$M = \begin{bmatrix} 0 & \Gamma_{A,1} & \Gamma_{A,1} & \Gamma_{A,2} & \Gamma_{A,2} \\ \Gamma_{A,1} & -eV_1 + E_{A,1} & 0 & 0 & 0 \\ \Gamma_{A,1} & 0 & -eV_1 - E_{A,1} & 0 & 0 \\ \Gamma_{A,2} & 0 & 0 & -eV_2 + E_{A,2} & 0 \\ \Gamma_{A,2} & 0 & 0 & 0 & -eV_2 - E_{A,2} \end{bmatrix}$$

where  $E_{A,1/2}$  is the energy of the respective levels  $\zeta_{1/2}^{+/-}$  and  $\Gamma_{A,1/2}$  is the coupling to the QD level. The ABS energies  $E_{A,1/2}$  are pinned to the chemical potential  $V_{1/2}$  of the respective electrodes  $LS_{1/2}$ . After diagonalising this matrix, we obtain new eigenvalues for all energy levels. We assume the same Lorentzian shape for all levels and combine them in the Lorentzian transmission function  $T_{QD}$  (see equation 7.1). We stress that the resulting amplitude is therefore not calculated correctly within this simple model.

In addition, we can model the soft edges of the peaks at the gap edge by expressing the  $LS_{1/2}$  DOSs by using the phenomenological Dynes parameter  $\delta_{1/2}$  [152]:

$$D_{S1/2} = \left| \Re \left( E - i\delta_{1/2} \right) / \sqrt{(E - i\delta_{1/2})^2 - \Delta_{1/2}^{*2}} \right|. \quad (7.2)$$

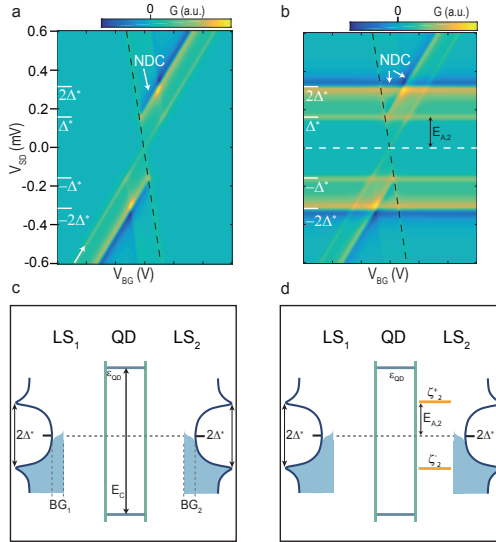
Softening the superconducting gap with the Dynes parameter does not allow to reproduce our experimental findings. In addition, we need to add a constant background DOS  $D_{BG1/2}$  to both  $D_{S1,2}(E)$ , accounting for a finite single particle DOS in the energy gap, while the edges of the gap remain sharp. Increasing the Dynes parameter  $\delta_{1/2}$  also adds a finite DOS inside the gap, but smears out the BCS coherence peaks. Since we do not see any sign for a change in magnitude of the gap, we keep  $\Delta_{1/2}^*$  for both  $LS_{1/2}$  fixed at  $\Delta_{1/2}^* = 160 \mu\text{eV}$ . Furthermore, as the QD resonance broadening stays constant for this gate range, we set it to  $\Gamma = 20 \mu\text{eV}$ . The Dynes parameters  $\delta_{1/2}$  are fixed to  $\delta_{1/2} = 10 \mu\text{eV}$ , as well as the constant DOS background  $D_{BG1/2} = 1$  on both sides with respect to the DOS in the normal state. By turning on the gate independent transmission of the single electron levels  $\zeta_{1/2}^{+/-}$ , mimicking the ABS transitions, at  $\pm\Delta^*$  as well as the coupling between the artificial ABS levels and the QD level  $\Gamma_{A,1/2}$ , we can reproduce most of the detected characteristics.

Fig. 7.8 and Fig. 7.9 show a step by step construction in this toy model, whereas the top row shows the resulting conductance maps, based on the energy diagrams presented in the respective lower row.

We begin with the simplest situation, a S - QD - S system with a soft gap and in the absence of Andreev levels (see Fig. 7.8 c). The resulting conductance map yields a shift of the CB diamond tips in energy by  $\pm 2\Delta^*/e$  and

in gate voltage by  $\Delta V_{BG} = 2\Delta^*/\beta_- e$ , as shown in Fig. 7.8 a, as discussed in section 2.3.1 [97]. In addition, we observe a resonance running through the superconducting gap (indicated with white arrow), which is a result of the softness of the gap. Here, the Fermi level of both reservoirs is aligned to the QD resonance, resulting in this line for a remaining non-zero DOS at zero bias. This is only observable for a soft gap and for a resonance broadening of the QD significantly smaller than the superconducting gap  $\Gamma < \Delta^*$  (see also chapter 5). We note that NDC is also present inside one CB resonance. This part of the model accounts for the detected shift of the CB diamond tips and the NDC in the measurements, but can not reproduce the observed sub-gap resonances.

We therefore artificially add the single particle levels  $\zeta_2^{+/-}$  at energies  $E_{A,2} = 160 \mu\text{eV} = \Delta^*$  in  $\text{LS}_2$  with  $\Gamma_{A,2} = 0$  (see Fig. 7.8 d). This resulting conductance map is shown in Fig. 7.8 b. We now observe resonances at



**Figure 7.8. Resonant tunneling model for S - QD - S.** a,b Resulting conductance map of the resonant tunneling model, based on the respective energy diagrams, as shown in the panels below c,d. c S - QD - S system with constant background density  $D_{BG1/2}$ . d S - QD - S system with additional single electron levels  $\zeta_2^{+/-}$  (orange) in  $\text{LS}_2$  at energies of  $E_{A,2}$ , mimicking the ABS transitions.

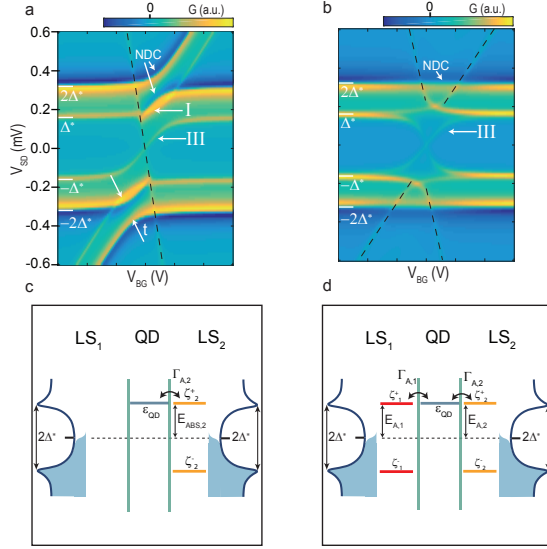


**Figure 7.9. Resonant tunneling model for anti-crossing.** **a,b** Resulting conductance maps, based on resonant tunneling model with respective energy diagrams shown in the panels below. **c** Same system as in Fig.7.8d but with finite coupling  $\Gamma_{A,2}$  between the levels  $\zeta_2^{+/-}$  (orange) and the QD level. **d** Same configuration as in **c**, but with additional level  $\zeta_1^{+/-}$  (red) in  $LS_1$  (at energy  $E_{A,1}$ ) with coupling strength of  $\Gamma_{A,1}$  to the QD level. The anti-crossing between the level  $\zeta_1^{+/-}$  and the QD is labeled with  $t$ .

energies of  $E_{A,2}$  and  $\Delta^* + E_{A,2}$  that are gate independent. Furthermore, these resonances cross the QD resonances unaffected. This is consistent with our experiments, where the ABSs at the gap edge occur in the cotunneling spectrum inside the CB region, which are weakened when moving away from the charge degeneracy point. The characteristics which is missing, compared to the resonances shown in Fig.7.6, are the anti crossing of the ABS (type *I*) with the Coulomb resonance at  $\Delta^* + E_{A,2}$  as well as the subgap resonances of type *II*, *III* at lower energies.

In order to account for the observed anti-crossing/hybridisation of the QD level with the ABS, we introduce a finite coupling  $\Gamma_{A,2}$  between them (Fig. 7.9 c). The resulting conductance map for a coupling strength of  $\Gamma_{A,2} = 60 \mu\text{eV}$  is shown in Fig. 7.9 a. We observe an asymmetric anti-crossing  $t$  of the resonance at  $\Delta^* + E_{A,2}$  with the CB resonance (with positive slope), while



the QD resonance with negative slope is unaffected and runs straight through the gap. This resonance begins to bend towards energies of  $E_{A,2} (= \pm\Delta^*)$ , where it stops when meeting the Coulomb resonance with negative slope. Furthermore, we observe NDC within the anti-crossing of this level and the CB resonance. In order to directly compare the results of this part of the toy model with a representative CB resonance, we directly compare resonance *D* of Fig. 7.6 with the result of Fig. 7.9 a in Fig. 7.10. Here, the anti-crossing of the ABS at the gap edge (type *I*) with the QD level is reproduced well with the model. We observe a resonance running at energies  $\pm\Delta^*$ , which bends towards lower energy, when approaching the charge degeneracy point where it crosses zero. Qualitatively, this reproduces the observed characteristics of the resonances of type *III* very well, but can not account for the observation of resonance type *II*. We note that we can only create this feature with a constant background density on both sides  $D_{BG1/2}$ , accounting for the required DOS inside the gap. Furthermore we stress that the asymmetry in the result of the model is caused by the fact that the artificial ABS level  $\zeta_2^{+/-}$  is added only on one side (LS<sub>2</sub>).

In order to reproduce the resonances of Fig. 7.6f at larger  $V_{BG}$  and the characteristics of the subgap resonances, we need to add an additional single electron level mimicking a second ABS at energy  $E_{A,1} (= E_{A,2})$  in LS<sub>1</sub>. We further cou-

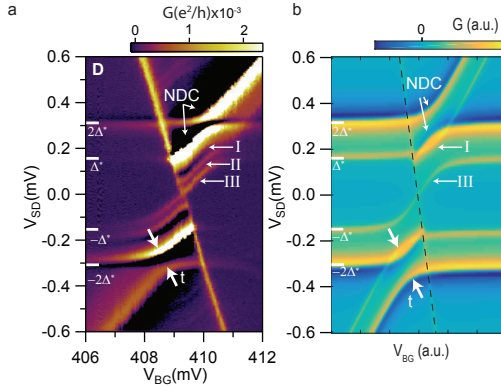


**Figure 7.10. Comparison of Coulomb resonance with result of resonant tunneling model. a** Coulomb resonance *D* of Fig. 7.6. **b** Result of resonant tunneling model of Fig. 7.9 a. Qualitative agreement of the model with the measurements, concerning resonance type *I* and *III*, as well as anti-crossing *t* and NDC. Resonance *II* can not be reproduced with our model.

ple this level  $\zeta_1^{+/-}$  with the same coupling strength  $\Gamma_{A,1}$  to the QD as  $\zeta_2^{+/-}$  in  $LS_2$  ( $\Gamma_{A,1/2} = 60 \mu\text{eV}$ ), as illustrated in Fig. 7.9 d. We now observe a cross-like structure for the resonances running at  $E_{A,1} = E_{A,2} (= \pm \Delta^*)$  (Fig. 7.9 b), very similar to the resonances shown in Fig. 7.6 f,g. We also note that for this configuration we can't reproduce the symmetric anti crossing with both Coulomb resonance at  $\pm 2\Delta^*$ , that we observe in the measurement.

Our model reproduces most of the observed features by using a modified resonant tunneling model mimicking ABS transitions with single electron levels, coupled to a single QD level. Adding artificial ABS levels in only one lead segment results qualitatively in the detected asymmetric anti-crossing, i.e. the hybridisation of an ABS with the QD. What we are missing in our toy model is the resonance of type *II* and the anti crossing in the symmetric case. We further point out, that adding more discrete levels (ABSs) into the model leads to more complex structures, but does not describe the resonance of type *II* (see appendix D.2). We therefore interpret the observed type *II* resonance as a replica of type *III*, because of there similarity of characteristic properties (FWHM, amplitude). The origin of this resonance might be related to coupling to a bosonic bath of the environment, similar to Ref. [97].

### 7.3.4. Conclusions

We performed measurements in three distinct transport regimes, detected a supercurrent in the open regime with no signature of the integrated QD and saw transport being dominated by the QD in the weak coupling regime.

In the intermediate regime, where  $\Gamma \sim \Delta^*$ , we observe a hybridisation of the QD states with the ABS in the NW lead caused by the strong coupling of the ABS to the QD. By using a resonant tunneling model, we can account for most of the observed characteristics. By mimicking the ABS transitions with single electron levels, the model reproduces the subgap resonances *I* and *III*, as well as the asymmetric anti-crossing of the ABS (*I*, in  $LS_{1/2}$ ) with the QD level.

We point out, that in the model the discrete single electron levels  $\zeta_{1/2}^{+/-}$  hold the same properties as the QD level, despite one crucial difference; these levels are symmetric around zero energy, mimicking the electron hole symmetry of a superconducting state. Furthermore, the detected NDC is also reproduced well by the model.

This suggest that an ABS in only one of the NW leads is strongly coupled to the QD. However, we can not fully reproduce the symmetric case. The observations in the measurements, suggest a change in coupling to the second NW lead, dependent on the applied gate voltage.

Based on the model, we can not provide a clear explanation for the detected type *II* resonance but suggest that it as replica of type *III*, possibly related to a coupling to a bosonic bath of the environment [97].

In order to reproduce the detected features, we needed to add a constant

background DOS to the BCS like DOS of each lead segment. Using only the phenomenological Dynes parameter did not reproduce our results sufficiently. We suggest, that our experimental findings could be the result of a finite coupling between even/odd parity states of the ABS with the even/odd states of the QD, leading to the detected hybridisation. An alternative explanation for the type *II* resonance might be a finite coupling between an ABS in one lead segment  $LS_1$  and a second ABS in  $LS_2$ . In order to shed more light on this, further investigations and a more sophisticated theoretical model are required.



## 8 Cooper-pair splitting in two parallel InAs nanowires<sup>1 2</sup>

---

In the following chapter we demonstrate fabrication and electrical characterization of an InAs double - nanowire (NW) device consisting of two closely placed parallel NWs. Both NWs are connected to one common superconducting contact, whereas the two NWs are individually connected to separated normal metal electrodes. We observe Cooper-pair splitting (CPS) in this new generation of devices, with a sizeable efficiency of correlated currents in both NWs (see also section 2.5.1). Compared to previous reports, where Cooper-pair splitting was detected in devices which are based on single NWs [4, 176–179], we detect an *interwire* interaction mediated by the common superconductor, instead of an intrawire electron pairing. Interwire interaction is especially important, as it plays an important role in the realization of zero-magnetic field Majorana bound states [13, 29, 30, 180, 181], or Parafermions [15]. Furthermore, we detect additional resonances, only apparent in the superconducting state, which we attribute to Andreev Bound states [90, 117, 182] and/or Yu-Shiba resonances [150], which are most likely formed in the proximitized NW segment.

### 8.1. Double nanowire device and characterization

The investigated sample is presented schematically in Fig. 8.1 (a). Two InAs semiconducting NWs with large spin orbit interaction are aligned in parallel (NW<sub>1</sub> green, NW<sub>2</sub> red) and electrically coupled to a (single) common superconductor S (blue). The two NWs are individually connected to normal metal electrodes N<sub>1/2</sub> (yellow). Two sidegates SG<sub>1/2</sub> are placed on each side of the NWs, to tune the chemical potentials of both quantum dots (QDs) individually, which are created between N<sub>1/2</sub> and S respectively. The precise location of both quantum dots is unknown, since no additional barrier gates are used in this experiment [183].

We already would like to point out here, that the electronic boundary condi-

---

<sup>1</sup>Parts of this chapter are results from a collaborative work together with Shoji Baba in the group of Seigo Tarucha from University of Tokyo.

<sup>2</sup>Parts of this chapter are published similarly in Ref. [175], with permission of © 2018 IOP Publishing.

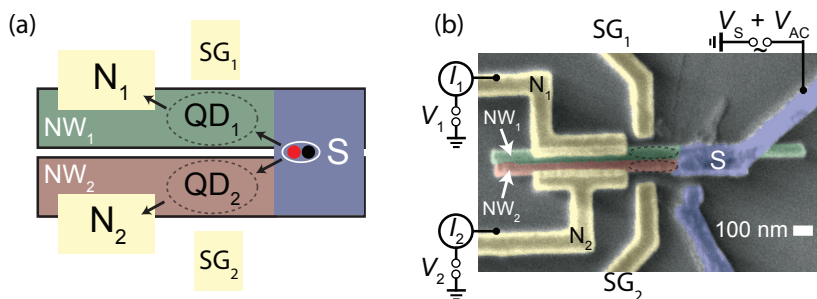


**Figure 8.1. Cooper-pair splitting setup in two parallel nanowires.**

(a) Scheme of the double NW Cooper-pair splitting device. Two individual InAs NWs,  $NW_{1/2}$ , are placed in parallel, having one common superconducting electrode (blue) and two separated normal metal contacts,  $N_{1/2}$ . Two quantum dots ( $QD_{1/2}$ ) are formed in the NWs and tuned individually by the local sidegates  $SG_{1/2}$ . (b) SEM micrograph of the measured sample, which consists of two  $NW_{1/2}$  with a common superconducting contact, made of Al. Individual normal metal contacts,  $N_{1/2}$ , are made of Au, as well as the sidegates  $SG_{1/2}$ . The measurement geometry is presented schematically [175]. © 2018 by IOP Publishing.

tions on the side of the superconductor might be changed, when the superconductor is turned into the normal state, because of the proximity effect. Besides local Cooper pair tunneling from the superconductor to the normal metal contacts  $N_{1/2}$  [97], Cooper pairs (white circle with red/black dot) can also be split, which then results in a non-local current consisting of entangled single electrons. This effect is expected to be enhanced, when both quantum dots,  $QD_{1/2}$ , are in the sequential tunneling regime, which allows electrons to tunnel sequentially from the superconductor to both normal metal contacts.

## Fabrication

The NWs which we use in this study are made of InAs (wurtzite crystal phase), having a diameter of  $\sim 80$  nm. In order to fabricate a device, we first transferred the NWs from their growth ship to the substrate and afterwards post selected NW pairs which lie next to each other by using standard SEM imaging. Importantly, we note that the NWs are not electronically connected, as they are separated by their native oxide (thickness of about 2 nm to 3 nm), which surrounds each of the NW. In the next step, we place the common superconductor, consisting of Ti/Al (3 nm/90 nm) after removing the native

oxide using a solution of  $(NH_4)_2S_x$  [130]. Next, both normal metal electrodes  $N_{1/2}$ , which consist of Ti/Au (3 nm/130 nm) are evaporated together with the sidegates  $SG_{1/2}$ . In Fig. 8.1(b) we present a SEM image of the actual sample. The superconductor and the normal metal electrodes are separated by 250 nm.

## Characterization

All measurements have been performed at a temperature of about 50 mK. We measure differential conductance  $dI/dV$  of both NWs simultaneously, by using synchronized lock-in techniques (as shown schematically in Fig. 8.1 (b)). Fig. E.1 in the appendix shows characteristic CB diamond measurements, indicating two individual QDs,  $QD_1$  and  $QD_2$ , in each of the NW, similar to previous results [184]. From these measurements, we can determine the following parameters for the two individual QDs: charging energy  $U$ , single particle level spacing  $\epsilon$  and the life-time broadening  $\Gamma$ :  $U_{1,2} = 0.5 - 0.7$  meV,  $\epsilon_1 = 0.3 - 0.5$  meV,  $\epsilon_2 = 0.1 - 0.3$  meV,  $\Gamma_1 = 0.1 - 0.2$  meV and  $\Gamma_2 = 0.2 - 0.3$  meV for  $QD_1$  and  $QD_2$ , respectively. The characteristic properties of both QDs are rather similar and suggest that each QD is created between the superconducting Al electrode and the normal metal Au reservoirs. Furthermore, we detect a suppression of conductance for some regions for energies lower than the superconducting energy gap  $\Delta$ , which we find to be  $\sim 150$   $\mu$ eV, similar to previous studies [177]. Consequently, we are in the limit where  $\Delta < \Gamma$ , meaning that local pair tunneling should exceed Cooper-pair splitting [185, 186]. We further note, that it is not possible to distinguish individual tunnel couplings  $\Gamma_{1/2}$  of each QD to either S or N. The ratio of the tunnel rates has an important influence on the magnitude of Cooper-pair splitting. As observed in previous experiments, CPS can be substantially suppressed when tunneling out of the QD into the drain electrode is the rate-limiting step [179, 186]. In addition, we expect no influence of inter dot tunnel between both QDs, as they are placed in two different NWs, in contrast to earlier experiments.

## 8.2. Cooper pair Splitting in double NW

Figs. 8.2 (a) and (b) present simultaneously measured differential conductance  $G_1$  of  $QD_1$  and  $G_2$  of  $QD_2$  with respect to the applied gate voltages  $V_{SG1/SG2}$  respectively. The measurement have been performed at zero bias and no external magnetic field was applied. Tuning the sidgate  $V_{SG1}$  shifts  $QD_1$  through several CB resonances, which results in a series of conductance peaks recorded in  $G_1$ . Very similar, changing  $V_{SG2}$  shifts the resonances of  $QD_2$  in NW<sub>2</sub>. For each detected resonance, the charge state of the respective QD is changed, which can be sensed by the other QD, since both QDs are coupled capacitively. Here,  $QD_2$  plays the role of a good charge sensor of the charge on  $QD_1$ , as the CB resonances of  $QD_1$  shift substantially every time the charge on  $QD_2$

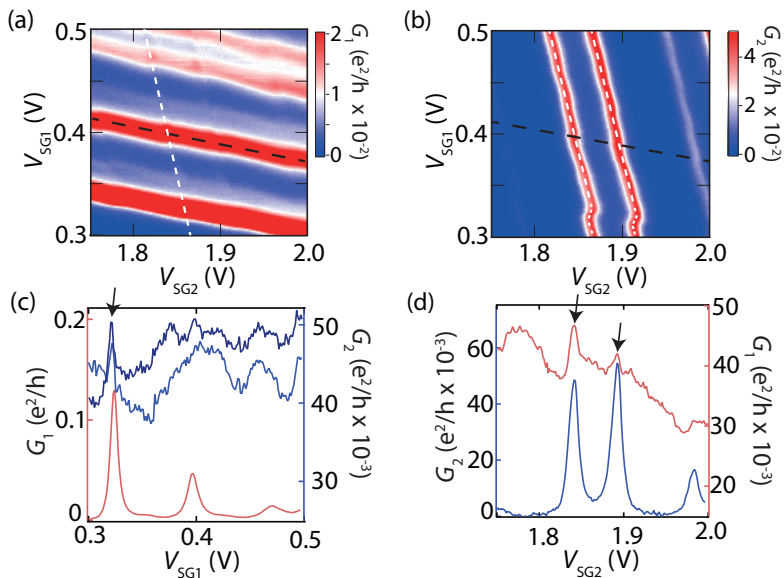


**Figure 8.2. Cooper pair splitting with quantum dots in two parallel nanowires.** (a) Differential conductance  $G_1$  of QD<sub>1</sub> with respect to  $V_{SG1/2}$ . (b)  $G_2$  of QD<sub>2</sub> as a function of  $V_{SG1/2}$ . (c) cross sections taken at the white lines of (a) and (b). (d) cross sections taken at the black dashed lines of (a) and (b) [175]. © 2018 by IOP Publishing.

is changed by one electron (presented in Fig. 8.2 (b)). Because of capacitive crosstalk from  $V_{SG1}$  on QD<sub>2</sub> (and  $V_{SG2}$  on QD<sub>1</sub>) the position of the resonances is a bit tilted in each of the graphs.

For some settings of side gate voltages  $V_{SG1/2}$ , an increase of conductance on both sides is very clearly detected, in case both QDs are on resonance. This is best seen in the cross sections, presented in Figs. 8.2 (a) and (b). By following the cross section (black line) in Fig. 8.2 (a) we detect an enhancement of  $G_1$  at the same position of the peak of  $G_2$  for the two resonances at  $V_{SG2} \approx 1.87$  V and  $V_{SG2} \approx 1.91$  V (see arrows), while other possible correlations are less clear. Following the white dashed line, similar correlations are observed in the cross sections of  $G_2$  at the peak positions of  $G_1$ , as shown in Fig. 8.2 (b). The positive correlation is clearly seen at  $V_{SG1} \approx 0.32$  V (arrow), whereas the correlation is only weakly detected for the other two resonances at  $V_{SG1} \approx 0.4$  V and  $V_{SG1} \approx 0.49$  V. Consequently, we believe that we see a positive correlation



between  $G_1$  and  $G_2$  on three resonances, which we can assign to Cooper-pair splitting from the superconducting electrode into  $QD_1$  and  $QD_2$ . When an external magnetic field (250 mT, out of plane) is applied (see Fig. 8.3), which is larger than the critical magnetic field  $B_C$  of the aluminum electrode, the former positive correlations between  $G_1$  and  $G_2$  are completely absent. This proves that the positive correlations in conductance originate from Cooper-pair splitting. The Cooper-pair efficiency is defined as:  $2G_{CPS}/G_{total}$ , which results in a maximum efficiency of  $\approx 20\%$ , which is similar to what has been reported earlier in samples based on a single NW.

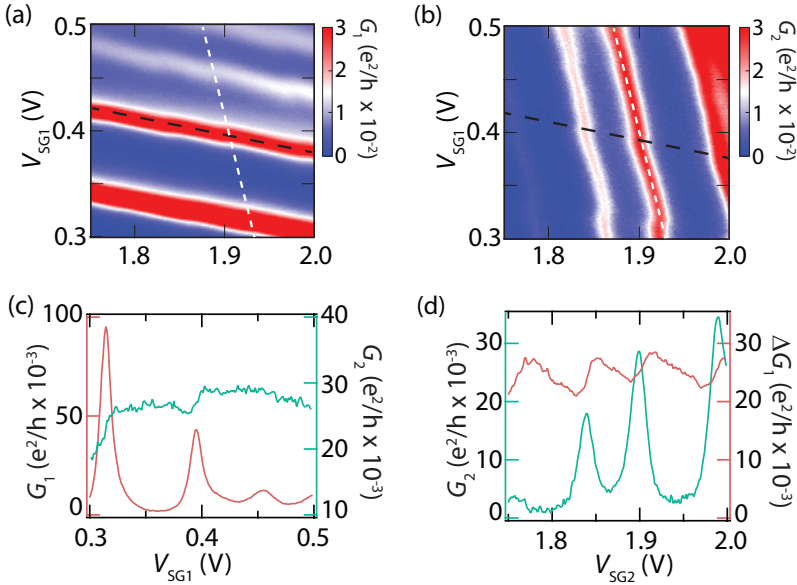


**Figure 8.3. Normal state measurements.** (a), (b)  $G_1$  and  $G_2$  of  $QD_{1/2}$  with respect to the sidegate voltages  $V_{SG1}/V_{SG2}$ . Out of plane external magnetic field of 250 mT is applied. (c), (d) Cross sections taken at white/black dashed line of (a) and (b). Positively correlated signal, shown in Fig.8.2 is absent in the presence of external magnetic field. In (d) a linear background has been removed of  $G_1$ , which is why we call it  $\Delta G_1$  [175]. © 2018 by IOP Publishing.

### Cooper pair splitting with second type of resonances

We now discuss a very similar type of measurement, as presented in Fig. 8.2, in a different sidegate regime, depicted in Fig. 8.4. For this setting of gate voltages, we detect two sets of resonances for QD<sub>1</sub>. In addition to the QD resonances, which we presented in Fig. 8.2 (indicated here with type *I*), we observe a second set of resonances (from now on referred to as type *II*). In contrast to this, we detect only one set of QD resonances for QD<sub>2</sub>. We will demonstrate, that the type *II* resonances are very different when compared to the type *I* resonances.

First, the amplitude of type *II* resonances is only half of the amplitude of type *I* resonances. In addition to this, the resonances of type *II* have a different slope, when compared to resonances of type *I*, which indicates that they differ

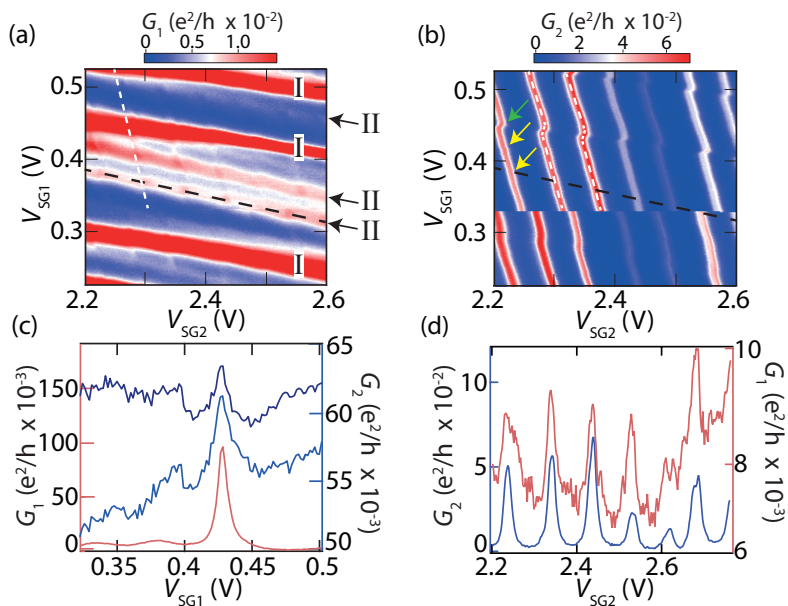


**Figure 8.4. Cooper pair splitting with second type of resonances.** (a)  $G_1$  of QD<sub>1</sub> with respect to sidegate voltages  $V_{SG1}$  and  $V_{SG2}$ . Second set of resonances is indicated with *II* (black arrows). (b) Differential Conductance  $G_2$  respectively for QD<sub>2</sub>. (c) cross sections taken at dashed white lines of (a) and (b). (d) cross sections taken at black dashed line of (a) and (b) [175].

© 2018 by IOP Publishing.

in their capacitive coupling to  $SG_1$  and  $SG_2$ . The broadening of both types of resonances also differs, roughly by a factor of two:  $\Gamma_I = 0.5 \text{ meV}$ , while  $\Gamma_{II} = 1.2 \text{ meV}$ . Most strikingly, type *II* resonances fully vanish when we apply an external magnetic field (not presented), meaning they only appear in the superconducting state. Furthermore, the conductance of  $QD_2$  only acts on a change in charge state of  $QD_1$  for resonances of type *I* (indicated by green arrow in Fig. 8.4 (b)) but does not react to the resonances of type *II*. Hence, it seems that the charge state is not changed as  $QD_2$  does not sense these resonances (highlighted by yellow arrows in Fig. 8.4 (b)). Consequently, we are convinced that resonances of type *II* can not be CB resonances. The origin of these states has to be within the superconducting phase, most likely close to the superconducting electrode. Although the type *II* resonances are not CB resonances, we can still record Cooper-pair splitting with them. A clear positive correlation is observed between  $G_1$  and  $G_2$  in Fig. 8.4 (d) and also in Fig. 8.4 (c). The splitting efficiency is determined to be  $\approx 13\%$  for type *II*, which is similar to what we calculated for resonances of type *I* in the other sidegate region presented in Fig. 8.2.

Since the resonances of type *II* can be tuned by the sidegates, we believe that this suggests the existence of sub-gap states, which are not located in  $QD_1$ , but rather in the nanowire segment, which is connected to the superconductor, as they are not fully screened by the superconductor. Consequently, we suggest that a proximitized region is created in  $NW_1$ , which is extended out from the superconductor to some distance into the nanowire, which is then coupled to  $QD_1$ . Inside this nanowire lead segment, subgap states can be formed, because of potential fluctuations or residual disorder in at one the NWs. In general, we can think of two kinds of superconducting bound states, namely Andreev bound states (ABS) [90, 117, 182] or Yu-Shiba Rusinov (YSR) [150] states. In general, these states don't appear at zero energy, but could be tuned electrically to zero energy, signaling a ground state transition between the proximitized lead region and the bulk of the superconductor. This can result in an increase in the DOS inside the superconducting energy gap of the superconductor, which causes an enhancement of the subgap conductance which we measure. For this situation we can think of two electrons which are launched by Cooper-pair splitting are transmitted in a different way to the respective drain electrodes. One electron takes the path through  $QD_2$  and is then transferred by the usual sequential tunneling process, while the other electron can take the path via  $QD_1$ , transferred by co-tunneling. In principle, we could expect that this process suppresses Cooper-pair splitting as the latter one corresponds to a low probability for out-tunneling into the drain contact. However, because of the existing sub-gap resonances in the proximitized nanowire lead segment, this process can be also enhanced and one can therefore reach almost similar CPS efficiencies. Despite disorder in at least one of the nanowires we present a significant CPS efficiency, the first fundamental

effect which is required for the creation of NW-based Parafermions. Future samples with less disorder could also show larger CPS efficiencies, which is relevant for the non-local superconducting correlation.

### 8.3. Conclusion

In summary, we present the fabrication of an electronic sample, which consists of two closely aligned parallel InAs NWs, contacted by one common superconductor and individual normal metal contacts. Tuning individual sidegate voltages allows us to address the QDs which are formed in each NW separately. In the resonant tunneling regime of both QDs, we detect Cooper-pair splitting with efficiencies of up to 20%. In a certain sidegate regime, we observe a second set of resonances in one of the NWs, which is only apparent in the superconducting state of the device. We find, that the second set of resonances are no CB resonances, hence, are not related to a change of charge state of the QD. Since they only appear in the superconducting state, we tentatively assign the second set of resonances to superconducting subgap states which are formed in the nanowire lead segment, which is connected to the superconductor.

With this experiment, we demonstrate a new nanowire hybrid platform, which is suitable to implement the next milestone in topological quantum computation, namely Parafermions. Cooper-pair splitting in our sample is most likely enhanced by the Coulomb charging energy of the QDs, which have been formed in the NW segments. For future experiments, we would be interested in investigating the question, whether these interactions, or alternatively intra-wire electron-electron interactions can be sufficiently strong enough to generate nonlocal superconducting correlations between both nanowire segments *below* the superconducting electrode in order to generate Parafermions in such device architectures.

## 9 Summary and outlook

---

Within the scope of this thesis we studied indium arsenide (InAs) nanowire (NW) hybrid devices using integrated QDs, mainly by means of tunnel spectroscopy.

We characterized QDs in InAs NWs, defined by crystal phase engineering, namely wurtzite (WZ) and zinc-blende (ZB) crystal phase. We established sophisticated SEM techniques (ECCI) enabling the detection of the WZ tunnel barriers and thereby their location and the size of the QD. We carried out characterization measurements of these QDs and found a systematic increase of the QD resonance broadening as a function of gate voltage. We qualitatively explained the observed exponential increase of the resonance broadening with a linear reduction of the tunnel barrier height with respect to the Fermi energy. We found that the resonance broadening can be tuned over a large range ( $\approx 50 \mu\text{eV}$  up to  $\approx 1 \text{ meV}$ ). We further presented Coulomb diamond measurements, revealing large level spacings ( $1 \text{ meV}$  to  $3 \text{ meV}$ ) and large charging energies ( $\approx 7 \text{ meV}$ ). This confirms the suitability of this system, as a well controlled electronic spectrometer, as the QD levels are well separated from one another and can be very sharp (chapter 4).

We used this platform as a new tunnel spectroscopy tool for the investigation of the proximity induced gap of a superconductor in a nanowire segment. We demonstrated the possibility to use the QD as a spectrometer in two different transport regimes: in Coulomb blockade, where the QD effectively acts as a single tunnel barrier and on resonance, where transport is dominated by first order sequential tunneling. Using both methods allowed us to detect the evolution of the induced gap in the nanowire lead segment, which we explained by a gate tunable transition from the long to the short junction limit (chapter 5).

In addition, we performed spectroscopy measurements on the NW lead segment in presence of discrete states. We detected superconducting sub-gap states originating from Andreev type processes. Thus, we demonstrate the possibility to employ ZB/WZ QDs as spectrometers for individual sub-gap states in NW segments (chapter 6).

Coupling a InAs NW with crystal phase defined QD to two superconducting contacts gave access to three different transport regimes in the same device. We presented supercurrent measurements in the open regime, Coulomb blockade in the weak coupling regime and hybridization of Andreev bound states (ABS) with the QD states in the intermediate coupling regime. We qualitatively explained the observed asymmetric anti-crossing of the ABS and the QD level by using a resonant tunneling model, mimicking a coupling of one ABS in (one NW segment) to the QD (chapter 7).

Furthermore, we presented results on devices consisting of two InAs nanowires. By coupling two parallel aligned InAs NWs to one common superconductor and two individually connected normal metal electrodes, we demonstrated Cooper pair splitting in this new type of platform. This provides the basis for devices towards the detection of parafermions (chapter 8).

In this thesis, we presented the next generation of nanowire devices. To solve current problems, we demonstrated that it is very advantageous to perform electronic tunneling spectroscopy in NWs by means of tunnel barrier defined (“integrated”) QDs. Integrated QDs could potentially serve as a powerful spectroscopic tool, not only to unambiguously detect MBSs, but also to distinguish topological states from trivial ABSs. The results presented in this thesis lay the groundwork for further spectroscopic studies of MBS characteristics. Furthermore, continuing experiments based on two nanowires can lead to the detection of new topologically protected states, such as parafermions. Especially using two parallel NWs both having an integrated QD might be of great interest to study such states and therefore provide a potential building block for quantum information processing.

# Bibliography

- [1] S. De Franceschi, L. P. Kouwenhoven, C. Schöenberger, and W. Wernsdorfer, *Nature Nanotechnology* **5**, 703 (2010).
- [2] L. Hofstetter, A. Geresdi, M. Aagesen, J. Nygård, C. Schöenberger, and S. Csonka, *Phys. Rev. Lett.* **104**, 246804 (2010).
- [3] Y.-J. Doh, J. A. van Dam, A. L. Roest, E. P. A. M. Bakkers, L. P. Kouwenhoven, and S. De Franceschi, *Science (New York, N.Y.)* **309**, 272 (2005).
- [4] L. Hofstetter, S. Csonka, J. Nygård, and C. Schöenberger, *Nature* **461**, 960 (2009).
- [5] S. Nadj-Perge, S. M. Frolov, E. P. A. M. Bakkers, and L. P. Kouwenhoven, *Nature* **468**, 1084 (2010).
- [6] S. Nadj-Perge, V. S. Pribiag, J. W. G. Van Den Berg, K. Zuo, S. R. Plissard, E. P. A. M. Bakkers, S. M. Frolov, and L. P. Kouwenhoven, *Physical Review Letters* **108** (2012), 10.1103/PhysRevLett.108.166801.
- [7] A. Stern and N. H. Lindner, *Science* **339**, 1179 (2013).
- [8] J. Alicea, *Physical Review B* **81**, 125318 (2010).
- [9] Y. Oreg, G. Refael, and F. von Oppen, *Physical Review Letters* **105**, 177002 (2010).
- [10] J. Alicea, Y. Oreg, G. Refael, F. von Oppen, and M. P. A. Fisher, *Nature Physics* **7**, 412 (2011).
- [11] S. Das Sarma, M. Freedman, and C. Nayak, *Nature Publishing Group* (2015), 10.1038/npjqi.2015.1.
- [12] C. Nayak, S. H. Simon, A. Stern, M. Freedman, and S. D. Sarma, *Reviews of Modern Physics* **80**, 1083 (2008).
- [13] V. Mourik, K. Zuo, S. M. Frolov, S. R. Plissard, E. P. A. M. Bakkers, and L. P. Kouwenhoven, *Science* **336** (2012), 10.1126/science.1222360.
- [14] A. Keselman, L. Fu, A. Stern, and E. Berg, *Physical Review Letters* **111**, 116402 (2013).
- [15] J. Klinovaja and D. Loss, *Physical Review B - Condensed Matter and Materials Physics* **90**, 1 (2014).

- [16] E. Gaidamauskas, J. Paaske, and K. Flensberg, *Physical Review Letters* **112**, 233513 (2014).
- [17] S. R. Plissard, I. van Weperen, D. Car, M. A. Verheijen, G. W. G. Immink, J. Kammhuber, L. J. Cornelissen, D. B. Szombati, A. Geresdi, S. M. Frolov, L. P. Kouwenhoven, and E. P. A. M. Bakkers, *Nature Nanotechnology* **8**, 859 (2013).
- [18] J. Gooth, M. Borg, H. Schmid, V. Schaller, S. Wirths, K. Moselund, M. Luisier, S. Karg, and H. Riel, *Nano Letters* **17**, 2596 (2017).
- [19] F. Krizek, T. Kanne, D. Razmadze, E. Johnson, J. Nygård, C. M. Marcus, and P. Krogstrup, *Nano Letters* **17**, 6090 (2017).
- [20] S. Gazibegovic, D. Car, H. Zhang, S. C. Balk, J. A. Logan, M. W. A. de Moor, M. C. Cassidy, R. Schmits, D. Xu, G. Wang, P. Krogstrup, R. L. M. O. het Veld, K. Zuo, Y. Vos, J. Shen, D. Bouman, B. Shojaei, D. Pennachio, J. S. Lee, P. J. van Veldhoven, S. Koelling, M. A. Verheijen, L. P. Kouwenhoven, C. J. Palmstrøm, and E. P. A. M. Bakkers, *Nature* **548**, 434 (2017).
- [21] X. Jiang, Q. Xiong, S. Nam, F. Qian, Y. Li, and C. M. Lieber, *Nano Letters* **7**, 3214 (2007).
- [22] M. T. Björk, B. J. Ohlsson, T. Sass, A. I. Persson, C. Thelander, M. H. Magnusson, K. Deppert, L. R. Wallenberg, and L. Samuelson, *Nano Letters* **2**, 87 (2002).
- [23] K. A. Dick, C. Thelander, L. Samuelson, and P. Caroff, *Nano Letters* **10**, 3494 (2010).
- [24] M. T. Björk, C. Thelander, A. E. Hansen, L. E. Jensen, M. W. Larsson, L. R. Wallenberg, and L. Samuelson, *Nano Letters* **4**, 1621 (2004).
- [25] M. Nilsson, L. Namazi, S. Lehmann, M. Leijnse, K. A. Dick, and C. Thelander, *Physical Review B* **93** (2016), 10.1103/physrevb.93.195422.
- [26] P. Krogstrup, N. L. B. Ziino, W. Chang, S. M. Albrecht, M. H. Madsen, E. Johnson, J. Nygård, C. M. Marcus, and T. S. Jespersen, *Nature Materials* **14**, 400 (2015).
- [27] R. M. Lutchyn, E. P. A. M. Bakkers, L. P. Kouwenhoven, P. Krogstrup, C. M. Marcus, and Y. Oreg, *Nature Reviews Materials* **3**, 52 (2018).
- [28] J. E. Sestoft, T. Kanne, A. N. Gejl, M. von Soosten, J. S. Yodh, D. Sherman, B. Tarasinski, M. Wimmer, E. Johnson, M. Deng, J. Nygård, T. S. Jespersen, C. M. Marcus, and P. Krogstrup, *Physical Review Materials* **2** (2018), 10.1103/physrevmaterials.2.044202.
- [29] S. M. Albrecht, A. P. Higginbotham, M. H. Madsen, F. Kuemmeth, T. S. Jespersen, J. Nygård, P. Krogstrup, and C. M. Marcus, *Nature* **531**, 206 (2016).
- [30] M. T. Deng, S. Vaitiekenas, E. B. Hansen, J. Danon, M. Leijnse, K. Flensberg, J. Nygård, P. Krogstrup, and C. M. Marcus, *Science* **354** (2016), 10.1126/science.aaf3961.



- [31] M. T. Deng, S. Vaitiekėnas, E. Prada, P. San-Jose, J. Nygård, P. Krogstrup, R. Aguado, and C. M. Marcus, *Physical Review B* **98**, 1 (2018).
- [32] H. Zhang, C.-X. Liu, S. Gazibegovic, D. Xu, J. A. Logan, G. Wang, N. van Loo, J. D. S. Bommer, M. W. A. de Moor, D. Car, R. L. M. O. het Veld, P. J. van Veldhoven, S. Koelling, M. A. Verheijen, M. Pendharkar, D. J. Pennachio, B. Shojaei, J. S. Lee, C. J. Palmstrøm, E. P. A. M. Bakkers, S. D. Sarma, and L. P. Kouwenhoven, *Nature* **556**, 74 (2018).
- [33] C. X. Liu, J. D. Sau, T. D. Stanescu, and S. Das Sarma, *Physical Review B* **96**, 1 (2017).
- [34] C. Reeg, O. Dmytruk, D. ü, D. Loss, and J. Klinovaja, *Physical Review B* **98**, 245407 (2018).
- [35] M. Leijnse and K. Flensberg, *Physical Review B - Condensed Matter and Materials Physics* **84**, 1 (2011).
- [36] S. Hoffman, D. Chevallier, D. Loss, and J. Klinovaja, *Physical Review B* **96** (2017), 10.1103/physrevb.96.045440.
- [37] K. Gharavi, D. Hoving, and J. Baugh, *Physical Review B* **94**, 1 (2016).
- [38] D. Chevallier, P. Szumniak, S. Hoffman, D. Loss, and J. Klinovaja, *Physical Review B* **97**, 1 (2018).
- [39] Y.-J. Doh, S. D. Franceschi, E. P. A. M. Bakkers, and L. P. Kouwenhoven, *Nano Letters* **8**, 4098 (2008).
- [40] A. P. Higginbotham, S. M. Albrecht, G. Kiršanskas, W. Chang, F. Kueemmeth, P. Krogstrup, T. S. Jespersen, J. Nygård, K. Flensberg, and C. M. Marcus, *Nature Physics* **11**, 1017 (2015).
- [41] S. Li, N. Kang, P. Caroff, and H. Q. Xu, *Physical Review B* **95**, 1 (2017).
- [42] K. Gharavi, G. W. Holloway, R. R. LaPierre, and J. Baugh, *Nanotechnology* **28**, 085202 (2017).
- [43] Z. Su, A. Zarassi, J.-F. Hsu, P. San-Jose, E. Prada, R. Aguado, E. J. H. Lee, S. Gazibegovic, R. L. M. Op het Veld, D. Car, S. R. Plissard, M. Hocevar, M. Pendharkar, J. S. Lee, J. A. Logan, C. J. Palmstrøm, E. P. A. M. Bakkers, and S. M. Frolov, *Physical Review Letters* **121**, 127705 (2018).
- [44] X. Duan and C. M. Lieber, *Advanced Materials* **12**, 298 (2000).
- [45] W. Lu and C. M. Lieber, *Journal of Physics D: Applied Physics* **39**, R387 (2006).
- [46] J. Bao, M. A. Zimmler, F. Capasso, X. Wang, and Z. F. Ren, *Nano Letters* **6**, 1719 (2006).
- [47] E. C. Garnett, M. L. Brongersma, Y. Cui, and M. D. McGehee, *Annual Review of Materials Research* **41**, 269 (2011).

- [48] P. Offermans, M. Crego-Calama, and S. H. Brongersma, *Nano Letters* **10**, 2412 (2010).
- [49] A. Konar, J. Mathew, K. Nayak, M. Bajaj, R. K. Pandey, S. Dhara, K. V. R. M. Murali, and M. M. Deshmukh, *Nano Letters* **15**, 1684 (2015).
- [50] A. M. Burke, D. J. Carrad, J. G. Gluschke, K. Storm, S. F. Svensson, H. Linke, L. Samuelson, and A. P. Micolich, *Nano Letters* **15**, 2836 (2015).
- [51] S. Dayeh, D. P. Aplin, X. Zhou, P. K. Yu, E. Yu, and D. Wang, *Small* **3**, 326 (2007).
- [52] H. Kosaka, A. Kiselev, F. Baron, K. W. Kim, and E. Yablonovitch, *Electronics Letters* **37**, 464 (2001).
- [53] C. Bloemers, *Electronic Transport in Narrow-Gap Semiconductor Nanowires*, Ph.D. thesis, RWTH Aachen University (2012).
- [54] S. d'Hollosy, *Locally Tunable InAs Nanowire Quantum Dots for Cooper Pair Splitting*, Ph.D. thesis, University of Basel (2014).
- [55] G. Fabian, *Engineered Magnetoconductance in InAs Nanowire Quantum Dots*, Ph.D. thesis, University of Basel (2015).
- [56] R. S. Wagner and W. C. Ellis, *Applied Physics Letters* **4**, 89 (1964).
- [57] C. Thelander, P. Caroff, S. Plissard, A. W. Dey, and K. A. Dick, *Nano Letters* **11**, 2424 (2011).
- [58] S. Lehmann, J. Wallentin, D. Jacobsson, K. Deppert, and K. A. Dick, *Nano Letters* **13**, 4099 (2013).
- [59] M. Nilsson, *Charge and Spin Transport in Parallel-Coupled Quantum Dots in Nanowires*, Ph.D. thesis, Lund University (2018).
- [60] L. J. Lauhon, M. S. Gudiksen, D. Wang, and C. M. Lieber, *Nature* **420**, 57 (2002).
- [61] C. Thelander, M. Björk, M. Larsson, A. Hansen, L. Wallenberg, and L. Samuelson, *Solid State Communications* **131**, 573 (2004).
- [62] A. Fuhrer, L. E. Fröberg, J. N. Pedersen, M. W. Larsson, A. Wacker, M.-E. Pistol, and L. Samuelson, *Nano Letters* **7**, 243 (2007).
- [63] J. Salfi, S. Roddaro, D. Ercolani, L. Sorba, I. Savelyev, M. Blumin, H. E. Ruda, and F. Beltram, *Semiconductor Science and Technology* **25**, 024007 (2010).
- [64] L. Romeo, S. Roddaro, A. Pitanti, D. Ercolani, L. Sorba, and F. Beltram, *Nano Letters* **12**, 4490 (2012).
- [65] A. C. Ford, S. B. Kumar, R. Kapadia, J. Guo, and A. Javey, *Nano Letters* **12**, 1340 (2012).
- [66] S. Chuang, Q. Gao, R. Kapadia, A. C. Ford, J. Guo, and A. Javey, *Nano Letters* **13**, 555 (2013).

- [67] F. Vigneau, V. Prudkovkiy, I. Duchemin, W. Escoffier, P. Caroff, Y.-M. Niquet, R. Leturcq, M. Goiran, and B. Raquet, *Physical Review Letters* **112** (2014), 10.1103/physrevlett.112.076801.
- [68] P. Štředa and P. Šeba, *Physical Review Letters* **90** (2003), 10.1103/physrevlett.90.256601.
- [69] S. Heedt, N. T. Ziani, F. Crépin, W. Prost, S. Trellenkamp, J. Schubert, D. Grützmacher, B. Trauzettel, and T. Schäpers, *Nature Physics* **13**, 563 (2017).
- [70] M. Scheffler, S. Nadj-Perge, L. P. Kouwenhoven, M. T. Borgström, and E. P. A. M. Bakkers, *Journal of Applied Physics* **106**, 124303 (2009).
- [71] A. E. Hansen, M. T. Björk, C. Fasth, C. Thelander, and L. Samuelson, *Physical Review B* **71** (2005), 10.1103/physrevb.71.205328.
- [72] L. O. Olsson, C. B. M. Andersson, M. C. Håkansson, J. Kanski, L. Ilver, and U. O. Karlsson, *Phys. Rev. Lett.* **76**, 3626 (1996).
- [73] D. Aasen, M. Hell, R. V. Mishmash, A. Higginbotham, J. Danon, M. Leijnse, T. S. Jespersen, J. A. Folk, C. M. Marcus, K. Flensberg, and J. Alicea, *Physical Review X* **6** (2016), 10.1103/physrevx.6.031016.
- [74] T. Ihn, *Semiconductor Nanostructures* (Oxford University Press, 2009).
- [75] L. P. Kouwenhoven, D. G. Austing, and S. Tarucha, *Reports on Progress in Physics* **64**, 701 (2001).
- [76] J. Gramich, *Andreev and Spin Transport in Carbon Nanotube Quantum Dot Hybrid Devices*, Ph.D. thesis, University of Basel (2016).
- [77] M. Ciorga, A. S. Sachrajda, P. Hawrylak, C. Gould, P. Zawadzki, S. Jullian, Y. Feng, and Z. Wasilewski, *Physical Review B* **61**, R16315 (2000).
- [78] L. A. Ponomarenko, F. Schedin, M. I. Katsnelson, R. Yang, E. W. Hill, K. S. Novoselov, and A. K. Geim, *Science* **320**, 356 (2008).
- [79] F. Kuemmeth, S. Ilani, D. C. Ralph, and P. L. McEuen, *Nature* **452**, 448 (2008).
- [80] F. A. Zwanenburg, C. E. W. M. van Rijmenam, Y. Fang, C. M. Lieber, and L. P. Kouwenhoven, *Nano Letters* **9**, 1071 (2009).
- [81] V. Ranjan, *Admittance and Noise Detection in Mesoscopic Systems via GHz Impedance Matching*, Ph.D. thesis, University of Basel (2017).
- [82] J. Schindele, *Observation of Cooper Pair Splitting and Andreev Bound States in Carbon Nanotubes*, Ph.D. thesis, University of Basel (2014).
- [83] C. W. J. Beenakker, *Physical Review B* **44**, 1646 (1991).
- [84] R. Hanson, L. P. Kouwenhoven, J. R. Petta, S. Tarucha, and L. M. K. Vandersypen, *Reviews of Modern Physics* **79**, 1217 (2007).

- [85] S. De Franceschi, S. Sasaki, J. M. Elzerman, W. G. van der Wiel, S. Tarucha, and L. P. Kouwenhoven, [Physical Review Letters](#) **86**, 878 (2001).
- [86] Y. Meir, N. S. Wingreen, and P. A. Lee, [Phys. Rev. Lett.](#) **70**, 2601 (1993).
- [87] S. M. Cronenwett, T. H. Oosterkamp, and L. P. Kouwenhoven, [Science \(New York, N.Y.\)](#) **281**, 540 (1998).
- [88] A. Kogan, S. Amasha, and M. A. Kastner, [Science \(New York, N.Y.\)](#) **304**, 1293 (2004).
- [89] S. Csonka, L. Hofstetter, F. Freitag, S. Oberholzer, C. Schönenberger, T. S. Jespersen, M. Aagesen, and J. Nygård, [Nano Letters](#) **8**, 3932 (2008).
- [90] J.-D. Pillet, C. H. L. Quay, P. Morfin, C. Bena, A. L. Yeyati, and P. Joyez, [Nature Physics](#) **6**, 965 (2010).
- [91] H. Ibach and H. Lüth, *Festkörperphysik* (Springer Berlin Heidelberg, 1999).
- [92] M. Tinkham, *Introduction to Superconductivity: Second Edition (Dover Books on Physics) (Vol i)* (Dover Publications, 2004).
- [93] J. Bardeen, L. N. Cooper, and J. R. Schrieffer, [Physical Review](#) **108**, 1175 (1957).
- [94] D. J. Thouless, [Physical Review](#) **117**, 1256 (1960).
- [95] A. L. Yeyati, J. C. Cuevas, A. López-Dávalos, and A. Martín-Rodero, [Physical Review B](#) **55**, R6137 (1997).
- [96] M. Gaass, S. Pfaller, T. Geiger, A. Donarini, M. Grifoni, A. K. Hüttel, and C. Strunk, [Physical Review B](#) **89** (2014), 10.1103/physrevb.89.241405.
- [97] J. Gramich, A. Baumgartner, and C. Schönenberger, [Physical Review Letters](#) **115**, 1 (2015).
- [98] C. W. J. Beenakker, in *Quantum Mesoscopic Phenomena and Mesoscopic Devices in Microelectronics* (Springer Netherlands, 2000) pp. 51–60.
- [99] G. E. Blonder, M. Tinkham, and T. M. Klapwijk, [Physical Review B](#) **25**, 4515 (1982).
- [100] a. F. Andreev, [Sov Phys JETP](#) **19**, 1228 (1964).
- [101] B. Pannetier and H. Courtois, [Journal of Low Temperature Physics](#) **118**, 599 (2000).
- [102] T. M. Klapwijk, [Journal of Superconductivity](#) **17**, 593 (2004).
- [103] C. W. J. Beenakker, in *Springer Series in Solid-State Sciences* (Springer Berlin Heidelberg, 1992) pp. 235–253.
- [104] C. Bena, [The European Physical Journal B](#) **85** (2012), 10.1140/epjb/e2012-30133-0.

- [105] J. Cayao, *Hybrid superconductor-semiconductor nanowire junctions as useful platforms to study Majorana bound states*, Ph.D. thesis, Universidad Autonomia de Madrid (2016).
- [106] P. Joyez, “Probing the density of states in proximity systems, lecture notes capri spring school,” (2012).
- [107] I. Kulik, Soviet Physics JETP-USSR **30**, 944 (1970).
- [108] A. Zagoskin, *Quantum Theory of Many-Body Systems* (Springer International Publishing, 2014).
- [109] K. K. Likharev, *Reviews of Modern Physics* **51**, 101 (1979).
- [110] A. Martín-Rodero and A. L. Yeyati, *Advances in Physics* **60**, 899 (2011).
- [111] J. Schindele, A. Baumgartner, R. Maurand, M. Weiss, and C. Schönenberger, *Physical Review B - Condensed Matter and Materials Physics* **89**, 1 (2014).
- [112] T. Meng, S. Florens, and P. Simon, *Phys. Rev. B* **79**, 224521 (2009).
- [113] A. Braggio, M. Governale, M. G. Pala, and J. König, *Solid State Communications* **151**, 155 (2011).
- [114] J.-D. Pillet, P. Joyez, R. Žitko, and M. F. Goffman, *Phys. Rev. B* **88** (2013), 10.1103/PhysRevB.88.045101.
- [115] E. J. H. L. X. Jiang, M. Houzet, R. Aguado, C. M. Lieber, and S. D. Franceschi, *Nature Nanotechnology* -, 1 (2013).
- [116] R. S. Deacon, Y. Tanaka, A. Oiwa, R. Sakano, K. Yoshida, K. Shibata, K. Hirakawa, and S. Tarucha, *Phys. Rev. Lett.* **104** (2010).
- [117] J. Gramich, A. Baumgartner, and C. Schönenberger, *Physical Review B* **96**, 1 (2017).
- [118] C. Janvier, L. Tosi, L. Bretheau, Girit, M. Stern, P. Bertet, P. Joyez, D. Vion, D. Esteve, M. F. Goffman, H. Pothier, and C. Urbina, *Science* **349**, 1199 (2015).
- [119] J. Ridderbos, *Quantum dots and superconductivity in Ge - Si nanowires*, Ph.D. thesis, University of Twente (2018).
- [120] C. W. J. Beenakker and H. van Houten, *Single-Electron Tunneling and Mesoscopic Devices* , 175 (1992).
- [121] J. A. van Dam, Y. V. Nazarov, E. P. A. M. Bakkers, S. De Franceschi, and L. P. Kouwenhoven, *Nature* **442**, 667 (2006).
- [122] K. Grove-Rasmussen, H. I. Jørgensen, B. M. Andersen, J. Paaske, T. S. Jespersen, J. Nygård, K. Flensberg, and P. E. Lindelof, *Physical Review B* **79**, 134518 (2009).

- [123] A. Eichler, M. Weiss, S. Oberholzer, C. Schönenberger, A. L. Yeyati, J. C. Cuevas, and A. M. Rodero, *Physical Review Letters* **99** (2007), [10.1103/physrevlett.99.126602](#).
- [124] E. J. H. Lee, X. Jiang, R. Aguado, G. Katsaros, C. M. Lieber, and S. De Franceschi, *Phys. Rev. Lett.* **109**, 186802 (2012).
- [125] M. Ruby, F. Pientka, Y. Peng, F. von Oppen, B. W. Heinrich, and K. J. Franke, *Physical Review Letters* **115** (2015), [10.1103/physrevlett.115.087001](#).
- [126] P. Recher, E. V. Sukhorukov, and D. Loss, *Physical Review B* **63**, 165314 (2001).
- [127] A. Freyn, B. Douçot, D. Feinberg, and R. Mélin, *Physical Review Letters* **106** (2011).
- [128] T. Jonckheere, J. Rech, T. Martin, B. Douçot, D. Feinberg, and R. Mélin, *Physical Review B* **87** (2013), [10.1103/PhysRevB.87.214501](#).
- [129] Y. Cohen, Y. Ronen, J.-H. Kang, M. Heiblum, D. Feinberg, R. Mélin, and H. Shtrikman, *Proceedings of the National Academy of Sciences* **115**, 6991 (2018).
- [130] D. B. Suyatin, C. Thelander, M. T. Björk, I. Maximov, and L. Samuelson, *Nanotechnology* **18**, 105307 (2007).
- [131] W. Chang, S. M. Albrecht, T. S. Jespersen, F. Kuemmeth, P. Krogstrup, J. Nygård, and C. M. Marcus, *Nature Nanotechnology* **10**, 232 (2015).
- [132] S. Zihlmann, *Spin and charge relaxation in graphene*, Ph.D. thesis, University of Basel (2018).
- [133] F. Pobell, *Matter and Methods at Low Temperatures* (Springer-Verlag Berlin Heidelberg, 2007).
- [134] K. A. Dick, *Progress in Crystal Growth and Characterization of Materials* **54**, 138 (2008).
- [135] P. Caroff, J. Bolinsson, and J. Johansson, *IEEE Journal of Selected Topics in Quantum Electronics* **17**, 829 (2011).
- [136] C. Jünger, A. Baumgartner, R. Delagrangé, D. Chevallier, S. Lehmann, M. Nilsson, K. A. Dick, C. Thelander, and C. Schönenberger, *Communications Physics* **2** (2019), [10.1038/s42005-019-0162-4](#).
- [137] J. Johansson, K. A. Dick, P. Caroff, M. E. Messing, J. Bolinsson, K. Deppert, and L. Samuelson, *The Journal of Physical Chemistry C* **114**, 3837 (2010).
- [138] P. Caroff, K. A. Dick, J. Johansson, M. E. Messing, K. Deppert, and L. Samuelson, *Nature Nanotechnology* **4**, 50 (2008).
- [139] Z. Zanolli, F. Fuchs, J. Furthmüller, U. von Barth, and F. Bechstedt, *Physical Review B* **75** (2007), [10.1103/physrevb.75.245121](#).

- [140] A. Belabbes, C. Panse, J. Furthmüller, and F. Bechstedt, *Physical Review B* **86** (2012), 10.1103/physrevb.86.075208.
- [141] I.-J. Chen, S. Lehmann, M. Nilsson, P. Kivisaari, H. Linke, K. A. Dick, and C. Thelander, *Nano Letters* **17**, 902 (2017).
- [142] D. C. Joy, D. E. Newbury, and D. L. Davidson, *Journal of Applied Physics* **53**, R81 (1982).
- [143] S. Zaefferer and N.-N. Elhami, *Acta Materialia* **75**, 20 (2014).
- [144] F. S. Thomas, A. Baumgartner, L. Gubser, C. Jünger, G. Fülöp, M. Nilsson, F. Rossi, V. Zannier, L. Sorba, and C. Schönenberger, *Nanotechnology* **31**, 135003 (2020).
- [145] F. Rossella, A. Bertoni, D. Ercolani, M. Rontani, L. Sorba, F. Beltram, and S. Roddaro, *Nature Nanotechnology* **9**, 997 (2014).
- [146] M. Nilsson, F. V. Boström, S. Lehmann, K. A. Dick, M. Leijnse, and C. Thelander, *Physical Review Letters* **121** (2018), 10.1103/physrevlett.121.156802.
- [147] N. A. Court, A. J. Ferguson, and R. G. Clark, *Superconductor Science and Technology* **21**, 015013 (2007).
- [148] S. D. Franceschi, S. Sasaki, J. M. Elzerman, W. G. van der Wiel, S. Tarucha, and L. P. Kouwenhoven, *Physical Review Letters* **86**, 878 (2001).
- [149] T. Sand-Jespersen, J. Paaske, B. M. Andersen, K. Grove-Rasmussen, H. I. Jørgensen, M. Aagesen, C. B. Sørensen, P. E. Lindelof, K. Flensberg, and J. Nygård, *Physical Review Letters* **99** (2007), 10.1103/physrevlett.99.126603.
- [150] A. Jellinggaard, K. Grove-Rasmussen, M. H. Madsen, and J. Nygård, *Physical Review B* **94**, 1 (2016).
- [151] J. Gramich, A. Baumgartner, and C. Schönenberger, *Applied Physics Letters* **108**, 172604 (2016).
- [152] R. C. Dynes, V. Narayanamurti, and J. P. Garno, *Physical Review Letters* **41**, 1509 (1978).
- [153] P. F. Bagwell, *Physical Review B* **46**, 12573 (1992).
- [154] S. Takei, B. M. Fregoso, H.-y. Hui, A. M. Lobos, and S. Das Sarma, *Physical Review Letters* **110**, 186803 (2013).
- [155] C. X. Liu, F. Setiawan, J. D. Sau, and S. Das Sarma, *Physical Review B* **96**, 1 (2017).
- [156] C. Jünger, R. Delagrangé, D. Chevallier, S. Lehmann, K. A. Dick, C. Thelander, J. Klinovaja, D. Loss, A. Baumgartner, and C. Schönenberger, *ArXiv*, 2001.07666 (2020).
- [157] D. Goldhaber-Gordon, H. Shtrikman, D. Mahalu, D. Abusch-Magder, U. Meirav, and M. A. Kastner, *Nature* **391**, 156 (1998).

- [158] T. Sand-Jespersen, J. Paaske, B. M. Andersen, K. Grove-Rasmussen, H. I. Jørgensen, M. Aagesen, C. B. Sørensen, P. E. Lindelof, K. Flensberg, and J. Nygård, *Phys. Rev. Lett.* **99** (2007), 10.1103/PhysRevLett.99.126603.
- [159] B.-K. Kim, Y.-H. Ahn, J.-J. Kim, M.-S. Choi, M.-H. Bae, K. Kang, J. S. Lim, R. López, and N. Kim, *Physical Review Letters* **110** (2013), 10.1103/PhysRevLett.110.076803.
- [160] W. Chang, V. E. Manucharyan, T. S. Jespersen, J. Nygård, and C. M. Marcus, *Phys. Rev. Lett.* **110** (2013), 10.1103/PhysRevLett.110.217005.
- [161] K. Grove-Rasmussen, G. Steffensen, A. Jellinggaard, M. H. Madsen, R. Žitko, J. Paaske, and J. Nygård, *Nature Communications* **9**, 2376 (2018).
- [162] A. Clerk and V. Ambegaokar, *Physical Review B* **61**, 9109 (2000).
- [163] R. Maurand, T. Meng, E. Bonet, S. Florens, L. Marty, and W. Wernsdorfer, *Phys. Rev. X* **2** (2012), 10.1103/PhysRevX.2.019901.
- [164] R. Delagrangé, D. Luitz, R. Weil, A. Kasumov, V. Meden, H. Bouchiat, and R. Deblock, *Phys. Rev. B* **91** (2015), 10.1103/PhysRevB.91.241401.
- [165] M. Ferrier, T. Arakawa, T. Hata, R. Fujiwara, R. Delagrangé, R. Weil, R. Deblock, R. Sakano, A. Oguri, and K. Kobayashi, *Nature Physics* **12**, 230 (2015).
- [166] S. dHollós, G. Fabian, A. Baumgartner, J. Nygård, and C. Schönenberger (AIP, 2013).
- [167] M. T. Björk, A. Fuhrer, A. E. Hansen, M. W. Larsson, L. E. Fröberg, and L. Samuelson, *Physical Review B - Condensed Matter and Materials Physics* **72**, 1 (2005).
- [168] A. V. Kretinin, R. Popovitz-Biro, D. Mahalu, and H. Shtrikman, *Nano Letters* **10**, 3439 (2010).
- [169] S. Li, N. Kang, D. X. Fan, L. B. Wang, Y. Q. Huang, P. Caroff, and H. Q. Xu, *Scientific Reports* **6**, 1 (2016).
- [170] M. J. Biercuk, N. Mason, J. Martin, A. Yacoby, and C. M. Marcus, *Physical Review Letters* **94** (2005), 10.1103/physrevlett.94.026801.
- [171] H. A. Nilsson, P. Samuelsson, P. Caroff, and H. Q. Xu, *Nano Letters* **12**, 228 (2011).
- [172] T. Nishio, T. Kozakai, S. Amaha, M. Larsson, H. A. Nilsson, H. Q. Xu, G. Zhang, K. Tateno, H. Takayanagi, and K. Ishibashi, *Nanotechnology* **22** (2011), 10.1088/0957-4484/22/44/445701.
- [173] J. Xiang, A. Vidan, M. Tinkham, R. M. Westervelt, and C. M. Lieber, *Nature Nanotechnology* **1**, 208 (2006).
- [174] P. Jarillo-Herrero, J. a. van Dam, and L. P. Kouwenhoven, *Nature* **439**, 953 (2006).



- 
- [175] S. Baba, C. Jünger, S. Matsuo, A. Baumgartner, Y. Sato, H. Kamata, K. Li, S. Jeppesen, L. Samuelson, H. Q. Xu, C. Schönenberger, and S. Tarucha, *New Journal of Physics* **20**, 063021 (2018).
- [176] L. Hofstetter, S. Csonka, A. Baumgartner, G. Fülöp, S. d'Hollosy, J. Nygård, and C. Schönenberger, *Physical Review Letters* **107**, 136801 (2011).
- [177] A. Das, Y. Ronen, M. Heiblum, D. Mahalu, A. V. Kretinin, and H. Shtrikman, *Nature Communications* **3**, 1165 (2012).
- [178] G. Fülöp, S. d'Hollosy, A. Baumgartner, P. Makk, V. A. Guzenko, M. H. Madsen, J. Nygård, C. Schönenberger, and S. Csonka, *Physical Review B* **90**, 235412 (2014).
- [179] G. Fülöp, F. Domínguez, S. d'Hollosy, A. Baumgartner, P. Makk, M. Madsen, V. Guzenko, J. Nygård, C. Schönenberger, A. L. Yeyati, and S. Csonka, *Physical Review Letters* **115**, 227003 (2015).
- [180] M. T. Deng, C. L. Yu, G. Y. Huang, M. Larsson, P. Caroff, and H. Q. Xu, *Nano Letters* **12**, 6414 (2012).
- [181] Ö. Gül, H. Zhang, J. D. S. Bommer, M. W. A. de Moor, D. Car, S. R. Plissard, E. P. A. M. Bakkers, A. Geresdi, K. Watanabe, T. Taniguchi, and L. P. Kouwenhoven, *Nature Nanotechnology* (2018), 10.1038/s41565-017-0032-8.
- [182] T. Dirks, T. L. Hughes, S. Lal, B. Uchoa, Y.-F. Chen, C. Chialvo, P. M. Goldbart, and N. Mason, *Nature Physics* **7**, 386 (2011).
- [183] C. Fasth, A. Fuhrer, M. T. Björk, and L. Samuelson, *Nano Letters* **5**, 1487 (2005).
- [184] S. Baba, S. Matsuo, H. Kamata, R. S. Deacon, A. Oiwa, K. Li, S. Jeppesen, L. Samuelson, H. Q. Xu, and S. Tarucha, *Applied Physics Letters* **111**, 233513 (2017).
- [185] P. Recher and D. Loss, *Physical Review B* **65**, 165327 (2002).
- [186] J. Schindele, A. Baumgartner, and C. Schönenberger, *Physical Review Letters* **109**, 1 (2012).



# A Fabrication Recipes

---

Already in the chapter 3, fabrication techniques are discussed. The aim of this appendix is to provide details of the fabrication recipes.

## A.1. Fabrication of InAs Nanowire devices

### A.1.1. Wafer characteristics

- Substrate material: Silicon
- Dopant: p-type, boron
- Resistivity: 0.003 - 0.005  $\Omega\text{m}$
- Capping layer: 400 nm silicon oxide

### A.1.2. Cleaning

1. Dicing the wafer in appropriate sizes (2.5 cm $\times$ 2.5 cm)
2. Clean in Acetone, IPA for each  $\sim$ 5 min in ultrasonic
3. Blow-dry with N<sub>2</sub>
4. UVO treatment for  $\sim$ 5 min (Model 42-220, Jelight Company)

## A.2. Electron beam lithography

### A.2.1. PMMA etch mask

1. Spin-coat PMMA 950K (4000rpm for 300 nm, bake at 180  $^{\circ}\text{C}$  for 3 min)
2. Expose with E-beam (10 keV; Area dose=240  $\mu\text{C}/\text{cm}^2$ )
3. Development in 3:1 IPA/MIBK for 60 s

### A.2.2. ZEP mask for Pb contacts

1. Spin coat ZEP (300 nm, bake at 180 °C for 3 min)
2. Expose with E-beam (10 keV; Area dose = 35  $\mu\text{C}/\text{cm}^2$ ; Line dose = 505 pC/cm)
3. Development in Pentylacetate for 60 s, and in MIBK:IPA (ratio 9:1) for 10 s, blow-dry with  $\text{N}_2$

### A.3. Reactive ion etching - $\text{O}_2$ plasma cleaning

This plasma is used to remove PMMA residuals.

1. Parameters:  $\text{O}_2$  flow = 16 %, RF power  $P = 30$  W, process pressure  $p = 250$  mTorr,  $t = 1$  min.
2. Etch rates:  
 $\text{SiO}_2$ : negligible  
 PMMA:  $\sim 20$  nm/min

### A.4. Etching of NW native oxide

#### A.4.1. Argon Ion Beam milling

The  $\text{Ar}^+$  etching can be done in-situ in two different systems.  
 In Balzers:

1. Base pressure:  $2 \times 10^{-7}$  mbar
2. Ar flow: 3.2 sccm
3. Process background pressure:  $5 \times 10^{-5}$  mbar
4. Ar plasma: Recipe 2
5. Ar Beam current: 20 mA
6. Ar Beam voltage: 500 V
7. etch time: 23 s (stage perpendicular to Ar source)

In Bestec:

1. Base pressure:  $5 \times 10^{-7}$  mbar
2. Ar flow: adjust needle valve to get constant background pressure

3. Process background pressure:  $5 \times 10^{-5}$  mbar
4. Plasma power: adjust voltage such as output current is 20 mA
5. Extraction voltage:  $-0.6$  kV
6. Anode voltage: 1 kV
7. Etch time: 150 s

#### A.4.2. Sulphur passivation

1. Dilute 0.961 95 g sulphur in 10 ml of 20 %  $\text{NH}_4\text{S}_x$
2. Stir for at least 12 h at  $T \approx 35^\circ\text{C}$
3. Filter 2.5 ml of  $\text{NH}_4\text{S}_x$  to remove sulphur residuals
4. Heat 25 ml (1:10) of  $\text{H}_2\text{O}$  on hotplate at  $40^\circ\text{C}$  for minimum 10 min
5. Add  $\text{NH}_4\text{S}_x$  right before etching; otherwise it will degrade very fast
6. Etch for 120 s on hotplate
7. Stop etching by stirring in  $\text{H}_2\text{O}$  for 30 s
8. Blow-dry with  $\text{N}_2$
9. Build into vacuum chamber within 5 min

#### A.4.3. HCl

1. Dilute 37 % HCl in 1:10  $\text{H}_2\text{O}$
2. Etch for 12 s at RT
3. Stop etching by stirring in  $\text{H}_2\text{O}$  for 30 s
4. Blow-dry with  $\text{N}_2$
5. Build into vacuum chamber within 5 min

## A.5. Etching of epitaxial aluminum shell

Etch mask:

1. O<sub>2</sub> plasma cleaning (after NW deposition) for 1 min
2. Spin adhesion promoter (XY), bake at 185 °C for 2 min
3. Remove adhesion promoter (a monolayer will be left): 7 min Acetone, rinse in IPA, blow-dry with N<sub>2</sub>
4. Spin first layer of EL6, (4000rpm) bake at 185 °C for 90 s
5. Spin second layer of EL6, (4000rpm) bake at 185 °C for 90 s
6. Expose with E-beam (30 keV; Area dose=160  $\mu\text{C}/\text{cm}^2$ ; Line dose=550 pC/cm)
7. Development in 3:1 IPA/MIBK for 60 s
8. Blow-dry with N<sub>2</sub>
9. O<sub>2</sub> plasma cleaning for 1 min
10. Post bake at 120 °C for 1 min

Etching:

1. Prepare beaker for etchant: 40 mL of MF321 with magnetic stirrer in 50 mL beaker
2. Prepare two additional beakers fully filled with 500 mL of DI water
3. Etch time: 75 s for half shell; 85 s for full shell
4. Stop etch process by stirring heavily in first DI water beaker for 20 s, subsequently rinse sample in second DI water beaker for 30 s
5. Blow-dry with N<sub>2</sub>
6. Remove etch mask in acetone at 60 °C for 10 min
7. Rinse in IPA
8. Blow-dry with N<sub>2</sub>

## A.6. Contacts

### A.6.1. Ti/Au leads

This process is used for the base structure and normal metal contacts.

1. Type: E-beam evaporation
2. Pumping to base-pressure of  $\sim 2 \times 10^{-7}$  Pa
3. Evaporate 5 nm of Ti (0.5 Å/s to 1.6 Å/s)
4. Evaporate 50 nm to 70 nm of Au (1.4 Å/s to 1.6 Å/s)

### A.6.2. Ti/Al leads

This process is used for Al as a superconducting contact.

1. Type: E-beam evaporation
2. Pumping to base-pressure of  $\sim 2 \times 10^{-7}$  Pa
3. Evaporate 5 nm of Ti (0.5 Å/s to 0.6 Å/s)
4. Evaporate 50 nm to 70 nm of Al (1.4 Å/s to 1.6 Å/s)

### A.6.3. Pd/Pb/In leads

This process is used for Pb as a superconducting contact. The inside of the vacuum chamber of the Balzers is covered with Al foil.

1. Type: E-beam evaporation
2. Pumping to base-pressure of  $\sim 2 \times 10^{-7}$  Pa
3. Cool down with liquid N to  $\approx -50^\circ\text{C}$
4. evaporate 4.5 nm of Pd
5. Cool down further to  $T \approx -90^\circ\text{C}$
6. evaporate 110 nm of Pb
7. evaporate 20 nm of In





# B Further information on spectroscopy of the superconducting proximity effect in nanowires using integrated quantum dots

---

This part of the appendix provides additional calculations and measurements for chapter 5 [136].

## B.1. Additional numerical calculations for individual ABS

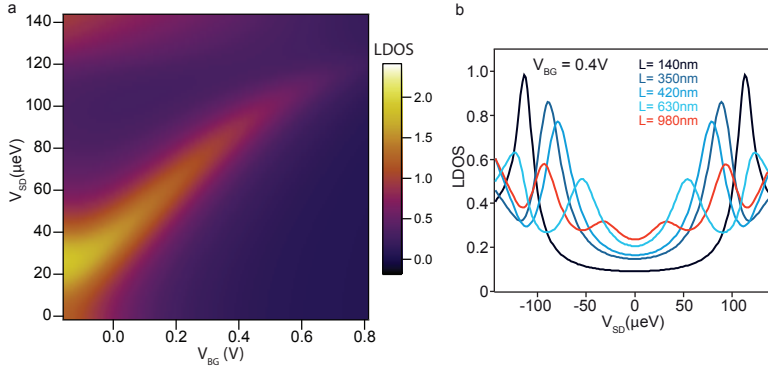


**Figure B.1. Numerical calculations of gate-evolution of individual ABS.** **a** Local DOS with respect to  $V_{SD}$  and backgate  $V_{BG}$  at  $L = 350$  nm. The ABSs width is set to  $\Gamma_{ABS} = 25$   $\mu$ eV. **b** Local DOS with respect to of energy at various distances from the interface for a fixed gate voltage  $V_{BG} = 0.4$  V [136].

## B.2. Additional numerical calculations for interface with disorder

Fig. B.2 shows the LDOS with respect to source drain bias  $V_{SD}$  (at  $V_{BG} = 1$  V) at a distance of  $L = 70$  nm from the S - N interface. The width of the ABS is set to  $\Gamma_{ABS} = 4$   $\mu$ eV. The black cross section shows the LDOS without disorder at the interface. The red cross section shows the same cross section as before, but with a random potential fluctuation at the interface. This was realized by adding a random fluctuation (maximum  $\pm 130$   $\mu$ eV) to the coupling of the superconductor ( $\Gamma_{S,i} = 320$   $\mu$ eV) at each site  $i$  of the NW below. The randomized fluctuation value follows a Gaussian distribution. The plotted cross section was averaged 30 times. As a result, the peaks at the gap edge are smaller in amplitude and also broadened, compared to the clean case. The edges of the gap appear to be slightly smoother.

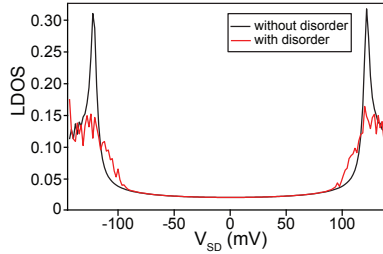


**Figure B.2.** Local DOS with respect to  $V_{SD}$  without (black) and with (red) disorder. The disorder LDOS was averaged 30 times [136].

## B.3. Additional measurements of S - I - S junction

Fig. B.3 shows the normalized  $G$  of a S-I-S tunnel junction (consisting of Al-AlO<sub>2</sub>-Al). The sample was measured in a similar measurement setup as the one discussed in the main text.

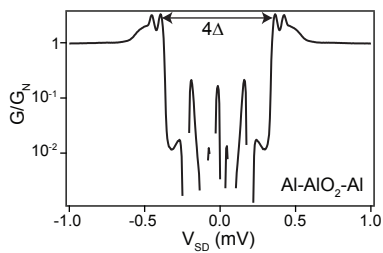


**Figure B.3.** Normalised conductance  $G/G_N$  as a function of  $V_{SD}$  of an S-I-S tunnel junction (made of Al-  $\text{AlO}_2$ -Al).



## C Further information on spectroscopy of superconducting sub-gap states

---

This section provides further measurements, performed on the device presented in chapter 6.

### Side gate dependence

The features observed inside the Coulomb blockade diamonds of Fig. 6.1. (c) are independent from the probing QD, as can be seen in Fig. C.1, which represents a conductance map at zero bias as a function of both back and side-gate. The parallel brighter lines, indicated by the red arrows, correspond

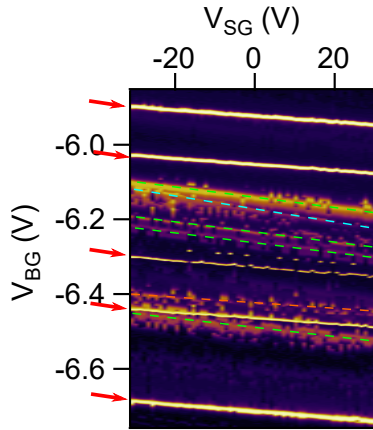


**Figure C.1.** Differential conductance at zero bias as a function of the back and side-gate. The brighter lines, indicated by red arrows, correspond to Coulomb peaks due to the barrier defined QD, while the green, blue and orange lines correspond to the conductance background inside the well defined diamonds. Red, blue, green and orange lines are not parallel, showing that the conductance background is not related to the barrier defined dot [156]. © 2020 by American Physical Society.

to the well defined diamonds of the probing QD. The other lines, which are emphasized by blue, green and orange dashed lines, correspond to the blurred conductance background. They have slopes different from the brighter lines, indicating that they are independent one from the other.

## D Additional measurements of S - QD - S

This section presents additional measurements of InAs NW with an integrated QD, made of WZ tunnel barriers. The measurements were performed on a segment of the NW, without WZ segments, meaning this segment consists of ZB crystal phase.

### D.1. Supercurrent in ZB segment of InAs nanowire

The top panel of Fig. D.1 shows the differential resistance  $dV/dI$  as a function of current  $I$  and gate  $V_{BG}$ . We detect a gate tunable supercurrent, similar to [3]. The central panel presents the extracted critical current  $I_C$  (blue) and the normal state resistance  $R_N$  (black). The lowest panel shows the resulting  $R_N I_C$  product. The maximal supercurrent ( $\approx 20$  nA) is larger, compared to the supercurrent measured in a segment with WZ barriers ( $\approx 5$  nA). However the  $R_N I_C$  product is of similar magnitude  $\approx 8 \mu\text{V}$  to  $16 \mu\text{V}$ .

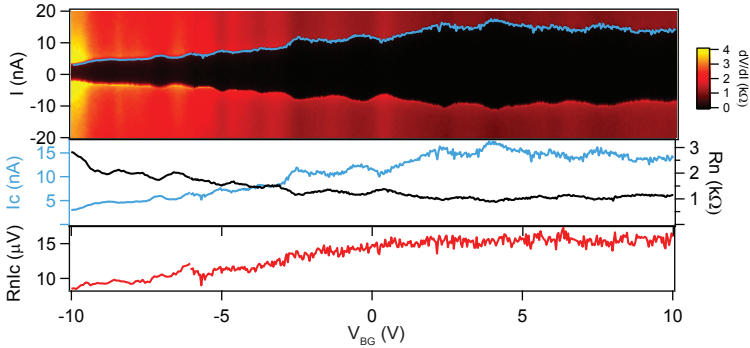


**Figure D.1. Supercurrent in ZB segment of InAs nanowire.** Top:  $dV/dI$  as a function of current  $I$  and gate  $V_{BG}$ . Middle: extracted critical current  $I_C$  (blue) and the normal state resistance  $R_N$  (black). Bottom: resulting  $R_N I_C$  product with respect to  $V_{BG}$ .

## D.2. Resonant tunneling model with two discrete levels

Fig. D.2 shows the result of the resonant tunneling model with two single electron levels in each lead segment  $LS_{1/2}$ .  $E_{A,1/2}$  refers to the energy of the two levels in  $LS_1$ , whereas  $E_{B,1/2}$  is the energy of two levels in  $LS_2$ .

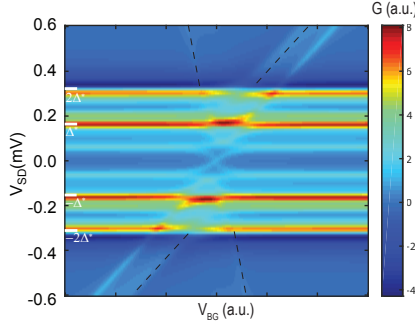


**Figure D.2. Resonant tunneling model with two ABS in each lead segment  $LS_{1/2}$ .** The ABS energies are:  $E_{A,1} = 160 \mu\text{eV}$ ,  $E_{A,2} = 60 \mu\text{eV}$ ,  $E_{B,1} = 160 \mu\text{eV}$ ,  $E_{B,2} = 60 \mu\text{eV}$ . The couplings to the QD are set to:  $\Gamma_{A,1/2} = \Gamma_{B,1/2} = 30 \mu\text{eV}$ .

## D.3. Additional data measured in S - QD - S device

This part of the appendix presents measurement data from an additional device similar to the one presented in Fig. 7.1, which is not discussed in chapter 7. It consists of an InAs NW with an integrated QD (defined by crystal phase engineering) and evaporated aluminum contacts. The junction length of this sample is 400 nm.

### Normal state

In the normal state (applied external magnetic field  $B = 50 \text{ mT}$ , perpendicular) we detect a regular Coulomb blockade (CB) diamond pattern with additional discrete states within the CB region (see Fig. D.3). The resonance broadening of the QD is gate regime is  $\Gamma \approx 200 \mu\text{eV}$ .



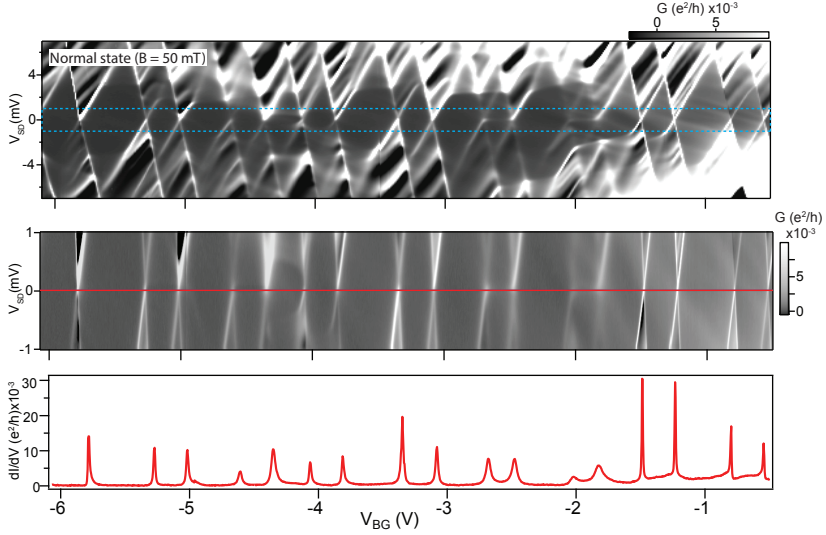


**Figure D.3. Coulomb blockade diamonds in the normal state. a** Differential conductance  $dI/dV$  with respect to bias voltage  $V_{SD}$  and backgate voltage  $V_{BG}$  in the normal state ( $B = 50$  mT). Discrete states with different slope crossing Coulomb blockade regions. **b** Detailed measurement of region marked with blue dashed lines in **a**. **c** Cross section at zero bias voltage  $V_{SD}$ .

### Superconducting state

Fig. D.4 a,b shows CB diamond measurements in the superconducting state. We observe a superconducting energy gap around zero bias voltage  $V_{SD}$ . In addition we marked the detected discrete resonances with blue arrows. We attribute these resonances to discrete levels in the lead segment of the NW, between the QD and one superconducting contact. In Fig. D.4 c,d we present detailed measurements for smaller bias voltages of the same gate region as in Fig. D.4 a,b. We observe several sub-gap states for energies between  $|\Delta^*|$  and  $|2\Delta^*|$ . Fig. D.4 c,f suggest the transformation of a discrete normal state (blue dashed line) into a sub-gap state for energies of  $|\Delta^*|$  to  $|2\Delta^*|$ . Cross sections of this region Fig. D.4 e reveal three different peaks suggesting three sub-gap states. We detect similar characteristics for the gate region in Fig. D.4 d, where the number of states for energies of  $|\Delta^*|$  to  $|2\Delta^*|$  is less clear (see Fig. D.4 g,h).

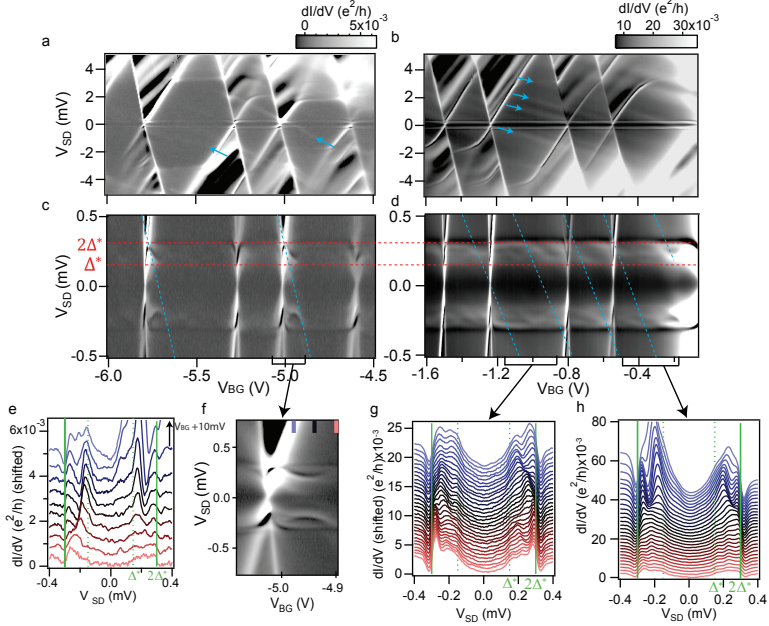


**Figure D.4. Coulomb blockade diamonds in superconducting state.** **a,b** Diamond with additional discrete states for different gate regions. **c,d** Zoom in of **a,b**. **e** waterfall plot of **f**. **g,h** waterfall plot of regions marked in **d**.

# E Further information on Cooper pair splitting in two parallel InAs nanowires

This section provides further measurements, performed on the device presented in chapter 8 [175].

## E.1. Coulomb diamond measurements

In Fig. E.1 we plot Coulomb blockade diamond measurements of the two quantum dots  $QD_{1/2}$  in the two individual nanowires  $NW_{1/2}$  respectively.

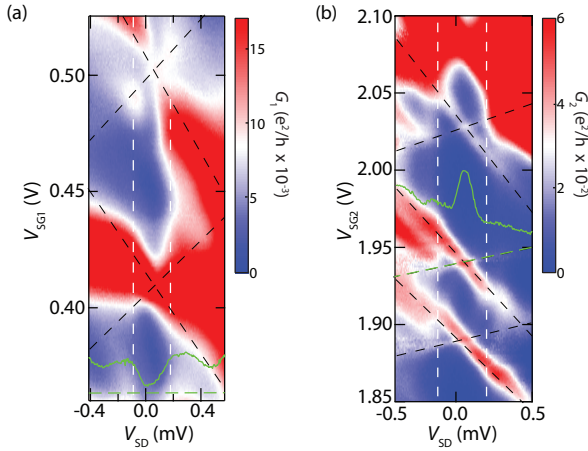


**Figure E.1.** (a) Differential conductance  $G_1$  of quantum dot  $QD_1$  with respect to sidegate voltage  $V_{SG1}$  and source drain bias voltage  $V_{SD}$ . The white lines highlight a conductance suppression, caused by the superconducting energy gap. The cross sections (green insets) are taken along the green dashed lines respectively. (b) Differential conductance  $G_2$  of  $QD_2$  with respect to sidegate voltage  $V_{SG2}$  and bias voltage  $V_{SD}$ . The cross section (green line inset) is taken along the green dashed line [175]. © 2018 by IOP Publishing.



# F Quantum dots in InAs defined by InP tunnel barriers

---

This section shows preliminary results obtained on InAs nanowires with InP tunnel barriers. Fig. F.1 presents a Coulomb diamond measurement of a QD (size:  $\approx 20$  nm) defined by InP barriers (thickness: 5.5 nm). The nanowires are thankfully provided by L. Sorba and the measurement were performed in collaboration with F. Thomas [144].

## F.1. Coulomb diamond measurements

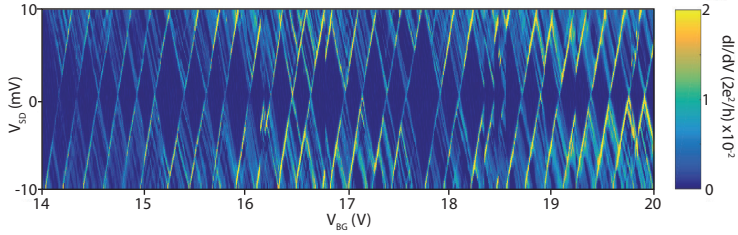


**Figure F.1. Coulomb blockade diamond measurement of InAs/InP nanowire quantum dot.** Differential conductance  $dI/dV$  with respect to source drain bias voltage  $V_{SD}$  and backgate voltage  $V_{BG}$  [144].



# G Preliminary results of superconducting nanowire multi-junction

In this appendix we present preliminary results of InAs nanowires connected to three superconducting electrodes made of lead (Pb). The device (see Fig. G.2) is based on the theoretical proposal of Ref. [127, 128]. The basic idea is to detect a signal originating from non-local crossed andreev reflection, a process called “quartets” (illustrated in Fig. G.1). First signatures have been recently reported in Ref. [129].

## G.1. Quartet device

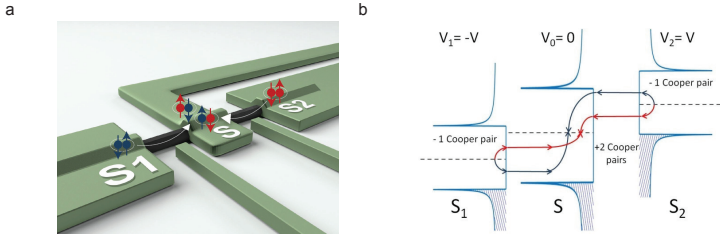


**Figure G.1. Quartet setup.** **a** Schematic of quartet current, generated by non-local crossed Andreev reflection. A Cooper pair originating from electrode  $S_1$  (blue) is combined to a new Cooper pair in  $S$ , together with a Cooper pair originating from  $S_2$  (red). **b** Illustration of energy diagram and non-local crossed Andreev reflection.

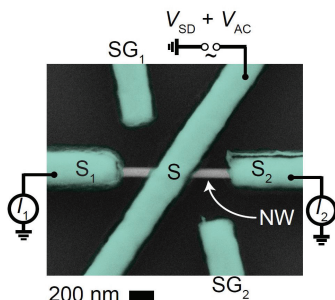


**Figure G.2. Quartet - superconducting nanowire multi-junction.** InAs NW (grey) with three superconducting electrodes S and  $S_{1,2}$  made of Pb (green).

## G.2. Supercurrent in multi-junction

We detect a gate tunable supercurrent (between contact S and  $S_1$ ) in a similar multi-terminal device (shorter junction length:  $\approx 50$  nm), as shown in Fig. G.2 a. The critical current  $I_C$  varies from 20 nA up to 80 nA at large gate voltages  $V_{BG}$ . In Fig. G.2 b we present the supercurrent which is simultaneously measured in both junctions. The black curve shows the current  $I$  measured between contact S and  $S_1$ , whereas the red curve shows the current

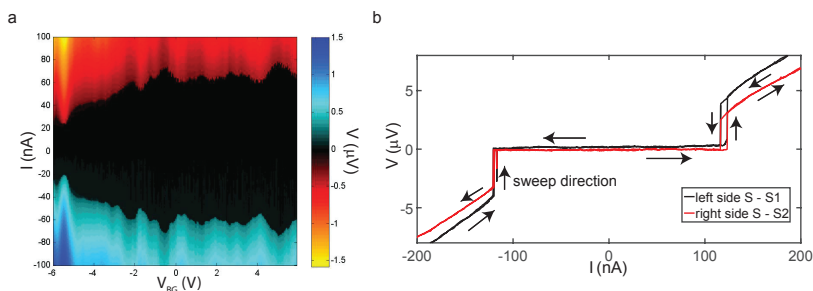


**Figure G.3. Supercurrent measurement in multi-terminal junction.** **a** Voltage  $V$  as a function of current  $I$  and gate voltage  $V_{BG}$  measured between contact S and  $S_1$ . **b** Supercurrent simultaneously measured between contact S and  $S_1$  (black) and S and  $S_2$  (red).



between S and S<sub>2</sub>. In Fig. G.4 we show the measured differential conductance  $G$  measured in both junctions (left: black; right: red) simultaneously when no magnetic field is applied (a) and for finite magnetic field  $B=13$  mT (b) and  $B=35$  mT (c).

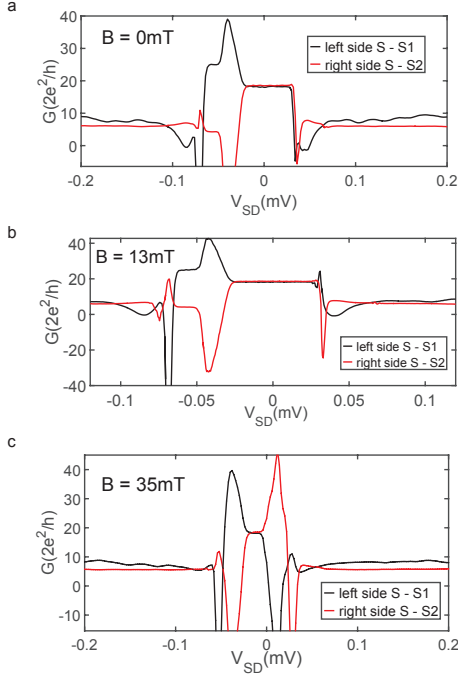


**Figure G.4. Magnetic field dependence.** Differential conductance  $G$  with respect to source-drain bias voltage  $V_{SD}$  for out-of plane magnetic field  $B = 0$  a,  $B = 13$  mT b,  $B = 35$  mT c. Differential conductance  $G$  in left junction S-S<sub>1</sub> shown in black and for right junction S-S<sub>2</sub> shown in red.



# Curriculum Vitae

Christian Helmut Jünger

Born on 30<sup>th</sup> June 1988 in Coburg (Germany)

## Education

- 4/2015 – 4/2019    **PhD in experimental physics at the University of Basel**
- Dissertation in the group of Prof. Dr. C. Schönenberger  
*“Transport Spectroscopy of Semiconductor Superconductor Nanowire Hybrid Devices”*
- 10/2012 – 2/2015    **Masters of Science in Physics at the University of Würzburg**
- Master thesis in the group of Prof. Dr. L. W. Molenkamp  
*“Spin pumping in the 3-Dimensional Topological Insulator HgTe”*
- 10/2009 – 1/2013    **Bachelor of Science in Physics at the University of Würzburg**
- Bachelor thesis in the group of Prof. Dr. F. Reinert  
*“Surface characterization of the topological insulator Sb<sub>2</sub>Te<sub>3</sub> through scanning tunneling microscopy”*
- 10/2007 – 10/2009    Studies of Mechanical Engineering at Technical University of Munich
- 2007                    Abitur at Regiomontanus Gymnasium, Hassfurt

## Research visits

- 9/2016 – 12/2016    *Research Internship*
- In the group of Prof. Dr. S. Tarucha at the University of Tokyo, Japan  
*“Cooper Pair Splitting on parallel InAs Nanowires”*

3/2014 – 4/2014    *Research Internship*

- In the group of Prof. Dr. S. Tarucha at the RIKEN Center for Emergent Matter Science, Japan  
*“Spin pumping in the 3-Dimensional Topological Insulator HgTe”*

### **Awards**

9/2016– 12/2016    *JSPS fellowship for overseas researchers “Young researchers exchange program between japan and switzerland”*

2015 – 2019        *Fellow of PhD Excellence School, “Quantum Science and Technology” at University of Basel*

## Publications

- “From Andreev atoms to Andreev molecules”  
**C. Jünger**, A. Baumgartner, D. Chevallier, R. Delagrangé, S. Lehmann, K. A. Dick, C. Thelander, C. Schönenberger.  
in preparation
- “Magnetic field independent sub-gap states in hybrid Rashba nanowires”  
**C. Jünger\***, R. Delagrangé\*, D. Chevallier, S. Lehmann, K. A. Dick, C. Thelander, J. Klinovaja, D. Loss, A. Baumgartner, C. Schönenberger.  
accepted in *Physical Review Letters (Editors’ Suggestion)*  
[ArXiv: 2001.07666 \(2020\)](#).
- “Highly symmetric and tunable tunnel couplings in InAs/InP nanowire heterostructure quantum dots”  
F. Thomas, A. Baumgartner, L. Gubser, **C. Jünger**, G. Fülöp, M. Nilsson, F. Rossi, V. Zannier, L. Sorba, C. Schönenberger.  
[Nanotechnology](#) **31**, 135003 (2020).
- “Spectroscopy of the superconducting proximity effect in nanowires using integrated quantum dots”  
**C. Jünger**, A. Baumgartner, R. Delagrangé, D. Chevallier, S. Lehmann, M. Nilsson, K. A. Dick, C. Thelander, C. Schönenberger.  
[Communications Physics](#) **2**, 76 (2019).
- “Cooper-pair splitting in two parallel InAs nanowires”  
S. Baba\*, **C. Jünger\***, S. Matsuo, A. Baumgartner, Y. Sato, H. Kamata, K. Li, S. Jeppesen, L. Samuelson, H. Q. Xu, C. Schönenberger, S. Tarucha.  
[New Journal of Physics](#) **20**, 063021 (2018).
- “Dynamical spin injection into graphene by broadband on-chip excitation”  
D. Indolese\*, S. Zihlmann\*, P. Makk, **C. Jünger**, K. Thodkar, C. Schönenberger.  
[Physical Review Applied](#) **10**, 044053 (2018).

- “Single Dirac cone on the Cs-covered topological insulator surface  $Sb_2Te_3$  (0001)”  
C. Seibel, H. Maaß, M. Ohtaka, S. Fiedler, **C. Jünger**, C.- H. Min, H. Bentmann, K. Sakamoto, and F. Reinert.  
[Physical Review B](#) **86**, 161105(R) (2012).

*\*both authors contributed equally to this article*

## Talks

- *Cooper-pair splitting in two parallel InAs nanowires*  
QSQT seminar, University of Basel, Basel (Switzerland), April 2018.
- *Cooper-pair splitting in two parallel InAs nanowires*  
Seminar, University of Lund, Lund (Sweden), January 2018.
- *Quartet States in Semiconducting Nanowires*  
Summer school “Transport in Nanostructures” Capri (Italy), April 2016.

## Poster Contributions

- *“Cooper-pair splitting in two parallel InAs nanowires”*  
Summer school “Quantum Transport in Topological Materials”, Miraflores (Spain), September 2017; poster prize.
- *“Nanowires with three superconducting contacts”*  
NTTI - NGS17, Würzburg (Germany), August 2016.
- *“Nanowires with three superconducting contacts”*  
SNC, Basel (Switzerland), June 2016.
- *“Nanowires with three superconducting contacts”*  
QSIT General Meeting, Arosa (Switzerland), February 2016.

## Acknowledgements

First, I would like to thank my thesis advisor Prof. Dr. Christian Schönenberger. I feel very grateful and honoured that I had the opportunity to pursue research in Christians group. He gave me guidance during the entire time and I learned a lot from him. His fascination for physics but also for science in general was always inspiring for me. His light-hearted and open way to interact with people set the positive atmosphere in the group, which I enjoyed a lot. The group excursions have always been fantastic as well. I really had an amazing time in his group. Thank you Christian.

Second, I thank Prof. Dr. Jesper Nygård and Dr. Fabrizio Nichele for reading my thesis and joining my PhD committee.

Next, I would like to thank Dr. Andreas Baumgartner, who supported me whenever I needed help but also gave me space to work on my own. I am especially thankful for the countless matlab programs he wrote and all the hours we spent together in front of cryostats and measurements setups. His critical comments, especially on manuscripts, always challenged me and helped a lot. Besides science, we also shared interest in the classic Tatort tv - series, especially the swiss one.

Furthermore, I am also grateful for Dr. Raphaëlle Delagrangé. I learned a lot from Raphaëlle, especially on supercurrent measurements. I am also very thankful for her help concerning IGOR programming.

I like to thank Dr. Peter Makk, as a scientist and as a friend. Your comments were always very open and direct which might be one of the reasons why we had a good time together. Even though we worked only on one good scientific project together, it was a pleasure to work with you: this was Tip Top.

With Simon Zihlmann I shared the same office for almost four years. Besides work, we spent many hours together outside of the lab, discussing about life and its mysteries. I wish you all the best for your future and hope you will stay the great scientist you already are.

I would also like to thank Frederick Thomas, who had the pleasure to proof read my thesis. In addition, Frederick was the one who carried on the InP heterostructured quantum dot project, when my PhD was already coming to an end. Thank you.

I am thankful for the friendship I share with Jan Overbeck. We both share a few common interests, most importantly: good music.

I feel also very thankful for the friendship with Roy Haller and David Indolese. We had a lot of fun together during working hours but also outside of the lab, especially in Würzburg.

From my time in this group I have to mention the people who left the group some time ago: Jörg Gramich was probably the best colleague I could have wished for in the beginning of this journey. Clevin Handschin, who gave me many insights into Swiss culture.

Moreover, I want to thank the Quantum and nanoelectronics team: Thomas Hasler, Jann Hinnerk Ungerer, Samuel d'Hollosy, Luk Yi Cheung, Anton Vladoyka, Olivier Faist, Alessia Pally, Zarina Minghazeva, Vishal Ranjan, Carlo Ciaccia, Ian Correo Sampaio, Lukas Gubser, Lujun Wang, Matthijs Hermans, Mehdi Ramezani, Blessonsam Varghese, Han Zheng, Arunav Bordoloi, Dr. Gulibusitan Abulizi, Dr. Peter Rickhaus, Dr. Minkyung Jung, Dr. Malin Nilsson, Dr. Joost Ridderbos, Dr. Artem Kononov, Dr. Paritosh Karnatak, Dr. Libin Wang, Dr. Gergö Fülöp.

Although we got to know each other only at a later stage of my PhD I want to thank my dear friend Martin Endres for his support and friendship which will hopefully last for a long time.

Throughout the PhD time I participated in many collaborations. First, I thank all the collaborators who were so kind to send me their Nanowires: Jesper Nygård, Lars Samuelson, Lucia Sorba, Claes and Kimberly Dick Thelander. I am especially thankful for the exceptional support I received from Claes. It was and still is a pleasure to work with you. Additionally, I had the opportunity to fabricate together with Claes in Lund for a few days, which was really great.

In addition, I had the great opportunity to collaborate with Prof. Seigo Tarucha from the University of Tokyo. I learned a lot in Seigos lab and really enjoyed the time in Tokyo. My special thanks goes to Dr. Shoji Baba, who I worked with in Basel as well as in Tokyo. Shoji made my stay in Tokyo unique and helped me a lot to get a deeper understanding of Japanese culture.

Thanks to Evi Bieler from the Nano-Imaging lab we have very nice SEM images from the crystal phase defined dots.

Furthermore, I have to thank Dr. M. Deng, who was kind enough to discuss fabrication details on the epitaxial aluminum shell etching.

Another special collaboration for me was and still is, the one with Dr. Denis Chevallier. I enjoyed working with you a lot and I am truly thankful for your friendship. Furthermore, I thank the people I had amazing BBQs with: Christina, Marko, Silas, Chris and Manisha. Thanks to Barbara Kammermann and Astrid Kalt bureaucracy was never a problem and thanks to Dominik Sifrig, I always had enough helium to measure: thank you.

Furthermore, I thank Axel Mettenleiter for the graphical design of the cover of this thesis.



---

Outside of work, I am very grateful for the friendship with Helge Mohn, Julian Münch, Wendelin Fischer, Ricardo Thoma and Hannes Mahr. Thank you so much for all the trips: Copenhagen, Bologna, London, Grindelwald or Aberdeen, I loved them all. In the end, It does not really matter where we go, as long as we go there together. I feel very honoured to have you as my friends. I want to express my deepest gratitude to an exceptional scientist who I met 6 years ago during my undergraduate studies: Dr. Erwann Boquillion. Erwann guided me through my Masters thesis and I would not have done a PhD without him. From Erwann I learned how science is supposed to be. I am very thankful that we are friends. Thank you for everything.

I would like to especially mention Dr. Sebastian Rauschert, who joined me the longest time on this journey. I am so grateful for the friendship with you. From the bottom of my heart I wish you all the best. I am looking forward to see you soon in Perth.

Thanks to my beloved parents, Christine and Helmut, I always had the background support I needed to look brave into the future and take the risks that came along when I started to go my own way. I am truly grateful and proud to have such amazing parents. Thank you so much for everything!

Fortunately, I have three awesome siblings: Johanna, Sophie and Markus. Without you, I would not be who I am today. Thank you.